Walter Schottky Institut
Zentralinstitut für physikalische Grundlagen der Halbleiterelektronik
Technische Universität München

Optoelectronic Properties of Defects in Diamond and AlGaN Alloys

Roland Zeisel

Vollständiger Abdruck der von der Fakultät für Physik der Technischen Universität München zur Erlangung des akademischen Grades eines

Doktors der Naturwissenschaften
(Dr. rer. nat.)

genehmigten Dissertation.

Vorsitzender:	Univ.-Prof. Dr. H. Friedrich
Prüfer der Dissertation:	1. Univ.-Prof. Dr. Martin Stutzmann
	2. Univ.-Prof. Dr. R. Gross
	3. Univ.-Prof. PhD F. Koch

Die Dissertation wurde am 4.1.2001 bei der Technischen Universität München eingereicht und durch die Fakultät für Physik am 26.4.2001 angenommen.

To my Family

Zusammenfassung

Um das große Potential der Halbleiter mit großer Bandlücke für elektronische Anwendungen nutzen zu können, ist eine umfassende Kenntnis der Eigenschaften tiefer und insbesondere flacher Defekte notwendig. Diese Arbeit befaßt sich mit Defektspektroskopie solcher Halbleiter, nämlich Diamant und AlGaN Legierungen mit hohem Al-Gehalt.

Kapazitäts-Spannungsmessungen ($C - V$) und thermische und optisch induzierte Deep Level Transient Spectroscopy (DLTS und ODLTS) sind angemessene Methoden, um Eigenschaften tiefer und flacher Defekte zu studieren. Um diese Methoden, welche für „Standardhalbleiter“ wie Si oder GaAs entwickelt wurden, auf die zu untersuchenden Materialien zu übertragen, mußte die Testfrequenz der $C - V$ Messung im Bereich zwischen 60 Hz und 10 kHz liegen. Dies stellt sicher, daß Einflüsse des Serienwiderstandes und der kleinen Emissionsrate der Dotieratome die Messung nicht verfälschen. Dafür wurde eine Kapazitätsmesseinheit entworfen und aufgebaut, welche aus einem Lock-In Verstärker, einem Pulsgenerator und einem Addierer besteht. Proben, die aufgrund ihres hohen Serienwiderstandes oder mangels sperrender Kontakte nicht mit Kapazitätspsektroskopie untersucht werden konnten, wurden mit spektral aufgelöster Photoleitung und verwandten Techniken spektroskopiert. Zusätzlich zu den erwähnten Methoden wurden noch temperaturabhängige Leitfähigkeits- und Hallexperimente durchgeführt um weiteren Einblick in die Transporteigenschaften der Proben zu gewinnen. Alle Experimente wurden durch Computerprogramme automatisiert. Für Hochtemperaturleitfähigkeitsmessungen und Ausheilexperimente im Vakuum wurde ein heizbarer Probenhalter gebaut, dessen Temperatur zwischen Raumtemperatur und 950 K mit Heizraten von bis zu 100 K/min variiert werden kann.

Die $C - V$ Messung ist eine der wichtigsten Möglichkeiten, Dotierkonzentrationen und eingebaute Potentiale an Schottkykontakten zu bestimmen. Für die in dieser Arbeit untersuchten Ag Schottkykontakte auf natürlichen und synthetischen Typ IIb Diamanten ergaben diese Messungen Akzeptordichten von 2×10^{16} cm^{-3} und ein eingebautes Potential von 1.7 V. Die Methode bietet weiterhin die Möglichkeit, die Wasserstoffpassivierung von Borakzeptoren in Diamant nachzuweisen, welche in einem Gleichspannungsplasma bei 400 °C durchgeführt wurde. Die $C - V$ Kennlinien nach einer Passivierung wurden mit einem Zweischicht-Modell erklärt: Durch die Passivierung entsteht eine hoch resistive Schicht, die

sich von der Oberfläche bis zur Eindringtiefe des Wasserstoffs erstreckt. Die zweite Schicht bildet das angrenzende Volumen des Kristalls, in dem die Akzeptordichte unverändert ist. Aus der Lösung der Poisson-Gleichung für diese Situation folgt direkt ein Ausdruck für die Raumladungszonenweite in Abhängigkeit der angelegten Spannung. Damit kann die $C-V$ Kennlinie gefittet werden. Der wesentliche Fitparameter ist die Eindringtiefe des Wasserstoffs, woraus bei bekannter Diffusionszeit und Temperatur die Diffusivität des Wasserstoffs in Diamant berechnet werden kann. Dies ergibt einen Wert von 4.7×10^{-13} cm^2/s bei 400 °C .

Ausheilen der passivierten Schottkydioden bei 750 K ändert deren $C-V$ Kennlinien stark. Dieses Verhalten konnte durch eine Reaktivierung der Borakzeptoren im oberflächennahen Bereich der Raumladungszone erklärt werden. Diese Reaktivierung ist durch das thermische Aufbrechen der Bor-Wasserstoff Bindungen und einer anschließenden Drift des geladenen Wasserstoffs im Feld der Raumladungszone verursacht. Am Ende der Raumladungszone wird der Wasserstoff dann wieder von einem noch nicht passivierten Borakzeptor gebunden. Dieser Effekt konnte durch Anlegen einer Rückwärtspannung während des Ausheilens verstärkt werden, was die positive Ladung des diffundierenden Wasserstoffs belegt.

ODLTS Experimente wurden an synthetischen Typ IIb Diamanten, homo- und heteroepitaktisch gewachsenen, Bor dotierten CVD Diamanten im Spektralbereich von 0.6 eV bis 3 eV durchgeführt. In allen Proben zeigt sich eine Absorptionsschulter im Bereich zwischen 1.2 eV and 1.7 eV, die am deutlichsten in einer homoepitaktisch gewachsenen Probe hervortritt. Die genaue spektrale Form und insbesondere die Temperaturabhängigkeit dieser Defektabsorption konnte durch die Wechselwirkung des Defekts mit dem Wirtsgitter erklärt werden. Dafür wurde die Linienform für Phonon unterstützte Übergänge zwischen vibronischen Zuständen des Defekts mit Matrixelementen für die Defekt-zu-Band Absorption kombiniert. Der Fit des resultierenden Photoionisationswirkungsquerschnitt im Rahmen der Elektron-Phonon-Kopplung an die experimentellen Daten lieferte eine energetische Lage des Defektes von 1.28 eV über dem Valenzband mit einem Franck-Condon Parameter von 0.16 eV.

Die Tatsache, daß diese Defektabsorption mehr oder weniger stark in allen untersuchten Proben zu finden ist, legt die Vermutung nahe, daß diese durch einen intrinsischen Defekt verursacht ist. Um dies zu überprüfen, wurden Kohlenstoff implantierte Typ IIb Diamanten untersucht. Da die Kohlenstoff-Implantation ausschließlich Vakanzen, Kohlenstoff-Zwischgitteratome und deren Cluster produziert, ist ein Anwachsen der Defektabsorption bei 1.28 eV ein Indiz für die oben erwähnte Vermutung. In der Tat konnte eine Zunahme dieser Absorption mit zunehmender Implantationsdosis beobachtet werden. Zusätzlich wurde eine Absorption im Bereich zwischen 2.5 eV und 3 eV durch Implantation erzeugt. Neben den ODLTS Spektren wurden auch die $C-V$ Kennlinien signifikant durch die Implantati-

on beeinflußt. Wie schon im Falle der Wasserstoffpassivierung, konnte das Verhalten durch ein Zweischichtsystem erklärt werden. Hierbei ist die hochresistive Schicht durch die Kompensation der Implantationsdefekte zu erklären. Ausheilexperimente an den implantierten Dioden zeigten ein Verschwinden des Defektes bei 1.28 eV bei 550 K mit einer Migrationsenergie von 1.25 eV. Dies ist in guter Übereinstimmung mit den Literaturdaten für eine Migration des Kohlenstoff-Zwischengitteratoms zur Vakanz mit nachfolgender Vernichtung. Das Ausheilverhalten der $C - V$ Kennlinien weist jedoch gewisse Widersprüche zu dieser Vorstellung auf, so daß kein vollständiges mikroskopisches Modell entwickelt werden konnte.

Theoretische Rechnungen verschiedener Gruppen weisen dem interstitiellen Li in Diamant die Eigenschaft eines flachen Donators zu. Deshalb wurden homoepitaktisch gewachsene, Li dotierte Diamantschichten auf thermisch aktivierte Dunkel- und Photoleitung hin untersucht. Die Dunkelleitfähigkeit der Schichten liegt nur unwesentlich über der des Typ Ib Substrats, die Aktivierungsenergie variiert zwischen 1 eV und 1.3 eV im Bereich zwischen Raumtemperatur und 750 K. Durch spektral aufgelöste Photoleitung konnten zwei neue Defekte bei 0.9 eV und 1.5 eV unter der Leitungsbandkante nachgewiesen werden. Ersterer kann durch UV-Licht metastabil besetzt werden und wird durch die Messung entleert, was zu einem Peak-förmigen Photoleitungsspektrum bei 1 eV führt. Um das Verhalten und die Natur der Defekte ansatzweise zu erklären, wurde ein Modell entwickelt, in dem Li in Verbindung mit einem weiteren, vermutlich strukturellem Defekt die Niveaus bei 0.9 eV und 1.5 eV verursacht.

Die elektronischen Eigenschaften von Si in AlGaN Legierungen wurden mittels verschiedener Spektroskopiemethoden charakterisiert. Die Aktivierungsenergie von Si dotierten AlGaN Schichten variiert von 20 meV (GaN) bis zu 320 meV (AlN). Der Wert für AlN ist im Widerspruch zum einfachen Wasserstoffmodell, welches eine Ionisierungsenergie von nur 60 meV erklärt. Außerdem setzt bei tiefen Temperaturen die Photoleitung erst bei 1.4 eV Photonenenergie ein. Diese Photoleitung ist persistent nach Abschalten des Lichtes, und die Probe geht erst bei Temperaturen über 60 K in die thermisch aktivierte Leitfähigkeit über. Ähnlich der Photoleitung ist nach Abkühlen im Dunklen kein ESR Signal zu detektieren, im Widerspruch zu einem gewöhnlichen effektiv-Masse-Donator. Nach Beleuchtung wird ein – ebenfalls persistentes – ESR-Signal mit einem g Faktor von 1.9885 detektiert. Alle diese Punkte können im Modell der großen Gitterrelaxation von Si (DX-Zustand) erklärt werden. Experimente an Si dotierten AlGaN Legierungen mit 75% und 68% Al-Gehalt zeigen ähnliches Verhalten. Durch ein Ratengleichungsmodell für die Übergänge zwischen den Zuständen des Si Donators konnten die wesentlichen – mit normaler Defekt zu Band Absorption nicht erklärbaren – Eigenschaften der transienten Photoleitung gut verstanden werden: Ein quadratischer Anstieg der Photoleitung nach Beginn der Beleuchtung und eine Abnahme der stationären Photoleitung mit zunehmender Temperatur. Aus der Zerfallszeitkonstante der

Photoleitung nach Abschalten der Beleuchtung konnte die Einfangbarriere bestimmt werden, die die photogenerierten Elektronen am Wiedereinfang in den DX Zustand hindert. Es ergab sich ein Wert von 80 ± 40 meV. Rauschexperimente bei Raumtemperatur und darüber zeigten ein klares Generations-Rekombinationsrauschen. Die Aktivierungsenergie der charakteristischen Zeitkonstante des Rauschprozesses ergibt 390 meV, was in guter Übereinstimmung mit der Summe aus Aktivierung der Leitfähigkeit (320 meV) und der Einfangbarriere (80 meV) ist. Rauschexperimente bei tiefen Temperaturen im Zustand der persistenten Photoleitung zeigen hingegen ein $1/f$-Spektrum. Dieses qualitativ andere Rauschverhalten als bei hohen Temperaturen kann damit erklärt werden, daß sich der Si Donator nach Photoionisierung im flachen substitutionellen Zustand befindet und somit ein Rauschspektrum erzeugt, wie es typisch für ein Material ist, das mit effektiv-Masse-Donatoren dotiert ist (z. B. GaN).

Contents

1 Introduction **1**

2 Theoretical Considerations **5**

2.1 Charge carrier transport 5

2.1.1 Band transport 5

2.1.2 Impurity band 6

2.1.3 Hopping 7

2.2 Interaction of light with matter 7

2.2.1 Frequency dependence of the dielectric function 9

2.3 Interaction between defects and bands 10

2.3.1 Thermal emission and capture 10

2.3.2 Optical defect ionisation 11

2.4 The space charge region 15

3 Experimental Methods **19**

3.1 Capacitance measurement 19

3.2 Performance of the setup 21

3.2.1 Frequency behaviour 21

3.2.2 Time behaviour 22

3.3 Choosing the test frequency 22

3.4 Transient space charge spectroscopy 25

3.4.1 The rate window concept 28
3.4.2 Optical emission 30
3.4.3 Sensitivity 33
3.4.4 Type of charge carriers 34

4 Experimental Setup **37**

5 Diamond **41**
5.1 Material properties 41
5.2 Growth 42
5.3 Impurities and classification 43

6 Boron in Diamond **47**

7 ODLTS Investigations of Boron doped Diamond **51**
7.1 CVD diamond 51
7.2 Ion implantation and annealing 60
7.2.1 Experimental 61
7.2.2 Measurements 61
7.2.3 Discussion 70

8 Hydrogen-Boron Interactions **75**
8.1 Passivation reactor 76
8.2 $C-V$ profiling of passivated samples 77
8.3 Bias annealing of passivated diodes 80

9 Li doped CVD Diamond **85**
9.1 Dark conductivity 86
9.2 Photoconductivity 87
9.3 Photoconductivity excitation spectroscopy 89

10 Group-III Nitrides **93**

11 Si in AlGaN Alloys **97**

11.1 Photo and dark conductivity 100

11.2 EPR measurements 101

11.3 Microscopic model 104

11.4 Dynamics 107

11.4.1 Conductivity 107

11.4.2 Noise 114

12 Summary and Outlook **121**

A Influence of a Compensated Layer on the $C-V$ Profile **125**

B Inhomogeneous trap distribution **127**

CHAPTER 1

Introduction

From the materials scientists point of view, the rapidly increasing demand for high speed data transfer reads as a recommendation for wide band gap semiconductors. To satisfy the needs for these applications, properties like thermal conductivity, break down field and saturation velocity are the key issues. As can be seen from Tab. 1.1, the wide bandgap semiconductors are superior to Si in most of their properties. In order to quantify the performance of a material for a unipolar device, the so called figures-of-merit have been introduced. They characterise the limit of the device that " *is not likely to be surpassed by that of any attainable design, no matter how optimized or cleverly conceived*" [Joh65]. In Tab. 1.2 the figures of merit for some semiconductors are summarized. The Keyes figure-of-merit has been invented as a criterion for integrated circuits, where the dissipation of heat is the crucial limitation. For microwave power devices, the Johnson figure-of-merit has been developed, which is the squared product of break down field times saturation velocity.

Material	Band gap		Electron mobility	Break down field	Thermal conductivity	Saturation velocity for electrons	Static dielectric constant
	E_G (eV)		$\mu\left(\frac{\text{cm}^2}{\text{Vs}}\right)$	F_B(V/cm)	$\lambda\left(\frac{\text{W}}{\text{cmK}}\right)$	v_{sat}(cm/s)	$\varepsilon(\omega=0)$
Si	1.1	i	1400	3×10^5	1.5	10^7	11.8
GaAs	1.4	d	8500	4×10^5	0.5	2×10^7	12.8
InP	1.34	d	5000	5×10^5	0.74	2.7×10^7	12.6
6H SiC	3.0	i	370	2.4×10^6	5	2×10^7	9.7
GaN	3.45	d	900	5×10^6	1.3	2.7×10^7	9.5
AlN	6.2	d	300	1.2×10^7	2.5	2×10^7	8.2
Diamond	5.48	i	2200	1×10^7	20	2.7×10^7	5.7

Table 1.1: Physical properties of important semiconductors. If temperature dependent, the properties are given at 300 K. In the band gap column i and d denote an indirect and direct band gap, respectively.

Figure-of-merit		Si	GaAs	InP	6H-SiC	GaN	AlN	Diamond
Keyes	$\lambda\sqrt{\frac{v_{sat}}{\varepsilon}}$	1	0.45	0.78	5.2	1.6	2.8	31.5
Johnson	$(F_B v_{sat})^2$	1	7.1	20	256	2025	6400	8100

Table 1.2: Keyes' and Johnsons figures-of-merit of some semiconductors, normalized to Si.

But not only the electronic properties make a material interesting for modern semiconductor device applications. The market volume for optical communications, including small and large area displays as well as laser diodes from the infrared to the blue and ultraviolet range, is expected to grow even faster than the one for pure electronic devices. Therefore the optical properties of a material can strongly push its technological development. This is one of the reasons why the group-III nitrides have received such a large attention during the last years. All compounds of AlN, GaN and InN exhibit a direct band gap, which is tunable from 1.9 eV to 6.2 eV, i. e. from the red into the deep UV region (cf. Fig. 10.1). This qualifies the nitrides for optical emission and sensor devices. Additionally, their high thermal and mechanical stability makes them superior to the wide bandgap II-IV compounds.

Diamond with its indirect band gap is unsuitable for efficient light emission involving band to band transitions. However, recently it has been shown that an internal transition at the nitrogen-vacancy complex in diamond is a perfect source for single photons, which are essential for e. g. quantum cryptography [Kur00]. Furthermore, due to its high radiation hardness, diamond offers great potential for stable radiation detectors [Ber00].

Technology however, has to overcome some severe problems to make these materials competitive on the market with well established semiconductors like Si and GaAs. A main disadvantage of most wide bandgap semiconductors is the lack of an inexpensive substrate for epitaxial growth. This forces the grower to use substrates with a considerable lattice mismatch, causing a high density of structural defects in the layers. In the case of nitrides, an Al_2O_3 substrate is most commonly used, whereas for CVD-diamond Si is the usual substrate material. Only SiC can be grown in reasonable large bulk crystals, which can be cut into wafers. Another drawback that haunts the nitrides and especially diamond is the lack of shallow dopants. Although the nitrides can be easily n-type doped by Si, p-type doping using Mg is not ideal due to the high activation energy of 170 meV of the acceptor in GaN. This is even worse in the case of diamond. Although the incorporation of boron as an acceptor is very easy, the acceptor level is twice as deep as in GaN. In the case of donors in diamond one should not term them shallow donors. Nitrogen, the most common donor, introduces a level at 1.7 eV below the conduction band [Far69] and phosphorus, the most shallow of all known donors in diamond, has an activation energy of 0.6 eV [Koi00].

Before all the visions of the "all-capable"wide band gap materials can become reality, the physicist has to appear on the scene. Key issues like growth properties, doping behaviour of

different promising candidates, the role, properties and nature of deep defects and many more have to be investigated, modeled and hopefully understood, before devices can be fabricated reproducibly. It is the aim of this thesis to contribute a little bit to the understanding of electronic and optical properties of defects in diamond and AlGaN alloys.

In Chapter 2, theoretical aspects which will be used in this thesis are briefly introduced. They contain mechanisms of charge carrier transport, defect kinetics and interaction of light with bulk material and in particular with defects. Chapter 3 gives a survey of the experimental techniques used to characterise the defect properties.

The part of the thesis concerned with diamond starts with a brief compilation of some important properties of diamond in Chapter 5, and the doping behaviour of boron in diamond is reviewed in Chapter 6. Due to the low resistivity of boron doped diamonds, optically induced and thermal Deep Level Transient Spectroscopy (ODLTS and DLTS) becomes possible. Over the last three decades after its invention, this technique has proven its great potential in characterizing deep defects in semiconductors. In Chapter 7, the results of these experiments applied to various diamond samples are presented and analyzed using photoionisation cross sections in the lattice relaxation model. These results motivate a further ODLTS study of carbon ion implanted diamonds, which showed the relation to implantation damage of the defects detected by ODLTS.

Despite the large amount of scientific work that has been done and is under way, characterizing interactions of hydrogen with defects, especially shallow dopants in Si and GaAs, this topic has remained untouched in diamond until 1998, when the first experimental paper about boron-hydrogen interactions was published. To initiate further research in this field, passivation and reactivation of boron by hydrogen has been studied with capacitance techniques. The results are presented in Chapter 8.

In 1997, the report of reproducible shallow n-type doping by phosphorus has stimulated the diamond community to intensify the search for further shallow donors. For example, Li is theoretically predicted to form a shallow donor. In Chapter 9, diamond layers doped with lithium were investigated by means of photoconductance and related techniques. However, the levels that were found to be introduced by Li incorporation did not show a shallow doping behaviour.

The part of this thesis concerned with nitrides starts with Chapter 10, were some crystal properties, growth methods, defects and dopants of the group-III nitrides are summarized. Considering the somehow related compound AlGaAs, the incorporation of Si becomes complex when the Al content exceeds 23 %. Here Si forms a so called DX state which significantly influences the transport properties, the most striking effect being persistent photoconductivity. This subject area has been studied in AlGaAs for many years. Theoretical predictions whether such a Si DX is also formed in AlGaN alloys, are contradictory. To

clarify this situation, Si doped AlGaN alloys with high Al content have been investigated by various spectroscopic techniques. These results are presented in Chapter 11.

CHAPTER 2

Theoretical Considerations

2.1 Charge carrier transport

For a current to flow through a semiconductor, charge carriers have to be mobile. As discussed in the following, there are three different ways of providing mobile charge carriers. In many cases however, it is not easy to determine the transport mechanism, since a combination of different types is possible.

2.1.1 Band transport

Band transport involves carriers, which are mobile within either the conduction or the valence band. Assuming a dominant carrier type (here holes), the conductivity of the sample is given by

$$\sigma = q\mu p, \tag{2.1}$$

where q is the elementary charge, μ the mobility and p the density of holes in the band. The mobility is determined by various scattering mechanisms of charge charge carriers with impurities and phonons and between the charge carriers themselves [See85]. The dominant type of scattering mechanism can be determined by the temperature dependence of the mobility. The density of charge carriers is – in thermal equilibrium – given via the Fermi-Dirac statistics. However, for lightly doped semiconductors, i. e. $E_F - E_V > 3kT$, the Boltzmann approximation is sufficient. As a consequence of electrical neutrality, the hole concentration p of a partially compensated $p-$type semiconductor is given by the equation [Pea49]

$$\frac{p(p+N_D)}{(N_A-N_D)-p} = \frac{N_V}{g_A}\,\mathrm{e}^{-E_A/kT}, \tag{2.2}$$

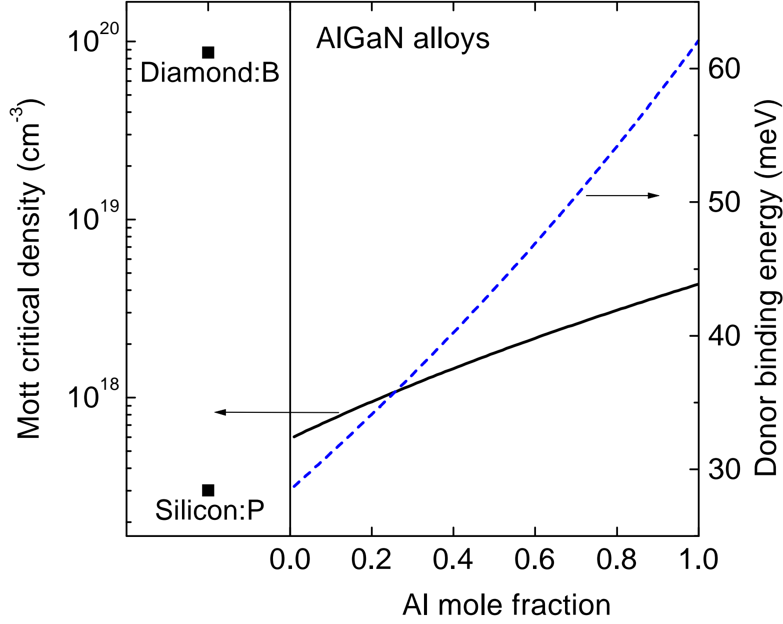

Figure 2.1: Calculated critical doping densities for the Mott metal-insulator transition in AlGaN, Diamond and Si.

where N_A and N_D are the acceptor and compensating donor densities, respectively. g_A is the degeneracy factor of the acceptor and the effective density of states N_V is given by $N_V = 2\left(\frac{2\pi m^* kT}{h^2}\right)^{3/2}$ [Sze85], where m^* is the effective mass of the holes. For sufficiently temperatures, p saturates to $N_A - N_D$, the so called carrier exhaustion regime. For low temperatures, p depends on temperature and can be described by

$$p = 2\frac{N_A - N_D}{g_A N_D}\left(\frac{2\pi m^* kT}{h^2}\right)^{3/2} \mathrm{e}^{-E_A/kT}, \tag{2.3}$$

which is called the carrier freeze-out range. The temperature limit of the validity of Eq. (2.3) strongly depends on the activation energy of the acceptor. For shallow acceptors in silicon, the exhaustion regime is already reached at room temperature, whereas for the boron acceptor in diamond ($E_A = 374$ meV) the low temperature approximation (2.3) is valid up to 800 K.

2.1.2 Impurity band

With increasing doping density, the interaction between the dopant atoms becomes more and more important. If the wave functions of the charge carriers bound to the dopant atoms can overlap, an impurity band is formed, which makes electrical transport possible. A criterion for this so called Mott metal-insulator transition is that the mean distance of neighbouring

dopant atoms equals 4.5 times the Bohr radius a_0 of the bound charge carrier [Mot82]. This leads to the critical doping density

$$N_D^{\text{Mott}} = \frac{1}{(4.5a_0)^3} \tag{2.4}$$

For boron acceptors in diamond $N_D = 8.6 \times 10^{19}$ cm^{-3}, for phosphorus in Si $N_D = 3 \times 10^{17}$ cm^{-3} is calculated. The experimental value for P in Si is $N_D = 3.74 \times 10^{18}$ cm^{-3}. Some examples of the critical density are shown in Fig. 2.1. For AlGaN alloys, the shallow donor ionisation energy as calculated by the hydrogen model (see Sec. 11) is also shown.

2.1.3 Hopping

When empty states near the Fermi level are available because of compensation or a defect distribution as in disordered semiconductors, it is possible that charge carriers can hop from localized state to localized state and therefore contribute to the current density. The conductivity due to such hopping processes can be described by [Hil76]

$$\sigma \propto \mathrm{e}^{(-BT^{-\beta})}. \tag{2.5}$$

For hopping between nearest neighbours, $\beta = 1$. The hopping transport will dominate only at low temperatures, where no significant conduction due to thermal activation of charge carriers into the bands is possible. At even lower temperatures it is more probable that hopping over larger distances occurs, when the energy separation between those empty localized states is smaller than between nearest neighbours. This is called variable range hopping and here $\beta = 1/4$ [Mot87]. In diamond, due to the high compensation and high activation energy, hopping is observed even slightly below room temperature at a doping level of $\approx 1 \times 10^{19}$ cm^{-3} [Vis92, Koi00].

2.2 Interaction of light with matter

The propagation of electromagnetic waves in matter is described by the Maxwell equations, the divergence equations

$$\nabla \cdot \vec{D} = \varrho \qquad \text{and} \qquad \nabla \cdot \vec{B} = 0 \tag{2.6}$$

and the rotation equations

$$\nabla \times \vec{E} = -\frac{\partial \vec{B}}{\partial t} \qquad \text{and} \qquad \nabla \times \vec{H} = \vec{j} + \frac{\partial \vec{D}}{\partial t}. \tag{2.7}$$

Here $\vec{E}$ denotes the electrical field, $\vec{D}$ the electrical displacement, $\vec{B}$ the magnetic flux and $\vec{H}$ the magnetic field. ϱ is the charge density and $\vec{j}$ the electrical current density. $\vec{D}$ is related to $\vec{E}$ via the permittivity in vacuum ε_0 and the polarisation density $\vec{P}$ by the relation

$$\vec{D} = \varepsilon_0 \vec{E} + \vec{P}. \tag{2.8}$$

The same holds for the relation between $\vec{B}$ and $\vec{H}$

$$\vec{B} = \mu_0 \vec{H} + \vec{M} \tag{2.9}$$

with the permeability in vacuum μ_0 and the magnetisation density $\vec{M}$.

For a weakly doped semiconductor, the approximations $\varrho = 0$, $\vec{M} = 0$ and $\vec{j} = 0$ can be made [Kli95]. Combining the rotation equations (2.7) and using the divergence equations (2.6) leads to

$$\nabla^2 \vec{E} - \mu_0 \frac{\partial^2 \vec{D}}{\partial t^2} = 0. \tag{2.10}$$

When the external electric field $\vec{E}$ is small compared to internal atomic fields, a linear relation between $\vec{P}$ and $\vec{E}$ is a good approximation

$$\vec{P} = \varepsilon_0 \chi \vec{E} \tag{2.11}$$

where χ is the electrical susceptibility, which is a measure of the ability of the material to be polarized by an external field. Substituting this into (2.8) leads to

$$\vec{D} = \varepsilon_0 (1 + \chi) \vec{E} = \varepsilon_0 \varepsilon \vec{E}, \tag{2.12}$$

defining the dielectric function ε. In general, ε as well as χ are complex tensors, depending on the frequency ω of the field. However, in most cases it is sufficient to use only a scalar dielectric function

$$\varepsilon(\omega) = \varepsilon_1(\omega) + \mathrm{i}\varepsilon_2(\omega). \tag{2.13}$$

By use of (2.12) we can rewrite Eq. (2.10) and get the wave equation for electromagnetic waves in matter

$$\nabla^2 \vec{E} - \mu_0 \varepsilon_0 \varepsilon(\omega) \frac{\partial^2 \vec{E}}{\partial t^2} = 0. \tag{2.14}$$

The most simple solutions of this equation are plane waves

$$\vec{E}(\vec{r},t) = E_0\,\mathrm{e}^{\mathrm{i}(\vec{k}\vec{r}-\omega t)}, \tag{2.15}$$

where the wave vector $\vec{k} = \frac{\omega}{c}\sqrt{\varepsilon(\omega)}\vec{e}_k$ has been used. $\vec{e}_k$ is a unity vector pointing in the direction of wave propagation. The square root of the dielectric constant is defined as the index of refraction $n^*(\omega)$

$$n^*(\omega) = n(\omega) + \mathrm{i}\,\kappa(\omega) = \sqrt{\varepsilon(\omega)}. \tag{2.16}$$

Using this, Eq. (2.15) becomes

$$\vec{E}(\vec{r},t) = E_0\,\mathrm{e}^{\mathrm{i}(\frac{\omega}{c}n(\omega)\vec{e}_k\vec{r}-\omega t)} \cdot \mathrm{e}^{-\frac{\omega}{c}\kappa(\omega)\vec{e}_k\vec{r}}. \tag{2.17}$$

The last term describes the exponential damping of the propagating wave. Since the intensity of the light is proportional to the square of the field, we get

$$I(x) = I_0\,\mathrm{e}^{-\alpha x} \tag{2.18}$$

with the absorption coefficient α

$$\alpha(\omega) = \frac{2\omega}{c}\kappa(\omega). \tag{2.19}$$

2.2.1 Frequency dependence of the dielectric function

The dielectric function can for example be described by the Drude formula [Jac83]

$$\varepsilon(\omega) = 1 + \frac{Nq^2}{\varepsilon_0 m^*}\sum_j \frac{f_j}{\omega_{0j}^2 - \omega^2 + \mathrm{i}\,\gamma_j\omega}. \tag{2.20}$$

This formula is based on the assumption that the absorption is caused by j microscopic oscillators with resonance frequencies ω_{0j}, oscillator strengths f_j and damping coefficients γ_j. As can be seen from the Drude formula, ε approaches unity for $\omega \to \infty$. The static dielectric constant $(\omega = 0)$ strongly depends on the number j and the strengths f_j of oscillators. The higher j the higher $\varepsilon(0)$. The oscillators must be able to couple to the electric field of the wave to contribute to ε. Such oscillators can be atomic vibrations in polar crystals or molecules or oscillations of free electrons around the fixed ion cores. From a quantum mechanical point of view, this interaction between light and matter gives rise to new quasi-particles. In the case of free electrons the quasi-particles are called plasmons, in the case of

optical phonons, they are called phonon-polaritons [Kli95, Kit93]. The latter ones are especially important, since they have frequencies in the infrared region (optical phonon branch near the Brillouin zone center) and form the so called Restrahlenbande [Ash86]. Polaritons are also responsible for the fact that the Maxwell relation

$$n_{\mathrm{opt}} = \sqrt{\varepsilon(0)} \tag{2.21}$$

does not hold for polar crystals (e. g. GaN), where the Lyddane-Sachs-Teller relation

$$n_{\mathrm{opt}}^2 = \varepsilon_0 \left(\frac{\omega_{TO}}{\omega_{LO}}\right)^2 \tag{2.22}$$

has to be used instead. Here ω_{LO} and ω_{TO} are the transverse and longitudinal optical frequencies of the crystal in the zone center. However, for non-polar crystals relation (2.21) still is valid (e. g. diamond). A few examples are given in Table 2.1. Since the energies of the polaritons are in the infrared region, the dielectric constant relevant for capacitance measurements ($\omega < 1$ MHz) is the static one, $\varepsilon(0)$.

In the UV-range, the dielectric constant is dominated by interband transitions of electrons, which give rise to peaks due to the van Hove singularities in the joint density of states [Coh89, Yu96]. From these singularities important information about the electronic band structure can be obtained [Ben98].

2.3 Interaction between defects and bands

2.3.1 Thermal emission and capture

The probability w that a defect in the band gap is occupied by an electron is given by the Fermi-Dirac statistic

$$w = \frac{1}{1 + \mathrm{e}^{(E_T - E_F^T)/kT}}, \tag{2.23}$$

Table 2.1: Comparison between the index of refraction n and the square root of the static dielectric constant $\sqrt{\varepsilon(0)}$. They are directly comparable only for non-polar crystals, for the polar crystal the Lyddane-Sachs-Teller relation gives more accurate results.

Material	$\sqrt{\varepsilon(0)}$	n	$\sqrt{\varepsilon_0}(\omega_{TO}/\omega_{LO})$
Diamond	2.39	2.419	
Si	3.38	3.4	
GaN	3.05	2.4	2.57
NaCl	2.37	1.5	1.54
H_2O	8.96	1.33	

where E_T is the trap level, E_F^T the quasi Fermi level for the traps and kT the temperature. The energy zero is the valence band edge. After having induced a non equilibrium condition (e. .g. a filling pulse in DLTS), the deep traps will relax back to equilibrium much slower than shallow levels. Therefore the occupation statistics during this back relaxation is described by the quasi Fermi level for traps E_F^T. In thermal equilibrium, $E_F^T = E_F$. The rate C of capturing electrons into the defects is given by [Sho52]

$$C = v_{th}\sigma_n n N_T(1-w). \tag{2.24}$$

It is proportional to the electron density n in the conduction band and to the density of empty traps $N_T(1-w)$. v_{th} is the thermal velocity of the electrons and σ_n the electron capture cross section of the defect. The rate G of emitting electrons out of the defect into the band is given by

$$G = \nu_n N_T w. \tag{2.25}$$

It is proportional to the density of electrons trapped in the defects $N_T w$. ν_n is the emission probability or emission constant. Very often it is also called the emission rate, but should not be confused with G.

From the principle of detailed balance, $C = G$, it follows that

$$\nu_n = \frac{v_{th}\sigma_n n(1-w)}{w}. \tag{2.26}$$

Defining the activation energy of the defect by $E_A = E_G - E_T$, where $E_G = E_C - E_V$ is the band gap with the energy zero at E_V, and using $n = N_C \times \exp[(E_F - E_G/2)/kT]$ for the electron density, leads to

$$\nu_n = \underbrace{v_{th}\sigma_n N_C}_{\nu_0}\ \mathrm{e}^{-\frac{E_A}{kT}}. \tag{2.27}$$

Thus, the knowledge of the temperature dependence of the emission probability ν_n provides two characteristics of the trap, namely the activation energy E_A and the capture cross section σ_n.

2.3.2 Optical defect ionisation

The interaction between electrons in a solid and photons of the radiation field can be described in first order by the Hamiltonian [Kli95]

$$H^{(1)} = -\frac{e\hbar}{m^*\mathrm{i}}\vec{A}\cdot\nabla, \tag{2.28}$$

where $\vec{A}$ is the vector potential of the electromagnetic field. For a monochromatic wave we can write [Kli95]

$$\vec{A} = \vec{A}_0 \, \mathrm{e}^{\mathrm{i}(\vec{k}\vec{r}-\omega t)}. \tag{2.29}$$

The use of time dependent perturbation theory [Sch92] leads to a transition between the initial state (here the defect state) ψ_T and the final state (a band state) ψ_b with the transition probability w_{Tb}, which is given by Fermi's golden rule

$$w_{Tb} = \frac{2\pi}{\hbar} \left| \left\langle \psi_b | H^{(1)} | \psi_T \right\rangle \right|^2 \delta(E_j - E_i - h\nu). \tag{2.30}$$

Expanding (2.29) leads to

$$\vec{A} = A_0 \left(1 + \frac{\mathrm{i}(\vec{k}\vec{r} - \omega t)}{1} - \frac{(\vec{k}\vec{r} - \omega t)^2}{2!} + \ldots \right). \tag{2.31}$$

In zero order approximation, only electric dipole transitions are taken into account and the Hamiltonian simplifies to

$$H^{(1)} = -\frac{e\hbar}{\mathrm{i}\, m^*} \vec{A}_0 \nabla \tag{2.32}$$

First order approximation would account for magnetic dipole and electric quadrupole transitions. To eliminate the dependence of the transition rate on $|A_0|^2$, the intensity of the light, the absorption cross section is defined by

$$\sigma_o = \frac{w_{Tb}}{\Phi} \tag{2.33}$$

where $\Phi \propto |A_0|^2 h\nu$ is the photon flux. The delta function in (2.30) has to be replaced by a suitable term proportional to the density of states $\rho(E)$, which results from the integration over the possible final states in the band. All together the spectral shape of the absorption cross section is given by

$$\sigma_o(h\nu) \propto \frac{1}{h\nu} \underbrace{\left| \left\langle \psi_b \left| \frac{\hbar}{\mathrm{i}} \frac{\partial}{\partial \vec{r}} \right| \psi_T \right\rangle \right|^2}_{|M_{Tb}|^2} \rho(h\nu - E_T) \tag{2.34}$$

The absorption coefficient α due to the traps is then given by

$$\alpha(h\nu) = N_T \sigma_o(h\nu) \tag{2.35}$$

where N_T is the trap density.

The spectral shape of the absorption cross section as derived in (2.34) depends on two parts. The matrix element M_{Tb} and the density of states $\rho(E)$. The density of states – around the conduction band minimum – can be very well described by the parabolic approximation of the bands, leading to [Kit93]

$$\rho(E) = \frac{1}{2\pi^2}\left(\frac{2m^*}{\hbar^2}\right)^{3/2}\sqrt{E}, \tag{2.36}$$

where m^* is the effective mass of the charge carriers. However, if the energy of the photon ionizing the defect is much larger than the trap energy E_T, i. e. the charge carrier is excited high into the band, then the assumption of the parabolicity and isotropy of the band does not hold anymore. Effects of band warping and spin orbit coupling on the spectral shape of the absorption cross section have been observed for the Au centre in Si [Gri75]. For the oxygen level in GaAs, transitions to higher lying conduction band minima (L and X) have been observed [Cha81].

To evaluate the matrix element, assumptions about the wave function ψ_T have to be made. For deep levels one usually assumes a delta-function potential [Luc65, Gri75] with the corresponding wave function of its bound state

$$\psi_T(r) = \sqrt{\frac{1}{2\pi a}}\frac{\mathrm{e}^{-r/a}}{r} \tag{2.37}$$

where a is defined by

$$\frac{1}{a} = \sqrt{\frac{2m_T E_T}{\hbar^2}}. \tag{2.38}$$

Here E_T is the energy level of the trap and m_T the mass of the electron bound to the defect. The wave function (2.37) leads to a photoionisation cross section

$$\sigma(h\nu) \propto \frac{(h\nu - E_T)^{3/2}}{h\nu(h\nu + E_T(m_T/m^* - 1))^2}. \tag{2.39}$$

Inksons approach [Ink81] divides the defect wave function into two parts: A core region, where the defect properties dominate and a surrounding region where the properties of the host lattice dominate. In this latter region, ψ_T is basically an evanescent extended state wave function which matches the inner part at the core surface. This approach leads to two groups of absorption cross sections, namely vertical and non-vertical transitions, which contain both allowed and forbidden transitions. The cross sections are given Tab. 2.2. Inkson does not

	vertical	non-vertical
forbidden	$\sigma_A \propto \dfrac{(h\nu - E_T)^{3/2}}{h\nu(h\nu + E_T(m_T/m^* - 1))^2}$	$\sigma_C \propto \dfrac{(h\nu - E_T)^{3/2}}{h\nu}$
allowed	$\sigma_B \propto \dfrac{(h\nu - E_T)^{1/2}}{h\nu(h\nu + E_T(m_T/m^* - 1))^2}$	$\sigma_D \propto \dfrac{(h\nu - E_T)^{1/2}}{h\nu}$

Table 2.2: The four optical photoionisation cross sections in the model of Inkson [Ink81].

give any clues for a choice of m_T. Grimmeis [Gri75] uses the free electron mass, assuming that the extension of the wave function does not exceed a nearest neighbour distance and therefore cannot be influenced by the periodic potential of the lattice. However, Inkson states that the absorption cross section is primarily determined by the evanescent part of the wave function. Since this part of the wave function consists of Bloch functions, it would be justified to set m_T equal to m^*.

As can be seen, the cross section σ_A in Inkson's models is equal to the one of Lucovsky, Eq. (2.39). In Fig. 2.2 the different photoionisation cross sections are plotted for a trap level at 1 eV and $m_T = m^*$.

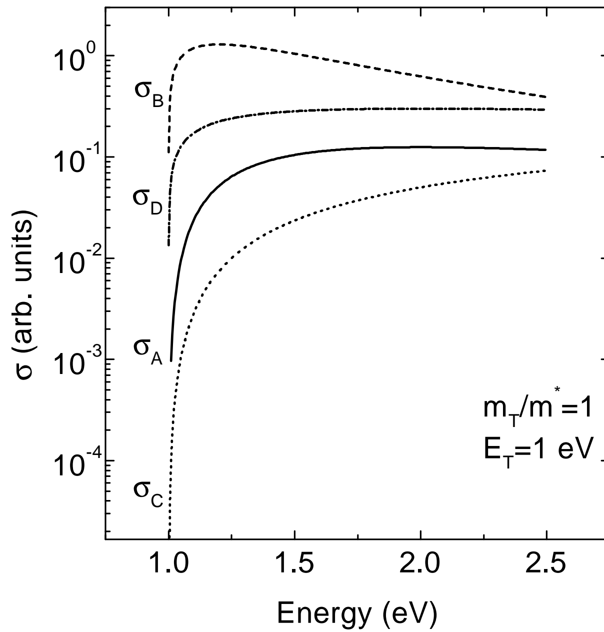

Figure 2.2: Plot of the four calculated photoionisation cross sections after the model of Inkson. As trap energy $E_T = 1$ eV and $m_T = m^*$ has been used.

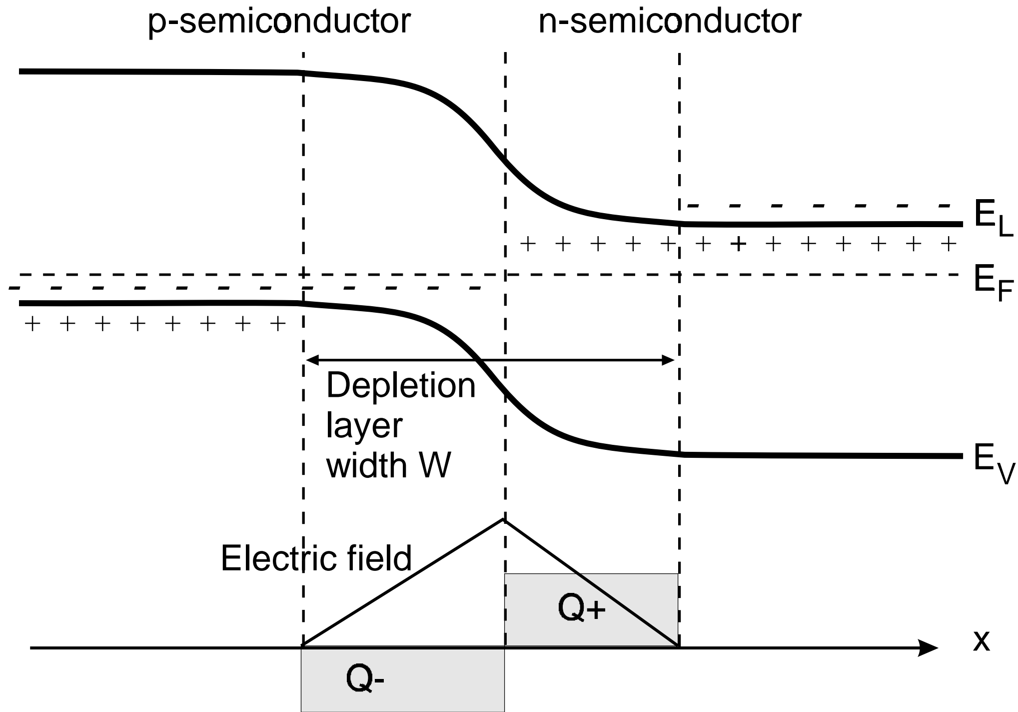

Figure 2.3: Schematic band diagram of a $p-n$ junction. In the lower graph the space charge and the electric field is shown in the Schottky approximation.

2.4 The space charge region

When a p-type and a n-type semiconductor are brought together, a depletion layer forms due to charge carrier drift and diffusion processes [Sze85]. This depletion layer contains spatially fixed charge, namely the ionised donors and acceptors, which form the space charge in the depletion layer. This space charge causes a band bending which is responsible for the rectifying behaviour of a $p-n$ junction. A schematic diagram of such a diode is shown in Fig. 2.3. The width of this depletion layer or space charge region for an abrupt $p-n$ junction can be varied by an external voltage and is given by [Sze85]

$$W = \sqrt{\frac{2\varepsilon}{q}\left(\frac{N_A+N_D}{N_A N_D}\right)(V_{bi}+V_{rev})} \tag{2.40}$$

where

N_A, N_D : acceptor and donor density

ε : static dielectric constant of the semiconductor

q : elementary charge

V_{bi} : build-in-potential

V_{rev} : externally applied potential in reverse direction

In case of a one sided abrupt junction, for example $p^+ - n$ (i. e. $N_A \gg N_D$), the depletion layer width can be approximated by

$$W = \sqrt{\frac{2\varepsilon(V_{bi} + V_{rev})}{qN_D}}. \quad (2.41)$$

The total charge Q stored in the depletion layer of a diode with area A is given by

$$Q = N_D W A. \quad (2.42)$$

With this voltage dependent charge we can define the differential capacitance C of the diode

$$C = A\frac{\partial Q}{\partial V} = A\sqrt{\frac{q\varepsilon N_D}{2(V_{bi} + V_{rev})}}. \quad (2.43)$$

Using Eq. (2.41) leads to

$$C = \varepsilon\frac{A}{W} \quad (2.44)$$

which corresponds to the capacitance of a plate capacitor with a dielectric material with ε and a distance W of the plates. Eq. (2.43) describes the $C - V$ characteristic of an ideal diode. From this $C - V$ behaviour it follows that $1/C^2$ is a linear function of V_{rev}, since

$$\frac{1}{C^2} = \frac{2(V_{bi} + V_{rev})}{q\varepsilon N_D}. \quad (2.45)$$

The condition $1/C^2 = 0$ (the intersection with the abscissa) immediately provides to the built-in voltage. Differentiating (2.45) with respect to the voltage gives the donor density

$$N_D = \frac{2}{q\varepsilon}\frac{1}{d(1/C^2)/dV}. \quad (2.46)$$

In case of an inhomogeneous doping density $N_D(x)$, its profile can be measured using $C - V$ profiling. After (2.46) N_D is a function of V, but using (2.41) V is a function of the actual depletion layer width. Therefore, one can plot N_D versus W and obtain the spatially resolved doping density. However, the region which can be probed is limited to the range of possible depletion layer widths. These limits are given by the onset of a significant current in forward direction and the junction breakdown in reverse direction.

A Schottky diode on a n-type semiconductor can be regarded as an abrupt $p^+ - n$ junction too, since the space charge region in the metal is – due to the high electron density –

only a few monolayers thick. Therefore the same equations for the depletion layer width and the capacitance apply. However, a Schottky contact, especially for space charge spectroscopy, is superior to an abrupt $p^+ - n$ junction. In the latter, both, minority and majority carriers are involved in current transport, whereas in a Schottky diode only majority carriers play an important role. Therefore the Schottky diode is a more simple system to study basic semiconductor properties.

CHAPTER 3

Experimental Methods

In this chapter principles and experimental details of the capacitance measurement are presented. Furthermore the idea and experimental implementation of (optical) Deep Level Transient Spectroscopy and its data analysis methods are described.

3.1 Capacitance measurement

The capacitance is generally defined as a differential value by the relation

$$C = \frac{\partial Q}{\partial V}, \tag{3.1}$$

i. e. the ratio of the incremental amount of charge ∂Q that can be stored by an incremental voltage change ∂V. This ability of storing charge induces a phase shift of +90° between current and voltage of an alternating current applied to the capacitor. As shown in Chapter 2.4, the same is valid for a diode, since charge is stored in the depletion layer. The frequency dependent complex impedance of an ideal capacitor is given by

$$Z_C = \frac{1}{\mathrm{i}\omega C} \tag{3.2}$$

where ω is the angular frequency of the applied voltage. However, the equivalent circuit of a real diode consists of a capacitor plus a series resistance R_S and a parallel resistance R_P (cf. Fig. 3.1). Therefore, the impedance of a real diode is given by

$$Z(\omega) = R_S + \frac{1}{1/R_P + \mathrm{i}\omega C}, \tag{3.3}$$

which can be separated into a real part Z_x

$$Z_x(\omega) = R_S + \frac{1}{1/R_P + \omega^2 C^2 R_P}, \tag{3.4}$$

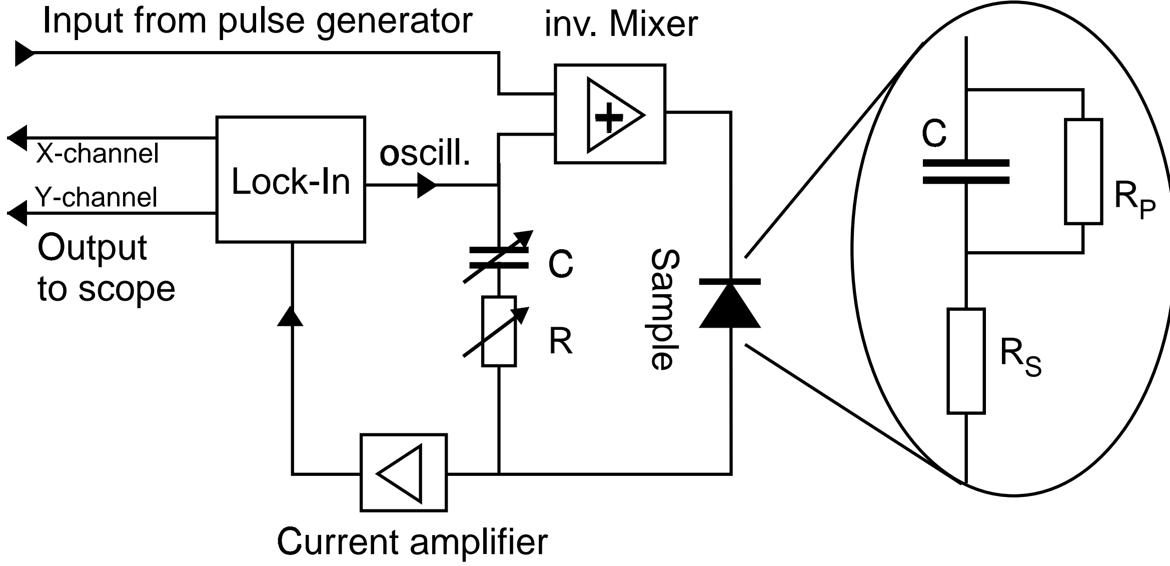

Figure 3.1: Block diagram of the capacitance detection unit. In the inset, the equivalent circuit of a real diode is shown.

and an imaginary part Z_y

$$Z_y(\omega) = \frac{-\omega C}{1/R_P^2 + \omega^2 C^2}. \tag{3.5}$$

Applying a sinusoidal voltage of the form $U(t) = U_0 \sin(\omega t)$ to the diode, results in a current which has both imaginary and real parts. However, at a given frequency ω, it is generally not possible to determine all three diode parameters C, R_S and R_P, since only the imaginary and real part of the current are experimentally available. Therefore one has to neglect one of the resistances (R_P or R_S) and can then determine C and the remaining resistance using the following relations.

$$\left.\begin{aligned} C_S &= \frac{I_y((I_x/I_y)^2+1)}{\omega U_0} \\ R_S &= \frac{U_0}{I_x((I_x/I_y)^2+1)} \end{aligned}\right\} \quad \text{if} \quad R_P \to \infty \tag{3.6}$$

$$\left.\begin{aligned} C_P &= \frac{I_y}{\omega U_0} \\ R_P &= \frac{U_0}{I_x} \end{aligned}\right\} \quad \text{if} \quad R_S = 0 \tag{3.7}$$

where I_x and I_y are the real and imaginary part of the complex current, respectively.

The experimental setup for measuring the capacitance is shown in Fig. 3.1. The oscillator of the Lock-In amplifier provides the test signal (amplitude U_0 and frequency ω) which is

then added to a DC bias voltage, supplied by a pulse generator. The negative sum of these voltages is applied to the diode. The resulting current through the diode is detected, amplified and converted into a voltage by a current amplifier. This voltage is fed into the input of a two phase Lock-In amplifier, which allows to measure the real and complex part of the current.

It will be shown later that for DLTS measurements, it is necessary to detect small changes of the capacitance on a large offset value. Therefore it is essential to compensate the offset capacitance. This is done by adding an adjustable capacitor parallel to the inverting mixer and the diode under test. Now the currents flowing through the two capacitors cancel each other in the current amplifier, since they are 180° out of phase. The resulting output is zero, only small deviations of the capacitance of the diode under test produce an output signal.

Experimentally, this capacitance detection unit was built up using an EG&G 5301 Lock-In amplifier operating from 10 Hz to 100 kHz and an HMS 541 current amplifier with variable current amplification from 10^4A/V to 10^{10}A/V. The mixer is a home-built device, using an Texas Instruments TLE 2142 operational amplifier, operating at unity gain. This device offers a high slew rate of 27V/μs, which enables short filling pulses with a high voltage swing. The filling pulses are provided by a Hewlett-Packard 8110A pulse generator.

Additionally, a Boonton 7200 commercial capacitance meter operating at 1 MHz was used for high frequency measurements. It also provides the possibility to compensate the offset capacitance by an external capacitor.

3.2 Performance of the setup

3.2.1 Frequency behaviour

The highest possible test frequency of the capacitance detection unit used here is limited by the bandwidth of the current amplifier. In order to determine this upper limit, a ceramic capacitor was fitted into the sample holder instead of a sample and the frequency dependent conductance was measured. The results for amplifications 10^4A/V, 10^5A/V and 10^6A/V are shown in Fig. 3.2. As can be seen, the conductance exhibits a linear behaviour from 50 Hz up to 20 kHz, as it is expected from relation (3.2). For the highest amplification, an overshoot at 50 kHz is observed, due to the limited gain-bandwidth product. Although the conductance rises linear with frequency and is therefore purely capacitive, the phase is not constant at 90° over the whole frequency range as it should be for a purely complex impedance. For low frequencies, the phase is 90°, but it drops to zero and even negative values for high frequencies. This is another artefact of the limited gain-bandwidth product of the current amplifier. However, for the capacitance measurement as described above, it is essential that the real as well as the complex current are amplified linearly and that no phase

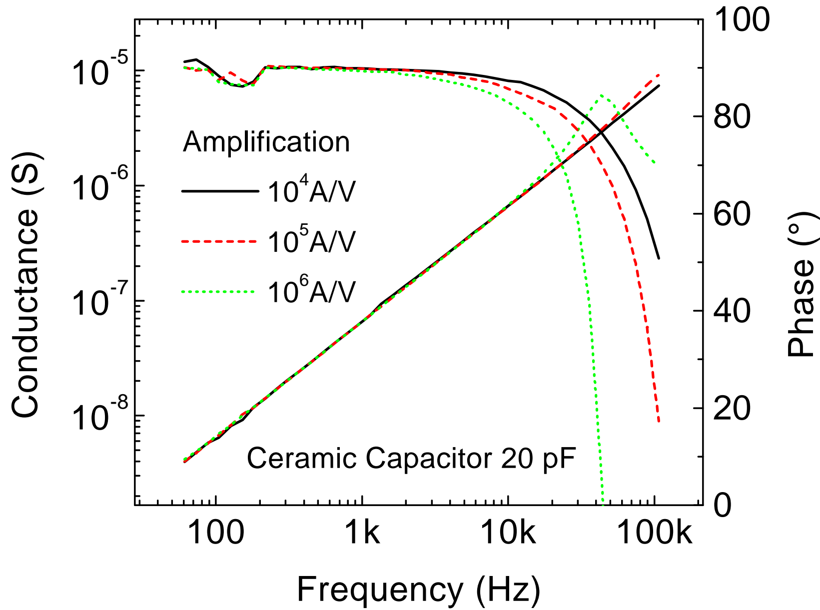

Figure 3.2: Frequency dependent conductance of a ceramic capacitor (nominally 20 pF). The phase shift is as measured by the Lock-In amplifier.

shift is introduced, since this would lead to wrong values of the deduced capacitance. For a given acceptable error of 3% this limits the upper frequency to the point, where the phase falls below 75°. For the amplifications 10^4A/V, 10^5A/V and 10^6A/V this gives 48 kHz, 34 kHz and 19 kHz, respectively.

3.2.2 Time behaviour

In Deep Level Transient Spectroscopy (DLTS), the temporal evolution of the capacitance is measured. Therefore it is important to know the settling times of the setup itself after voltage pulses and the drift of a steady state value. The settling time of the Lock-In setup strongly depends on the selected time constant of the Lock-In amplifier. It ranges from 10 ms to several seconds. The Boonton capacitance meter has a settling time of 150 μs. The drift of the steady state value is 2×10^{-6} pF/sec. Another limiting factor of the equipment is the slew rate of the pulse coupling circuits, which limits the duration of the filling pulse that can be applied to the diode. The slew rate of the Boonton is 20V/msec. For the Lock-In setup, the crucial device is the mixer. Its slew rate is given by the one of the operational amplifier, which is 27V/μs.

3.3 Choosing the test frequency

As described above, the choice of the test frequency is important to perform reliable capacitance measurements. Besides the limited frequency range of the setup, physical properties of the sample are important, which will be discussed in the following. Considering the equiva-

lent circuit of a diode as shown in Fig. 3.1 it is clear that for very high frequencies, where the impedance of the capacitor vanishes, the impedance of the diode is dominated by the series resistance R_S. For $\omega \to 0$, the impedance is given by the sum of R_S and R_P. In these cases the phase will be near to zero and small changes of the capacitance will not be detectable. For this reason, an intermediate frequency should be chosen, where the impedance is dominated by the capacitive part. Analytically, the useful test frequency range can be determined by (assuming $R_P \gg R_S$)

$$\frac{1}{2\pi R_P C} = f_c^l < f_{\text{test}} < f_c^u = \frac{1}{2\pi R_S C}. \quad (3.8)$$

For example, a diode with a capacitance of 100 pF and series resistance of 50 kΩ gives an upper cut-off frequency f_c^u of 31 kHz. In practice, the values R_S, R_P and C are not known in advance, therefore the experimental access to the test frequency will be the following. The frequency dependent conductance and phase is measured and plotted versus frequency. The region where the conductance exhibits a linear behaviour and the phase shows a maximum is suitable for capacitance measurements. If the frequencies f_c^u and f_c^l are so close together that the phase does not reach an acceptable value (i. e. above 73°) one has to increase or decrease the frequency slightly to ensure that the Ohmic part of the impedance is dominated by either the series or the parallel resistance. The capacitance can then be calculated accurately using the relations (3.6) and (3.7).

Another point which has to be taken into account when choosing the test frequency is the the emission rate of the defects. The test level wobbles the edge of the depletion layers and the current due to the flowing charge determines the measured capacitance. However, this can only happen when the charge carriers can follow the test signal. Therefore the emission rate of the shallow defects must be larger than the inverse test frequency. Using the relation (2.27) and a typical phonon frequency of 10^{13} s^{-1} for the prexponential factor ν_0 leads at 200 K to an emission rate of 3×10^3 s^{-1} for the boron acceptor in diamond ($E_A = 370$ meV) and 3×10^{12} s^{-1} for a dopant impurity with $E_A = 20$ meV. In the first case the 1 MHz of the Boonton capacitance meter would be much too high, and one has to reduce the test frequency to below 1 kHz.

An example is shown in the right column of Fig. 3.3. Here, the frequency dependent conductance and phase for three temperatures of a Schottky diode on boron doped diamond is shown. At room temperature the conductance is linear over the whole frequency range, as expected for a purely capacitive signal. In the phase plot, a decrease at low frequencies can be seen, indicating the influence of a finite parallel resistance. At lower temperatures, the conductance deviates from a linear function, establishing a constant value for frequencies higher than the cut-off frequency f_c^u. The same effect can be seen in the phase, which drops from 90° to 0° for $f > f_c^u$. This cut-off frequency shifts to lower values with decreas-

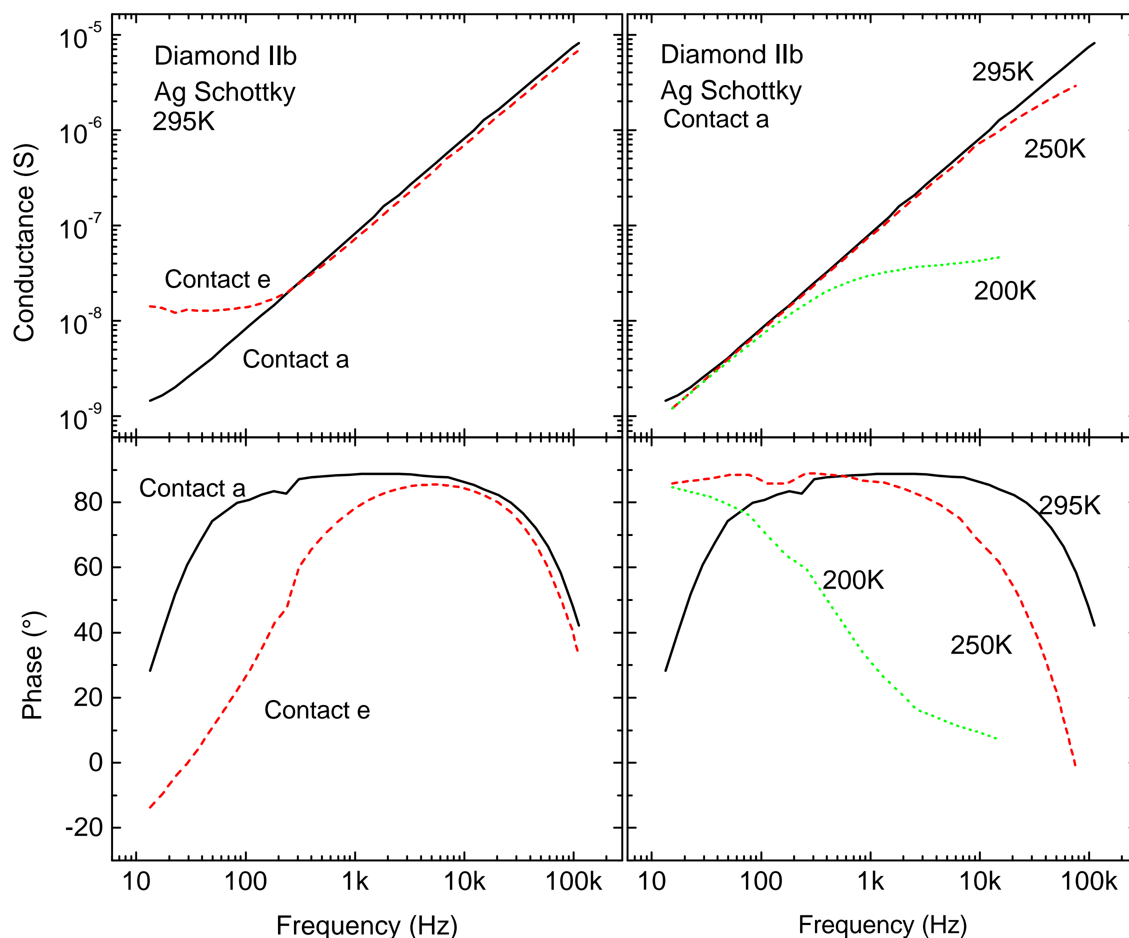

Figure 3.3: Left graphs : Conductance and phase of two different Schottky diodes on diamond at room temperature. The dashed one (contact e) has a significant (i. e. small) parallel resistance. Right graphs : One diode at three different temperatures. The increasing influence of the series resistance with decreasing temperature can be seen.

ing temperature, due to the increasing series resistance. In contrast, the phase shift at low frequencies increases with decreasing temperature due to the increasing parallel resistance.

The effect of a parallel resistance can be seen more clearly for two different diodes at room temperature, shown in the left column of Fig. 3.3. Here the phase rises from 0° to 90° with increasing frequency. At the same point, the frequency dependence of the conductance changes from constant (R_P is the dominating impedance) to linear (C is the dominating impedance). Obviously R_P is smaller for the dashed line than for the solid line.

3.4 Transient space charge spectroscopy

In Chapter 2.4 it was shown that the depletion layer width W of a Schottky diode on a uniformly doped semiconductor is given by

$$W = \sqrt{\frac{2\varepsilon_S(V_{bi}+V)}{qN_D}}, \tag{3.9}$$

where N_D is the shallow donor concentration. However, if there are additional charged defects with concentration $N_T^{\pm}$, they also contribute to the capacitance. Then Eq. (3.9) has to be modified to

$$W = \sqrt{\frac{2\varepsilon_S(V_{bi}+V)}{q(N_D \mp N_T^{\pm})}}. \tag{3.10}$$

Positively charged defects increase the total net charge in the depletion layer and therefore its width decreases. Negatively charged defects partially compensate the positive donors and therefore the depletion layer width increases. Using the relation $C = \varepsilon_S A/W$ and assuming that $N_D \gg N_T^{\pm}$ one can expand the square root in (3.10). This leads to

$$C = C_0\left(1 \mp \frac{N_T^{\pm}}{2N_D}\right) \tag{3.11}$$

where

$$C_0 = A\sqrt{\frac{q\varepsilon_S N_D}{2(V_{bi}+V)}} \tag{3.12}$$

is the capacitance without traps.

The principle of any space charge transient spectroscopy is to induce a metastable charge state of the defects and to observe their relaxation back to thermal equilibrium. In most cases the non-equilibrium situation is established by reducing the reverse voltage applied to the diode (filling pulse). This will cause the defects located at the edge of the depletion layer to capture an electron (Fig. 3.4a) and b)). After a certain time (the filling pulse duration), the reverse bias is restored. The defects which have captured an electron are now in a non-equilibrium charge state. Due to this unstable occupation, electrons will be emitted from the defects into the conduction band and will be swept out of the depletion layer (Fig. 3.4c)). This changes the total amount of charge in the depletion layer, which is reflected via (3.11) in the capacitance. Thus, measuring the temporal evolution of the capacitance provides two informations.

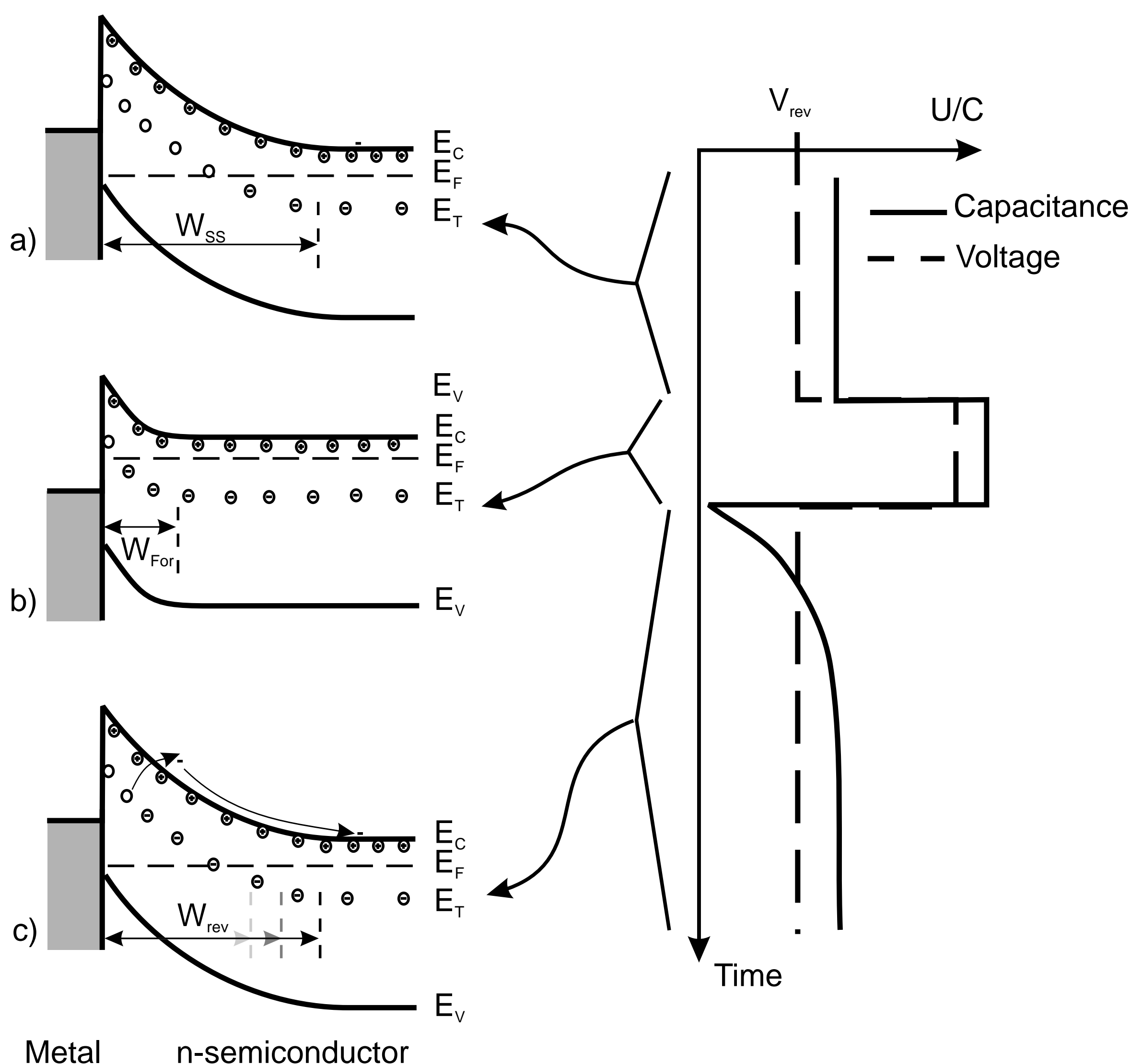

Figure 3.4: The course of a filling procedure. a) The diode is in thermal equilibrium corresponding to the applied reverse bias b) during filling pulse c) immediately after the filling pulse, the traps start to emit. It is assumed that trap filling is much faster than thermal emission.

First, the total change in capacitance yields the total amount of traps whose occupancy was changed during filling : Assuming that only one charge carrier is emitted from each defect, the change in capacitance ΔC is given by

$$\Delta C = C_0 \left(1 \mp \frac{N_T^{\pm}}{2N_D} \right) - C_0 = \mp \frac{C_0 N_T^{\pm}}{2N_D}, \tag{3.13}$$

which yields the trap density

$$N_T^{\pm} = 2N_D \frac{\Delta C}{C_0}. \tag{3.14}$$

However, this formula was derived using the assumption $N_D \gg N_T$. If this approximation does not hold, one has to use the full expression

$$C = C_0 \sqrt{1 - \frac{N_T}{N_D}}. \tag{3.15}$$

Assuming $N_T(t \to \infty) = 0$ (i. e. complete emptying of traps) we get

$$\frac{\Delta C}{C_0} = 1 - \sqrt{1 - \frac{N_T}{N_D}}, \tag{3.16}$$

which leads to

$$N_T = \left[1 - \left(1 - \frac{\Delta C}{C_0}\right)^2\right] N_D. \tag{3.17}$$

The second information is the emission rate of the defects. It can be deduced from the kinetics of the emission process. As it was shown in Chapter 2.3.1, the emission rate ν for electrons out of a defect into the conduction band is described by

$$\nu = v_{th} \sigma_n N_C \, \mathrm{e}^{E_A/kT}. \tag{3.18}$$

Therefore, the knowledge of the temperature dependent emission rate provides information about the activation energy E_A and the capture cross section σ_n. According to the principle of detailed balance, in thermal equilibrium the emission rate is equal to the capture rate. However, after the filling pulse, the defect is in a non-equilibrium state and the emission rate will overcome the capture rate. The simplest rate equation describing such an emission process is

$$\frac{dN}{dt} = -\nu N, \tag{3.19}$$

where N is the number of traps which are metastably occupied by a electrons. The solution is an exponential function

$$N(t) = N_T \, \mathrm{e}^{-\nu t}, \tag{3.20}$$

where N_T results from the initial condition and, assuming complete filling, represents the trap density. Substituting (3.20) into Eq. (3.11) leads to

$$C(t) = C_0 \left(1 - \frac{N_T}{2N_D} \, \mathrm{e}^{-\nu t}\right). \tag{3.21}$$

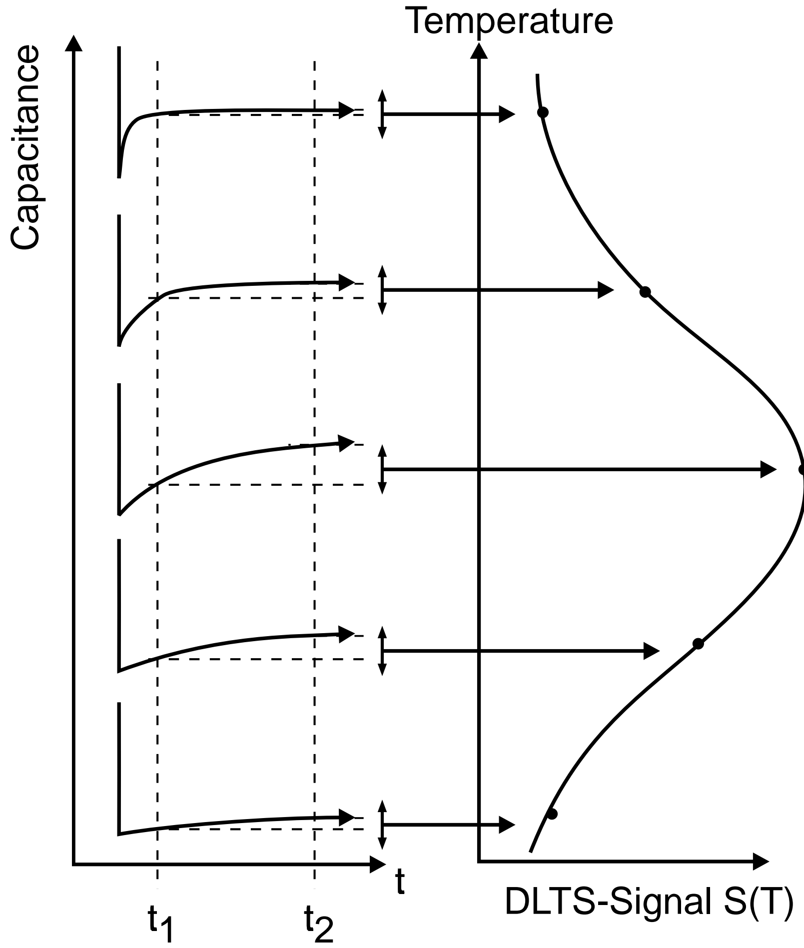

Figure 3.5: Origin of a DLTS peak. Left : Transients at different temperatures with the rate window given by t_1 and t_2. Right : The resulting DLTS signal $S(T)$.

3.4.1 The rate window concept

To extract the actual emission rate from the measured transient, a variety of methods have been proposed. The first one, originally invented by Lang [Lan74], is used in this work and will be discussed now in detail.

The DLTS signal S is defined by the difference of the capacitance at the times t_1 and t_2

$$\begin{aligned} S(t_1,t_2) &= C(t_2) - C(t_1) \\ &= \frac{C_0 N_T}{2N_D}\left(\mathrm{e}^{-\nu t_1} - \mathrm{e}^{-\nu t_2}\right). \end{aligned} \tag{3.22}$$

t_1 and t_2 define the so called rate window. We consider now the signal S for a fixed rate window, but varying emission rate ν. This is the case when the samples temperature is changed and ν rises exponentially following Eq. (3.18) (c.f. Fig. 3.5). At low temperatures

$S \approx 0$, since no electrons are thermally emitted from the traps. The same is true for high temperatures, since all electrons have already been emitted before t_1. However, for temperatures where the emission rate equals the rate window, the signal goes through a maximum. The emission rate corresponding to the maximum of the DLTS signal is given by setting the derivative of Eq. (3.22) with respect to ν equal to zero, thus

$$\frac{1}{\nu} = \frac{t_1 - t_2}{\ln(t_1/t_2)}. \tag{3.23}$$

Changing the values of t_1 and t_2 changes the rate window and the peak of the DLTS signal shifts. The maximum is characterized by the temperature (T_m) where it occurs for a given emission rate ν. For a series of scans with different rate windows one gets a set of (T_m, ν) data pairs, which are plotted into an Arrhenius diagram. The activation energy E_A for thermal emission is determined from the slope of such a plot. To account for the temperature dependence of the pre-exponential factor ν_0 ($v_{th} \sim T^{1/2}$ and $N_C \sim T^{3/2}$) in (3.18), $\ln \nu/T^2$ instead of $\ln \nu$ is plotted versus $1000/T$. The capture cross section is assumed to be temperature independent, which, however, may be a very crude approximation, especially for defects with a capture barrier.

In the rate window method described above, the experimental procedure would be as follows: Set a rate window by fixing t_1 and t_2 and measure the signal S while scanning the temperature. This is repeated many times for different rate windows. Since the temperature scanning rate should not be too high, this is a very time consuming measurement. It is much faster to fix the temperature and scan the rate window. In addition, to increase the signal to noise ratio, the capacitance is not sampled at a certain time t_1 and t_2 but is integrated over a time domain Δt around t_1 and t_2.

A more general approach to the analysis of a DLTS signal is the concept of a weighting function, where the DLTS signal S is defined by

$$S = \int_0^{T_C} C(t) W(t, \nu) dt, \tag{3.24}$$

where T_C is the observation time and W the weighting function, which depends on t and defines ν. For the rate window concept, W is just the sum of two δ-functions $W_{\text{Lang}} = \delta(t - t_1) - \delta(t - t_2)$ and therefore defines the rate window via Eq. (3.23). There have been a lot of other weighting functions proposed. For example one is the exponential $W_{\text{exp}} = A\, \mathrm{e}^{-\nu t}$, which rejects noise most efficiently, but gives a more broader DLTS peak than W_{Lang} [Mil75]. In addition, the DLTS signal S is sensitive to T_C which influences the measured emission rate. Based on the Gaver-Stehfest algorithm of the inverse Laplace transform, the weighting functions W_{GS4} and W_{GS6} have been proposed [Ist97], which have

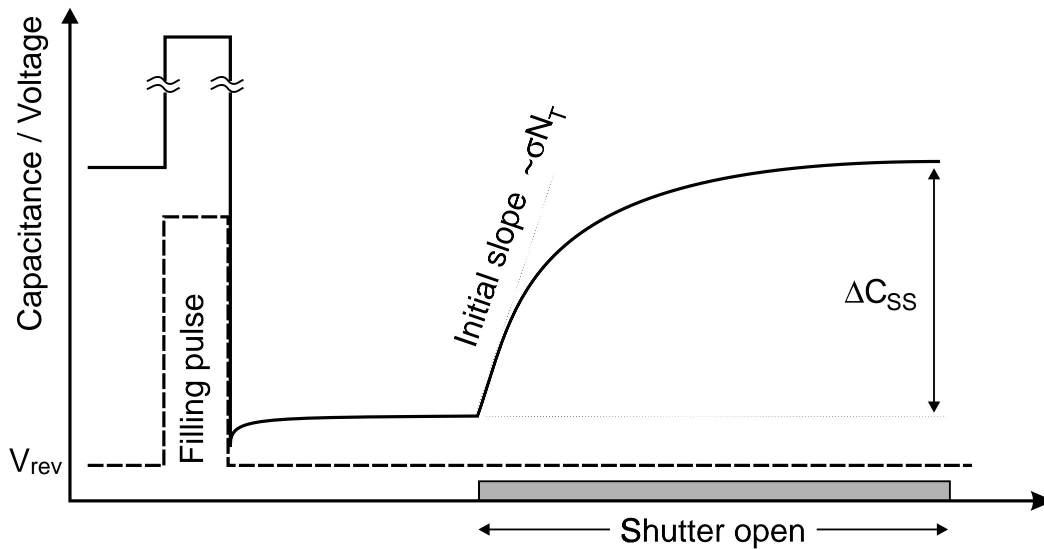

Figure 3.6: The course of a ODLTS measurement. During the shaded time, the shutter is opened and the transient is recorded.

been shown to give very narrow DLTS peaks. This allows to resolve possible substructures of a DLTS signal. Indeed, this has been successfully demonstrated by Dobaczewski and Kaczor [Dob94] for the EL2 defect in GaAs. However, the signal to noise ratio of the capacitance transients must exceed 2000 for those weighting functions to give a meaningful signal [Ist97].

3.4.2 Optical emission

Although the DLTS technique as described above is a powerful tool in studying deep defects, it has certain limitations. Considering Eq. (3.18), it is obvious that for very deep traps (i. e. $E_A > 1$ eV) the emission rates at reasonable temperatures become very small. To overcome this limitation, monoenergetic light is used to change the charge state of the defects by optical excitation. This optical DLTS (ODLTS) method can not only be used to excite very deep traps, but is also applicable for traps accessible to thermal DLTS, since it provides additional information, which cannot be probed by thermal DLTS, most importantly spectrally resolved photoionisation cross sections of deep traps. From this data one can extract information about the coupling of the defect to the lattice, non-parabolicity of the valence band and higher conduction bands.

Since the charge carriers are emitted optically in ODLTS, the temperature is chosen to be low enough so that thermal emission can be neglected during the observation period. The procedure of recording an ODLTS transient is as follows (cf. Fig. 3.6). After the filling pulse, the diode is brought back to reverse bias. Then, a delay of a few seconds allows the very

shallow traps to emit their charge carriers. After this delay, light is shone onto the diode and the capacitance transient is recorded. The form of the transient is in principle again described the kinetics given by Eq. (3.20), where the emission rate ν has to be replaced by

$$\nu_o = \sigma_o \Phi, \tag{3.25}$$

where σ_o is the photoionisation cross section and Φ is the photon flux. This results in a transient of the form

$$C(t) = C_0 \left(1 - \frac{N_T}{2N_D}\, \mathrm{e}^{-\sigma_o \Phi t}\right). \tag{3.26}$$

In contrast to thermal DLTS, in ODLTS the variation of the emission rate ν_o is done by sweeping the energy of the incident photons, instead of varying the temperature. An ODLTS experiment thus provides two kinds of information: (i) The energetically resolved trap density via the amplitude of the transient and (ii) the spectrally resolved photoionisation cross section σ_o via the emission rate ν_o. The latter contains most of the optical absorption properties of a defect. Its spectral form has been discussed in Section 2.3.2. To extract the amplitude and the emission rate from the transient, two methods are commonly used [Cha81, Göt95] which will be discussed in the following.

Initial slope analysis

Expanding the exponential function in (3.26) to first order results in

$$C(t) \approx C_0 \left(1 - \frac{N_T}{2N_D}(1 - \nu_o t)\right), \tag{3.27}$$

which is a good approximation for $t < 1/\nu_o$. The slope of the transient is then given by

$$\left.\frac{dC}{dt}\right|_{t<1/\nu} = \nu_o \frac{C_0 N_T}{2N_D}. \tag{3.28}$$

Substituting ν_o by Eq. (3.25) leads to

$$\left.\frac{dC}{dt}\right|_{t<1/\nu} \sim \sigma_o N_T \Phi. \tag{3.29}$$

Thus, the spectral dependence of the initial slopes normalized to the photon flux Φ is proportional the product $\sigma_o N_T$, which is the absorption coefficient of the sample. If one knows in

addition the trap density N_T (e. g. from thermal DLTS or steady state analysis in ODLTS), the absolute values of the photoionisation cross sections can be calculated.

A fit of a theoretical photoionisation cross section to an ODLTS spectrum obtained by this method yields the the energy position in the gap of the defect causing the absorption. If, in addition, the electron-phonon coupling is taken into account, information about the vibronic properties of the defect can be obtained (See Sec. 7.1).

Assuming that the ionisation energy of a defect is spatially varying due to e. g. strain, or that a defect distribution is present, the time dependent capacitance has to be written as

$$C(t) = C_0 \left(1 - \frac{1}{2N_D} \int_{E_V}^{E_C} \rho_T(E)\, \mathrm{e}^{-\nu(E)t} dE \right), \tag{3.30}$$

where $\rho_T(E)$ is the defect density of states, satisfying $\int_{E_V}^{E_C} \rho_T(E) dE = N_T$. For the initial slope of the transient the expression

$$\left. \frac{dC(h\nu)}{dt} \right|_{t<1/\nu} \propto \int_{E_V}^{E_C} \rho(E) \sigma_o(h\nu, E) dE \tag{3.31}$$

can be calculated. From this equation it is clear that a defect distribution broadens the rising flank of the measured photoionisation with respect to the photoionisation cross section σ_o of a sharp defect energy.

Steady state analysis

Complementary to the method described above, a second approach to analysing the transient is based on times much larger than the time constant of the emission. In this case the transient approaches a steady state $C(t \to \infty)$, since all traps have been ionised. According to Eq. (3.26), the amplitude of the transient is given by

$$\Delta C_{SS} = \frac{C_0 N_T}{2N_D}. \tag{3.32}$$

Since N_D is known from $C-V$ profiling, the trap density N_T can be directly calculated via this relation. In practice, one defines an observation time t_S after the light has been switched on and samples the capacitance at this time. C_{SS} is then given by $C(t_S) - C(t = 0)$. If $t_s < 1/\nu_o$, then C_{SS} is ≈ 0. If $t_S \gg 1/\nu_o$, C_{SS} will be given by Eq. (3.32). A ΔC_{SS} ODLTS spectrum obtained in this way will exhibit steps at a photon energy corresponding roughly to the energetic position of the trap, establishing a plateau for photon energies $h\nu > E_T$. From the step height the trap density of the individual defects can be calculated after (3.32).

If the photon energy exceeds the barrier height of the Schottky contact, internal photoemission occurs [Fow31]. This results in an increased current density through the depletion layer. One consequence is a capture of photogenerated charge carriers by the defects. As an effect, the traps will not be emptied completely and the steady state value of the capacitance will be the kinetically determined partial trap occupation, i. e. the trap density will be underestimated. However, an estimation of the ratio of retrapped to photoemitted carriers leads to the conclusion that this effect is negligible for typical trap parameters [Göt95].

Contrary to the initial slope analysis, the energetic position of the trap cannot be determined exactly by this method. Since the optical emission rate of the defect is not a step function of the photon energy, the time constant will by very large for $h\nu \approx E_T$ and decreases as the photon energy increases. Therefore, the capacitance sampled at a time t_s after illumination of the contact will give rise to the correct trap density only of $t_s \gg 1/\nu_o$ and will result in smaller values of N_T for $t_s \geq 1/\nu_o$. In this case it depends on the sampling time as well as on the photon flux, where the threshold of the step appears in the spectrum and how the step is shaped. Therefore, the energy level of the trap determined by the method of initial slopes is more reliable, whereas the actual trap density can only be measured by the steady state method.

3.4.3 Sensitivity

The maximum possible sensitivity of a (O)DLTS measurement is determined by Eqs. (2.43) and (3.14)

$$N_T = 2N_D \frac{\Delta C}{C_0} \stackrel{(2.43)}{=} \frac{2\Delta C}{A}\sqrt{\frac{2N_D(V_{bi}+V_{rev})}{q\varepsilon_S}}. \tag{3.33}$$

In order to detect a very small defect density N_T, ΔC and N_D have to be kept as low as possible. A typical value for ΔC is 0.5 fF to 50 fF depending on the test frequency. The higher the test frequency, the higher the resolution, since the signal increases linearly with frequency. A lower limit for the doping density is the resulting resistivity of the bulk material, which influences the capacitance measurement as discussed in Sec. 3.1. A possible way to overcome this limitation is to decrease the doping density towards the surface of the sample. On the other hand, when the contact area A of the diode is enlarged, the resolution increases. Here again, experimental limitations determine the maximum contact area. For the samples investigated in this work, only contacts of less than 250μm $\times$250μm in size had satisfying Schottky characteristics with a reasonable yield.

For a Schottky diode on type IIb diamond ([B]= 2×10^{16} cm^{-3}) defect densities of the order of 10^{14} cm^{-3} can be detected. However, one can imagine a diode on high quality Si samples where large rectifying contacts are possible (e. g. $A = 1$ mm^2), doped with 10^{14}

cm^{-3}. This leads to a theoretically detectable trap density of as low as 10^9 cm^{-3}. For the geometrical dimensions of this diode this corresponds to an absolute value of about 6000 detected traps.

3.4.4 Type of charge carriers

A peculiarity of the capacitance spectroscopy is the sensitivity to the sign of emitted charge carriers. The emission of minority and majority charge carriers can be clearly distinguished. Consider the case of a Schottky diode on a $p-$type substrate. If holes (majority carriers) are emitted, the net charge in the depletion layer decreases, which causes the capacitance to increase, since the effective acceptor density increases. However, if electrons (minority carriers) are emitted, the signs are reversed and the capacitance decreases. The same is true for a $n-$type substrate, with electrons and holes exchanged. In general the emission of majority carriers increases the capacitance, whereas the capacitance is decreased during emission of minority carriers.

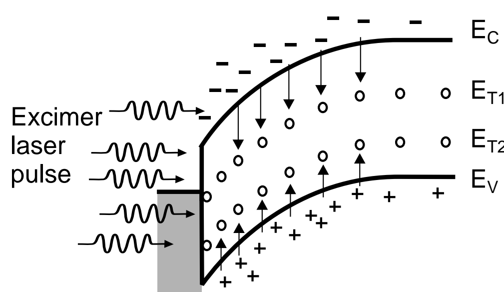

Figure 3.7: Filling of defects with electrons and holes by use of an excimer laser pulse.

An example for such a behaviour is a Au Schottky diode on $p-$type CVD grown diamond. For ODLTS measurements, in addition to the electrical filling pulse optical excitation has been performed by an ArF excimer laser pulse ($h\nu$ =6.4 eV), which is strongly absorbed by the diamond ($E_G = 5.45$ eV, $\alpha(6.4\text{eV}) \approx 5 \times 10^4$ cm^{-1}). This creates holes as well as electrons in the depletion layer, which are captured by the defects. As a consequence, defects above the Fermi level will be occupied by an electron, whereas those below the Fermi level will capture holes, as in the case of a pure electrical filling. This is confirmed by the observation that the capacitance increases after the filling pulse, which means that in addition to the ionised acceptors, negative charge has been brought into the depletion layer. This charge are the electrons captured by the defects above the Fermi level. The optical filling is sketched in Fig. 3.7.

The capacitance transients of the ODLTS measurement for various photon energies of the probing light are shown in Fig. 3.8. For photon energies below 2.5 eV, normal transients (i. e. positive slope) are observed, indicating hole emission. The trap density spectrum obtained from this time domain is shown in Fig. 3.8 (squares). From 2.5 eV on, however, a negative slope can be observed for t >20 sec, due to the emission of electrons into the conduction band. The fact that the negative slope is observable only at relatively long time scales indicates that the photoionisation cross section of this transition is very small. Focusing on those long times for the evaluation the slopes of the transients to determine the absorption

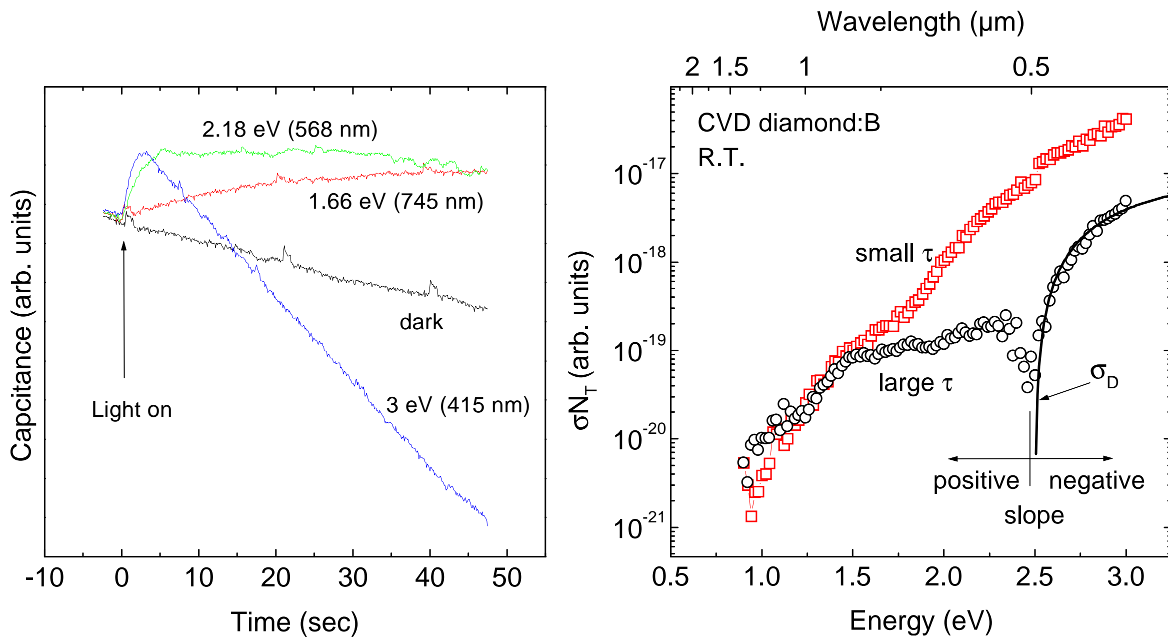

Figure 3.8: The left graph shows capacitance transients after a ArF excimer laser pulse filling. The right graph shows two ODLTS spectra. For the upper one, the slope of the transients has been evaluated for small times. In the lower one the slope for large times has been evaluated. Above 2.5 eV, minority carrier emission is dominant.

coefficient, results in the spectrum shown in Fig. 3.8 (circles). Here the sharp dip at 2.5 eV is caused by the change of sign of the transients' slope. The important issue of this change in sign is the energy position of the defects causing the absorption. When determining this position by fitting an photoionisation cross section to the data, the energy determined by this fit has to be referred relative to the conduction band. Such a fit is also shown in the graph (solid line). The extracted trap energy is 2.5 eV below the conduction band. This ability of distinguishing the type of carriers makes the capacitance spectroscopy superior to other related spectroscopies like photoconductivity.

CHAPTER 4

Experimental Setup

Within the frame of this work, a setup for performing different types of transport measurements has been built. A schematic drawing is shown in Fig. 4.1. The setup is optimized for various kinds of capacitance spectroscopy, such as $C-V$ profiling, Deep Level Transient Spectroscopy (DLTS) and optical induced DLTS (ODLTS). But photoconductivity and dark conductivity experiments can be carried out as well. The sample is placed on a cold finger of an Oxford continuous flow cryostat. The use of liquid helium or nitrogen as coolant allows the temperature to be varied from 5 K to 450 K. The temperature is controlled or ramped by an Oxford ITC503 temperature controller. The stability is better than 0.1 % over the whole range. Electrical connections in the cryostat are made via shielded steel cords. Steel was chosen to minimize heat conduction via the electrical connections, which however, increases the resistance of the cables to 10 Ω. Up to 5 electrical connections can be made to the sample, but due to heat conduction, it is recommended to use as few as possible. The parasitic capacitance of this setup is 60 fF. The sample itself is mounted in a ceramic 8 pin IC socket which enables quick sample change and reliable electrical connections via wire bonding.

The optical part of the setup enables the sample to be illuminated with photons in the energy range 0.56 eV $\leq h\nu \leq$ 3 eV. These photons are provided by a 100 W quartz tungsten halogen lamp in conjunction with a 270M Spex grating monochromator (1/4 m focal length). Appropriate gratings (600 and 1200 lines/mm, blaze wavelength 1100 nm and 550 nm, respectively) are chosen to optimize the throughput. The entrance and exit slit widths can be varied from 50 μm up to 6000 μm which corresponds to a spectral resolution between 0.3 nm and 38 nm for the 600 l/mm grating. The higher diffraction orders of the gratings are cut off by appropriate low pass filters after the monochromator output slit. The image of the output slit is focused via two concave mirrors onto the sample. Mirrors where chosen to avoid chromatic aberrations of dispersive elements like lenses. A small part of the optical beam is coupled out onto a pyroelectric detector to monitor the photon flux. Since pyroelectric elements can only detect chopped light, a chopper wheel was introduced which modulated

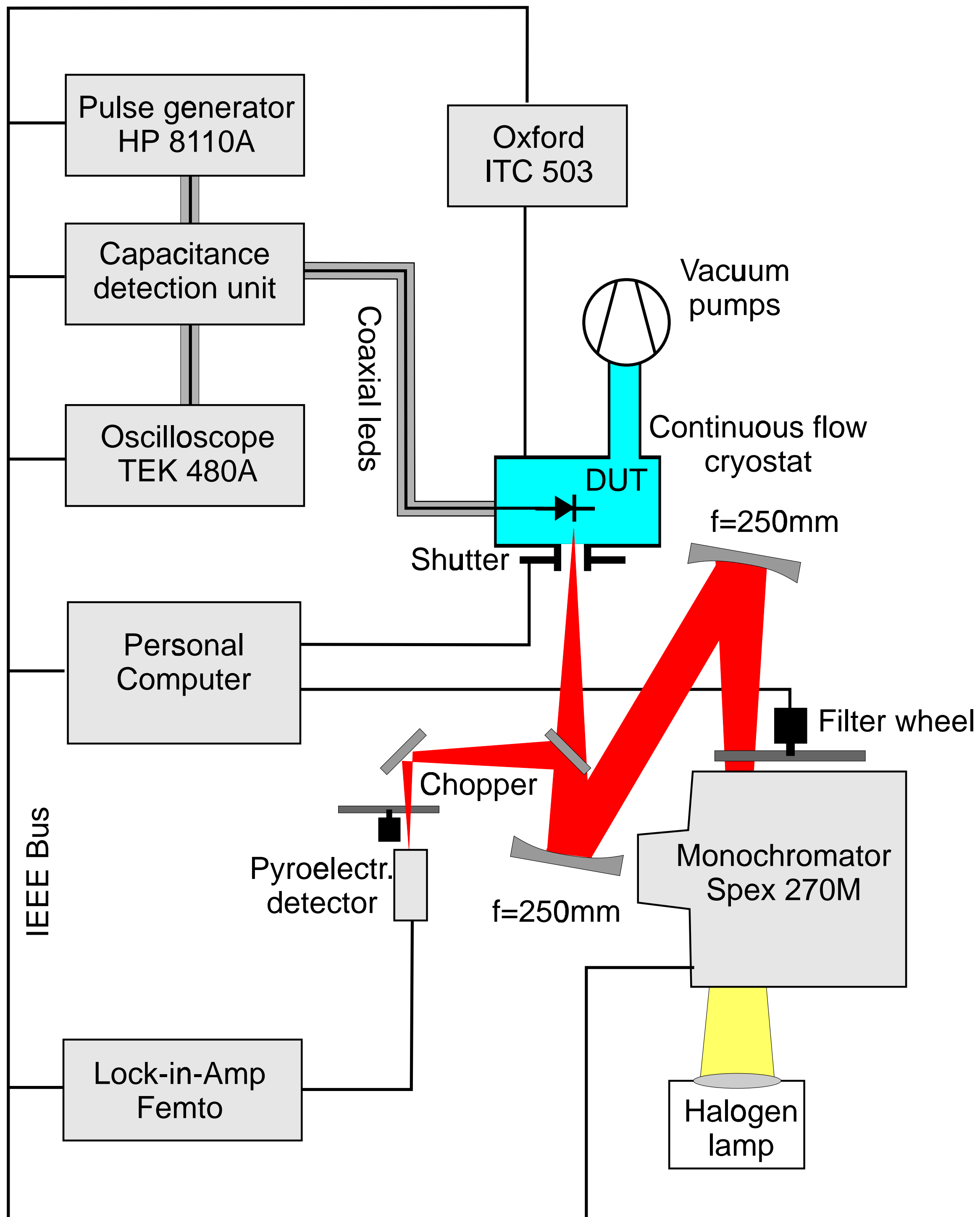

Figure 4.1: Experimental setup of (O)DLTS and photoconductivity experiment.

the beam with 12.8 Hz, where the detector has its maximum sensitivity. The output of the detector was analysed using a lock-in amplifier.

Capacitance measurements have been carried out using the capacitance detection unit described in Sec. 3.1. The compensation of the offset capacitance of the diode is done by stepper motor driven adjustable capacitors. For $C-V$ profiling, a Windows95 based Delphi 4 application was written, which ramps the voltage applied to the diode, reads out the values of the measurement devices, calculates and displays the capacitance, $1/C^2$, doping density and the phase shift between current and voltage. For (O)DLTS measurements, the output of the capacitance detection unit is fed into an Tektronics TEK480A oscilloscope, which records the transients. All devices are computer controlled, therefore the measurement can run automatically, driven by a Turbo Pascal based computer program.

Current measurements, i. e. dark and photoconductivity, have been performed using a Keithley 6(5)17 source measure unit, which was also controlled by appropriate computer programs. For sensitive photoconductivity measurements, the light beam was chopped with 12.8 Hz and the output of the current preamplifier was fed into a lock-in amplifier, which increases the signal to noise ratio.

CHAPTER 5

Diamond

In this chapter the most important material properties of diamond and aspects of growth and doping are briefly summarized.

5.1 Material properties

As can be seen from the phase diagram of carbon in Fig. 5.1, diamond is a metastable form of carbon at room temperature and atmospheric pressure. The stable form is graphite, the sp^2 bonded form of carbon. Due to its π bonds, graphite is electrically conductive, in contrast to intrinsic diamond. Diamond is the sp^3 bonded form of carbon and crystallises in a face centered cubic crystal structure, consisting of two interpenetrating sublattices, whereby one lattice is shifted one quarter along the cube diagonal. Besides the cubic form, a hexagonal form of diamond has been observed [Bun67]. There exists also an amorphous form of carbon, named t-a:C or diamond like carbon (DLC).

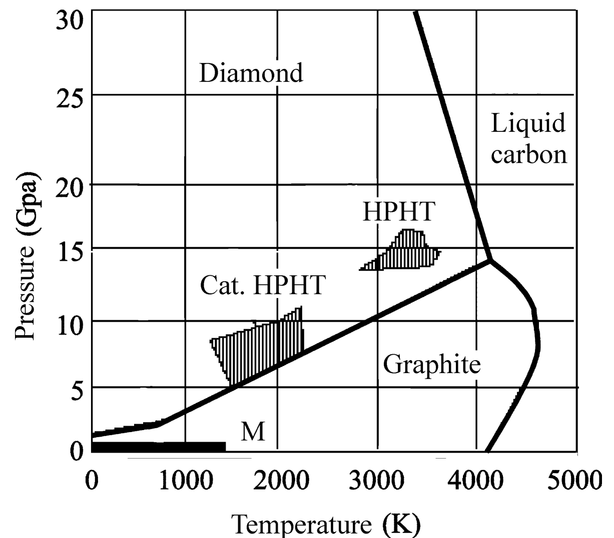

Figure 5.1: Phase diagram of carbon. Cat. HPHT stands for catalytic high pressure/high temperature synthesis, M for metastable CVD growth.

Here, the major fraction is sp^3 bonded carbon, however in a disordered arrangement. t-a:C is characterised by its sp^3 content [Rob86]. The bond length of diamond is 1.54 Å and the lattice constant is 3.56 Å [Lan82]. The mass density is 3.51 g/cm^3 and the atom density is 1.77×10^{23} cm^{-3}. There are two naturally occuring isotopes of carbon, namely ^{12}C and ^{13}C with natural abundances of 98.9% and 1.1%, respectively. The very strong covalent bond is

Property	Diamond	Competing Material
Band gap	5.48 eV	Si : 1.1 eV GaAs : 1.4 eV
Break down field	1×10^7 V/cm	Si : 5×10^5 V/cm GaAs : 6×10^5 V/cm
Hardness (Knoop scale)	9000kg/mm^2	cBN : 4500kg/mm^2 Al_2O_3 : 2000kg/mm^2
Transparency region	$> 10\mu$m - 200nm	MgF : 7.5μm - 140nm Quartz : 4μm - 250nm
Thermal conductivity at 300 K	2000 W/mK	Copper : 400 W/mK
Friction coefficient μ (not lubricated)	0.05 in (111) plane	Teflon : 0.045 Steel : 0.2
Resistivity	$> 10^{16}\Omega$ cm (Type I and IIa)	Quartz : $5 \times 10^{16}\Omega$cm Polyethylene : $10^{10} \ldots 10^{13}\Omega$cm

Table 5.1: Some properties of diamond in comparison with other materials.

partly responsible for the unique properties of diamond. In Table 5.1 some outstanding properties of diamond are summarised and compared with other materials. In addition diamond is chemically inert up to very high temperatures. Only oxidising agents can attack diamond at elevated temperatures (T>1300 K). Graphitization of diamond in an inert atmosphere starts at 1800 K, but in an oxygen atmosphere, the surface starts to turn black at 900 K.

Like all group IV semiconductors, diamond has an indirect band gap of $E_G = 5.48$ eV at room temperature [Cla64]. The direct bandgap is 7.3 eV. Due to the small ordinal number the spin orbit splitting of the valence bands at the Γ point is only 2 meV [Kim97]. The conduction band minima are located at 0.76 along the Δ direction. Measured values of the effective masses of holes (in boron doped diamond) and electrons are summarized in Table 5.2. The mobility of holes ranges from 1600 cm^2/Vs in single crystal diamonds down to 10 cm^2/Vs in polycrystalline CVD diamond. For phosphorus doped n-type diamond mobilities of 200 cm^2/Vs in homoepitaxial diamonds have been reported [Koi97].

5.2 Growth

In the early years of diamond research, only natural stones were available, but in 1953 the first high pressure/ high temperature (HPHT) synthesis succeeded at General Electric (USA) [Bun55]. Since diamond is metastable at normal conditions, the HPHT synthesis has to take place under extreme conditions (15 GPa/3000K). Catalytic synthesis using nickel and iron catalysts allow to reduce the pressure to 7 GPa and the temperature to 2000 K (cf. Fig. 5.1).

However, the size of the crystals grown by the HPHT method is in the millimeter range and therefore not suitable for electronic material. A breakthrough towards large area deposition was achieved by the successful application of chemical vapour deposition (CVD) to diamond growth in the late 70ies [Der75, Kam83] (region M in Fig. 5.1). Today diamond wavers of up to 4 inch diameter and 300 μm thickness can be grown heteroepitaxially on Si substrates, but also Iridium and Platinum substrates are used for better lattice matching [Sch99, Tac00]. Growth is performed in a plasma enhanced CVD process with typical substrate temperatures of 600 °C to 900 °C . Methane is used most commonly as source gas, which is diluted in hydrogen (1 % CH_4 in 99 % hydrogen or even less [Yam00]). This high hydrogen amount is needed to preferentially etch the non diamond carbon phases that grow more likely due to the metastable conditions for diamond during growth.

5.3 Impurities and classification

In natural diamond the most common impurities are nitrogen and boron which significantly influence most of the electrical, optical and thermal properties. Therefore the natural as well as the synthetic diamonds have been classified by four types [Rob34]. Their typical properties are listed in Table 5.3. The type I diamonds differ in the form of incorporated nitrogen. In type Ib diamond, single nitrogen is incorporated on the substitutional site, whereas in type Ia diamond, nitrogen is aggregated in A (type IaA, two substitutional nitrogen atoms as nearest neighbours) and B (type IaB, four nitrogen atoms) aggregates. These forms of nitrogen cause the characteristic infrared spectra shown in Table 5.3. In type IIa diamond, IR absorption due to nitrogen cannot be detected anymore, the only remaining infrared feature is the two phonon absorption around 2000 wavenumbers. In type IIb diamond there is additional absorption due to the excited electronic states of the boron acceptor.

Incorporation of isolated substitutional nitrogen leads to an activation energy of the dark conductivity of 1.7 eV, which is generally believed to be n-type. In 1997 Koizumi and coworkers were the first who succeeded in reproducible n-type doping of CVD diamond by addition of phosphorus [Koi97]. In addition to phosphorus, lithium and sodium have been

Holes		Electrons	
Value	Method [Ref.]	Value	Method [Ref.]
0.3 m_0 and 0.7 m_0	Cyclotron resonance [Kon93]	0.2 m_0	Estimation from exciton binding energy [Cla64]
0.88 m_0	Faraday rotation [Pro64]		
0.25 m_0 - 1.1 m_0	Hall effect [Mit63, Dea65]		

Table 5.2: Effective masses for holes and electrons as obtained by different experiments.

	Type Ia	Type Ib	Type IIa	Type IIb
Impurities	nitrogen, 500 … 2000 ppm in aggregated forms, either A- or B-aggregates (Subtypes IaA and IaB, defined by IR spectra).	Substitutional, isolated nitrogen, 50 … 500 ppm	nitrogen, less than 50 ppm	nitrogen and boron, less nitrogen than boron
ρ	insulating	insulating	insulating	$10 < \rho < 10^4 \Omega$cm
Comments	Most natural diamonds are of this type. Transparent.	Most synthetic diamonds are of this type. Can be converted to Ia by high temperature annealing [Kif94]. Yellow and greenish colour.	Very rare in nature, transparent. Type of gemstones.	Extremely rare, semi-conducting, transparent or blueish due to absorption of the boron acceptor
IR absorbance	IaB IaA 1000 1500	1000 1500	1000 3000	boron 1000 3000
	wavenumbers			

Table 5.3: Assignment of diamonds to four types according to their impurities and infrared spectra. The infrared spectra for type IaA, IaB and Ib are taken from [Dav76, Woo86, Kif94], respectively. The spectra of the type II diamonds are shown on an extended scale. The shaded area corresponds to the spectral range used for the classification of type I diamonds.

predicted to act as donors on an interstitial site [Kaj91] and sulfur as a substitutional shallow donor [Saa00].

CHAPTER 6

Boron in Diamond

As already indicated in Table 5.3, boron acts as an acceptor in diamond with an ionisation energy of 374 meV. The resistivity is generally lower than $10^4\,\Omega$cm. By adding diborane to the source gas in CVD growth, the boron concentration in diamond can be controlled in the range of $10^{15}\ldots10^{20}$ cm^{-3}. This doping effect was attributed to aluminum up to 1971 [Bro55, Col71]. Other p-type dopants are not known up to know.

Optically, the boron acceptor – if present in sufficient amount – manifests itself in a blueish colour of the diamond. This is due to the fact that the otherwise transparent diamond absorbs light in the region 0.38 eV up to 2 eV due to photoionisation of the holes bound to the boron acceptor. This can be very well seen in photoconductivity experiments. An example is shown in Fig. 6.1 [Roh98]. In the infrared region below a photon energy of 370 meV, the excited states of the boron acceptor can be seen by e. g. infrared absorption. A typical spectrum is shown in Fig. 6.2. The absorption lines at 304 meV, 341 meV, 347 meV and 349 meV arise from transitions from the $1s$ ground state into the different $2p$ levels. The line at 364 meV is due to excitation to even higher states. The hump around 320 meV is due to two phonon absorption, since it is present in type IIa diamonds, too.

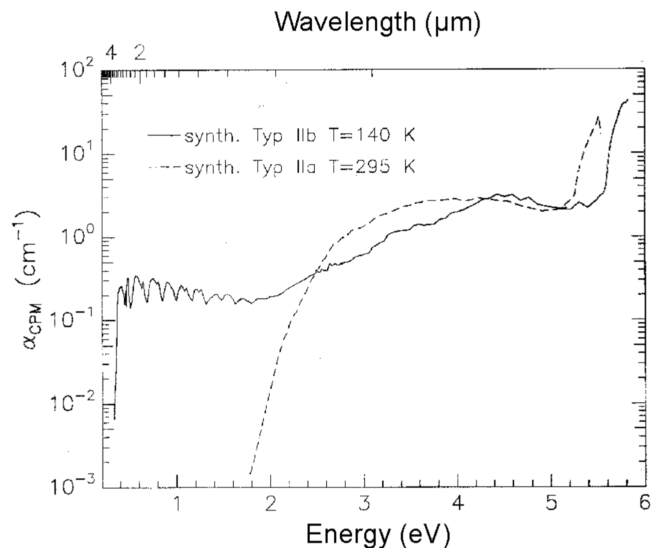

Figure 6.1: Photoconductivity of a type IIb an type IIa diamond [Roh98].

Electronically, the presence of boron acceptors can be probed by Hall effect measurements. A typical temperature dependent hole concentration of natural type IIb diamond is

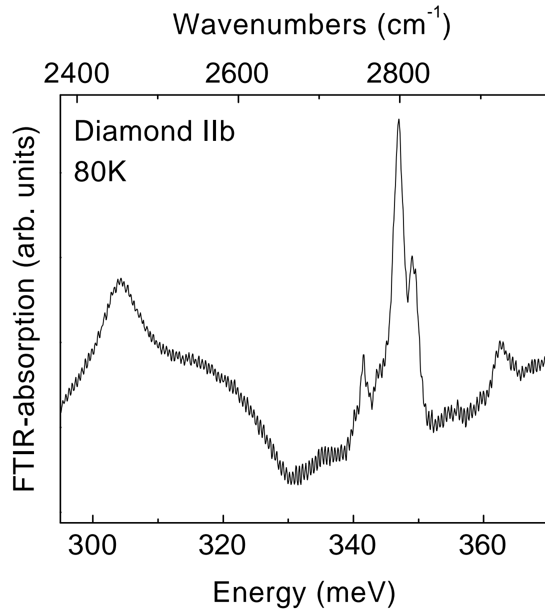

Figure 6.2: Fourier transform infrared absorption of a type IIb diamond. The discrete lines are due to electronic transitions of holes from the ground state to excited states at the boron acceptor.

shown in Fig. 6.3. From the Arrhenius plot of the hole concentration an activation energy of 377 meV results. This indicates a rather high compensation ratio. At temperatures above 600 K, the onset of carrier exhaustion can be seen. An extrapolation gives an uncompensated acceptor density of around 2×10^{16} cm^{-3}. The temperature dependence of the Hall mobility is $\mu_H \propto T^{-\beta}$, where β is larger than the 1.5, as expected from phonon scattering, approxi-

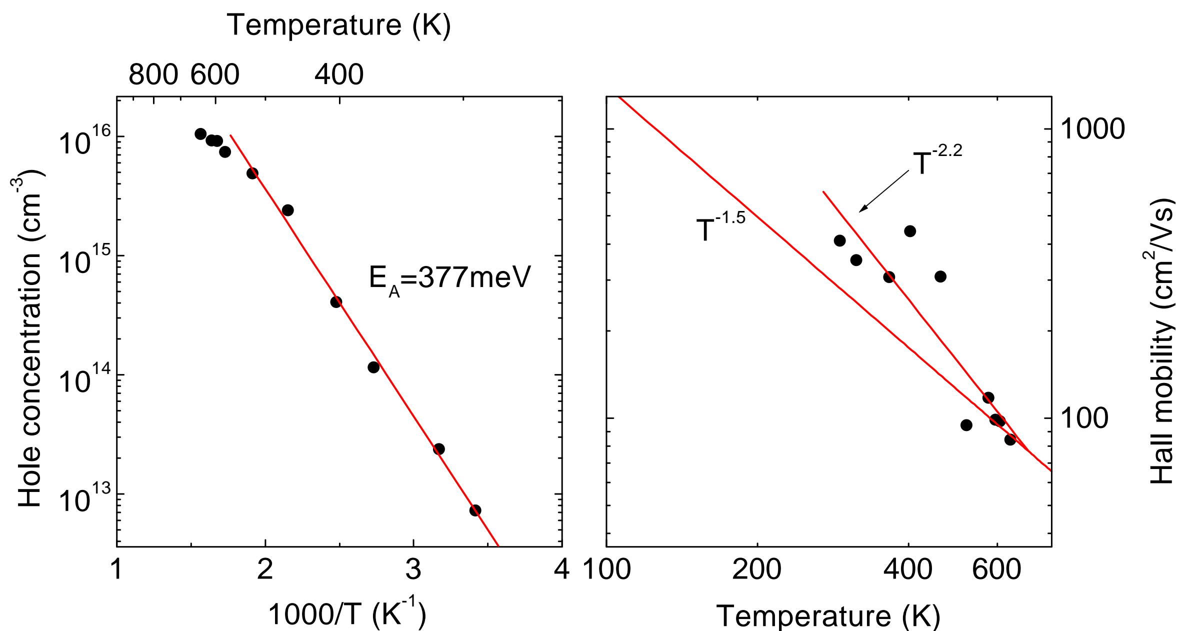

Figure 6.3: Left : Temperature dependent hole concentration of a type IIb boron doped natural diamond. Right : Temperature dependent hole mobility. The exponent of the temperature dependence of the mobility is larger than 1.5.

mately 2.2. This unusual high exponent is in agreement with the results of Malta *et al.* who found an exponent of -2.24 in Hall experiments on type IIb natural diamond [Mal93].

To determine the actual acceptor density, Hall experiments are unsuitable. For this purpose, the sample has to be brought to temperatures, where the acceptors are fully ionised, which means for the boron acceptor well above 1000 K. These are temperatures, where reliable Hall are difficult to carry out.

If it is possible to make rectifying contacts to the sample, it is much easier to perform $C-V$ measurements. Here the uncompensated acceptor density is probed at room temperature with the help of the electric field in the space charge region. However, to perform capacitance measurements, it is essential to reduce the frequency of the applied test voltage from MHz (standard capacitance meters) to several ten Hz to account for the emission rate of the boron acceptor and the residual resistivity of the layer (see Sec. 3.1). For Ohmic contacts the metal layers titanium/ platinum/ gold with the thicknesses 300 Å/ 150 Å/ 1500 Å have been deposited and annealed at 600 °C for 10 min in a forming gas atmosphere. As reported by Tachibana *et al.*, titanium forms a TiC layer at the contact interface. This produces a highly defective interface layer, whereby the contact becomes ohmic [Tac92]. Platinum has been introduced as a diffusion barrier for the Au top layer. For Schottky contacts, mainly Au and aluminum are used [Glo73, Har94]. However, it turned out that silver contacts also exhibit very good rectifying behaviour. Since Ag can be very easily etched in HNO_3, whereas the Ohmic contacts are unaffected by this acid, Ag has been mostly used as Schottky contacts in this work. Before any contact deposition, a cleaning of the diamond surface by an oxygen plasma was performed. In addition it turned out that it is necessary to clean the sample in chromosulfuric acid (CrO_3:H_2SO_4) at 80 °C for 1 hour before Schottky contact deposition. A $C-V$ measurement on natural type IIb diamond is shown in Fig. 6.4. The $1/C^2$ data follow a straight line, which shows a

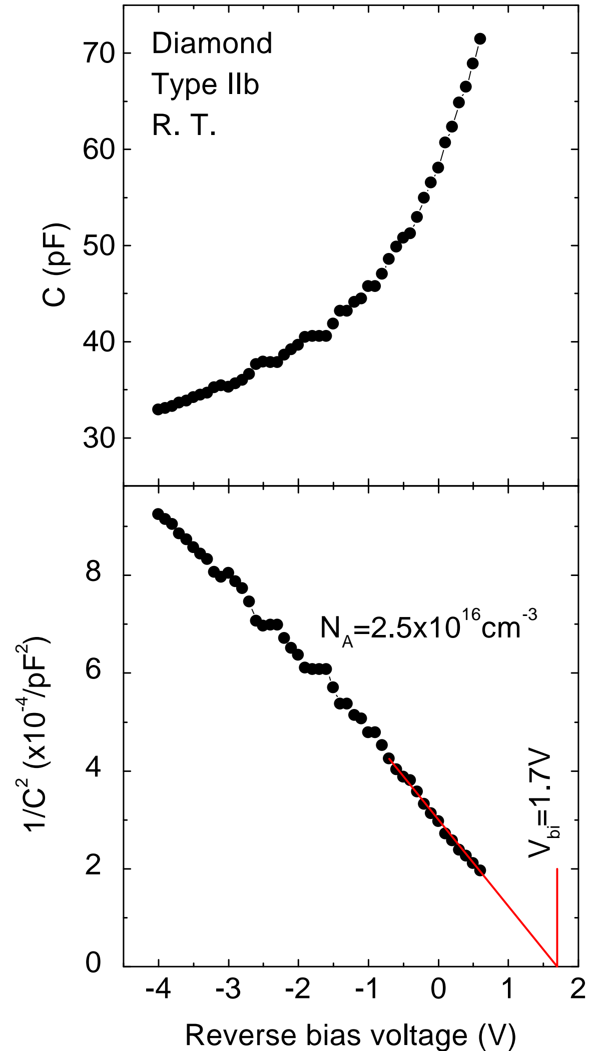

Figure 6.4: $C-V$ and $1/C^2$ plot of Ag Schottky diode on a natural type IIb diamond.

homogeneous acceptor density. The uncompensated acceptor density is calculated from the slope in the $1/C^2$ plot after Eq. (2.46) to 2.5×10^{16} cm^{-3}. This order of magnitude is typical for natural and synthetic HPHT diamonds [Mal93, Ris97, Wyn94, Glo73]. The extrapolation of the $1/C^2$ line to 0 yields the built-in potential V_{bi}, which is 1.7 V in this case. This value is comparable with the 1.4 V obtained for Au [Glo73, Mea76] and 1.7 V for Al [Mea76].

CHAPTER 7

ODLTS Investigations of Boron doped Diamond

The ability to reduce the resistivity of intrinsic diamond by boron doping allows the application of (O)DLTS to this material. In the otherwise extremely highly resistive diamond, only a limited number of experiments can be used to elucidate the electronic properties of defects in natural and synthetic material. It has been shown – mainly by luminescence and absorption techniques – that a variety of defects are present with well defined energy levels in the bandgap of diamond. With the aid of the Schottky diodes as described in Sec. 6, it is possible to perform transient capacitance spectroscopy. To explore the energy range 0.8 eV $\leq h\nu \leq$ 2 eV above the valence band in the band gap of boron doped diamond, ODLTS measurements are superior to spectrally resolved photoconductivity experiments. In this region, the absorption is strongly dominated by the photoionisation of the boron acceptor even at boron concentrations as low as $\approx 10^{16}$ cm^{-3} [Roh98, Col69]. Therefore photoconductivity experiments are unable to characterise defects in this energy range. In DLTS measurements, the defects are probed within the depletion layer of a diode. Since the boron acceptors are ionised already in this region, they cannot mask the optical absorption of other defects.

7.1 CVD diamond

The CVD diamond investigated here has been grown homoepitaxially in a microwave plasma quartz reactor at 820 °C and 30 Torr gas pressure. The gas composition was 100 sccm hydrogen and 4 sccm methane. Diborane was added resulting in a boron to carbon concentration ratio of 10 ppm in the gas phase. A synthetic type Ib substrate was used, upon which an undoped buffer layer of 1 micron was deposited, before the 3.5 micron thick boron doped layer was grown. The sample preparation was carried out as described in Chapter 6. Due to the isolating substrate, a coplanar contact configuration has been used, where the spacing

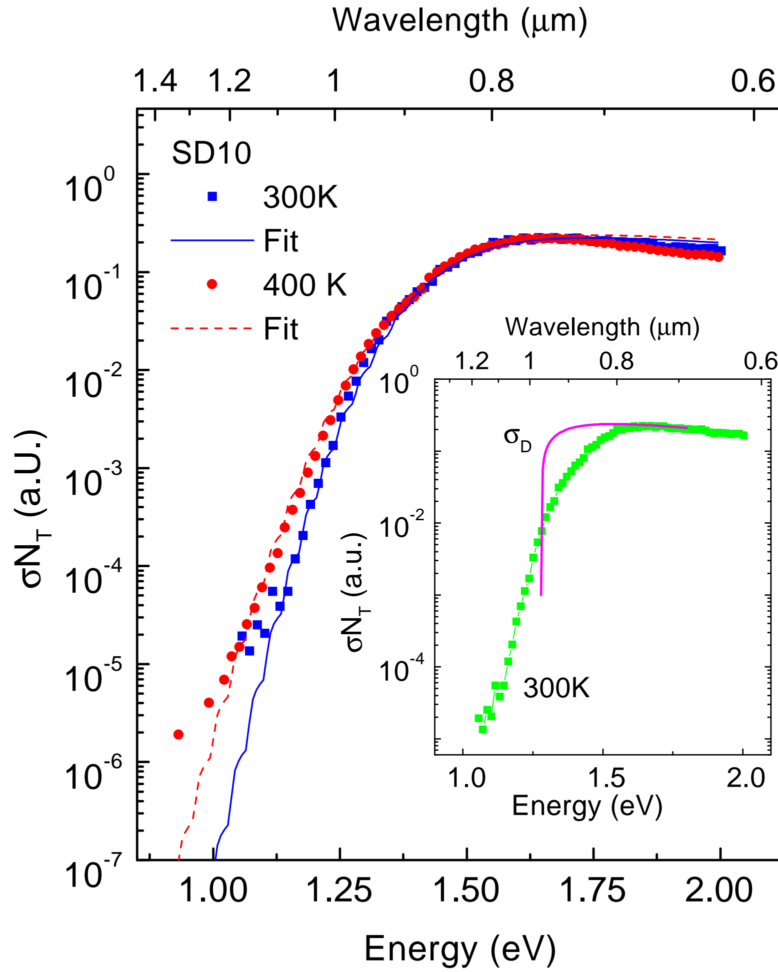

Figure 7.1: ODLTS spectra of a boron doped CVD-diamond at 300 K (squares) and 400 K (circles). Also included are two fits for the absorption at the two temperatures after Eq. (7.6). The inset shows the spectrum at 300 K with a photoionisation cross section after Inkson

between the Ohmic and the Schottky contact was 50 microns. The Schottky contact was illuminated through the substrate. This limits the spectral range to $h\nu \leq 2$ eV, since the Ib diamond is strongly absorbing for $h\nu > 2.1$ eV. For photon energies $h\nu < 2$ eV, the spectral dependence of the absorption coefficient varies from 0.8 cm^{-1} at 1.4 eV to 2 cm^{-2} at 2 eV. For capacitance measurements a test frequency of 84 Hz was used.

The ODLTS spectrum at 300 K – obtained from the initial rise of the capacitance transients – is shown in Fig. 7.1 (squares). A threshold at 1.0 eV is detected. The absorption steeply increases over 4 orders of magnitude and shows a maximum at 1.65 eV. For $h\nu \geq 1.65$ eV the absorption decreases slightly. To determine the trap levels from optical absorption one commonly calculates fits of theoretical photoionisation cross sections (see 2.3.2) to the

experimental data :

$$\sigma_o \sim \frac{\varrho(h\nu - E_T)}{h\nu} \frac{(h\nu - E_T)^\delta}{(h\nu)^{2\gamma}} \tag{7.1}$$

where E_T is the trap level and $\varrho(E)$ the density of states in the valence band, $m_T = m^*$ has been used. δ can be 0 or 1 which defines an allowed or a forbidden transition, respectively and γ, either 0 or 1, stands for an indirect or a direct transition, respectively. However, none of the four theoretical cross sections can be fitted satisfactorily to the experimental data. For example the best calculated fit of a cross section with trap energy at 1.28 eV, $\varrho(E) \sim E^{1/2}$, $\delta = 1$ and $\gamma = 1$ is shown in the inset of Fig. 7.1. Although a good agreement between the optical cross section and the experimental data for $h\nu \geq 1.6$ eV is achieved, the deviation below 1.6 eV is obvious, indicating a significant level broadening of the absorption centers.

Broadening can have various causes [Böe90]. It can be due to bonding disorder, introduced by structural imperfection such as dislocations in the layer. More important however, is thermally induced broadening, which becomes evident by comparing the spectra measured at different temperatures as shown in Fig. 7.1. The two spectra, recorded at 300 K and 400 K, are normalized to $\sigma_o N_T(1.6\text{ eV})$. For photon energies $h\nu < 1.25$ eV a strong temperature dependence of the absorption can be recognized. Spectra taken at higher temperatures were strongly affected by thermal emission competing with the optical excitation. Measurements below room temperature were not possible due to the exponentially increasing series resistance of the sample.

To calculate the energy level of the defect detected by ODLTS, the lattice relaxation model is assumed, which manifests itself in a Stokes shift of the transition energy for optical ionisation relative to the energy necessary for thermal ionisation. This is schematically shown in Fig. 7.2. Here, the lattice energy plus the electronic energy of the initial (lower parabola) and the final (upper parabola) state is plotted versus a configuration coordinate. After photoionisation, the hole is delocalized in the valence band. Therefore, the final state is defined by the vibronic states of the defect and the density of states of the valence band. Accounting for this, the resulting optical cross section σ_o^L has to be recalculated, since the expression for σ_o from Eq. (7.1) does not include any electron-phonon interaction. Here we follow the approach of Jaros [Jar77]

$$\sigma_o^L(h\nu) = \frac{1}{h\nu} \int \left| \langle \psi_b | - i\hbar\vec{\nabla} | \psi_T \rangle \right|^2 L(\epsilon, h\nu) \varrho(\epsilon) d\epsilon, \tag{7.2}$$

where ψ_b and ψ_T are the wave functions of holes in the valence band and in the trap, respectively. As Hamilton operator, the standard dipole approximation of the electromagnetic field is used. $L(\epsilon, h\nu)$ is the line shape function which takes into account the different transition probabilities between the vibrational states α and β of the defect and has been treated

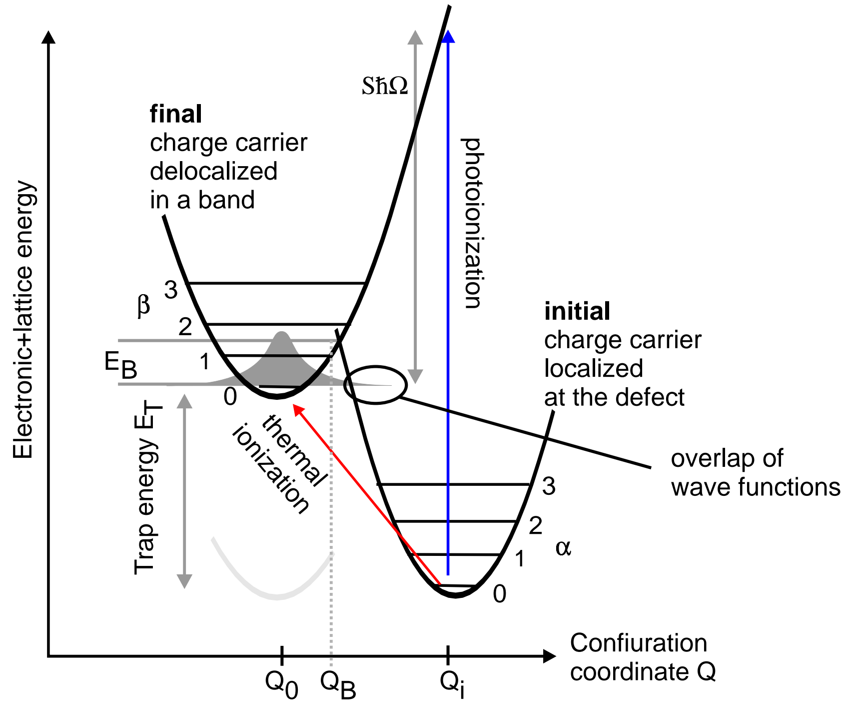

Figure 7.2: The configuration coordinate diagram for deep levels. The two parabola – initial and final defect state – with the vibrational levels are shifted horizontally by the change in configuration coordinate Q and vertically by the trap energy E_T. An optical transition between different vibronic states of initial and final defect state is marked with an arrow.

in detail by Keil [Kei65]. When the lattice coupling is treated quantum-mechanically, L consists of a sum over weighted delta functions, which represent the contribution of each vibrational state of the defect to the photoionisation. Most authors replace this sum of delta functions by a Gaussian function. This is valid in the so called high temperature/strong coupling limit [Lax53], which is defined by a large Huang-Rhys factor S and high temperatures, i. e. phonon energy $\hbar\Omega \ll kT$. But these conditions are not fulfilled in many cases, since – especially in diamond – the phonon energies are equal to or even larger than kT in the temperature range considered here. Therefore we use the fully quantum mechanical expression for the line shape function

$$L(E,h\nu) = \sum_{p=-\infty}^{\infty} \delta(p\hbar\Omega + E_T + E - h\nu) W(p) \tag{7.3}$$

where $W(p)$ is the weighting function defined by [Kei65]

$$W(p) = \exp\left[p\hbar\Omega/2kT - S\coth(\hbar\Omega/2kT)\right] I_p\left(S\,\mathrm{cosech}(\hbar\Omega/2kT)\right). \tag{7.4}$$

In these equations I_p is the Bessel function of the first kind with imaginary argument, $\hbar\Omega$ the energy of the involved phonon and $h\nu$ the energy of the incident photons. p is defined by

$p = \alpha - \beta$ where α and β are the quantum numbers of the phononic excitation of the ground state and the ionised state of the defect, respectively.

The integral Eq. (7.2) now decays in a sum over weighted matrix elements

$$\sigma_o^L(h\nu) = \frac{1}{h\nu} \sum_{p=-\infty}^{\infty} W(p)\, |\langle\psi_b| - i\hbar\nabla|\psi_T\rangle|^2\, \varrho(h\nu - E_T - p\hbar\Omega). \tag{7.5}$$

For the calculation of the matrix elements we again rely on the model of Inkson[Ink81]. Thus we get, using $\varrho(E) \sim E^{1/2}$

$$\sigma_o^L(h\nu) \sim \frac{1}{h\nu} \sum_p W(p) \frac{(h\nu - E_T - p\hbar\Omega)^{\gamma+1/2}}{(h\nu - p\hbar\Omega)^{2\delta}}, \tag{7.6}$$

where γ and δ have the same meaning as in Eq. (7.1).

Eq. (7.6) contains five free parameters of interest, namely the trap energy E_T, the two parameters for the photoionisation cross section γ and δ, the Huang-Rhys factor S – present in $W(p)$ – and the phonon energy $\hbar\Omega$. To account for the well pronounced plateau for $h\nu > 1.65$ eV, $\gamma = 1, \delta = 1$ has been assumed. Nothing is known about the phonon energy $\hbar\Omega$ of the defect. In our calculations, we assumed values in the range 30 meV to 60 meV which is reasonable in view of the fact that in absorption and luminescence experiments on diamond these values are often detected [Fie92]. Finally S and E_T have been used as fit parameters. The best fits are shown in Fig. 7.1, the corresponding fit-parameters are summarized in the following table.

Parameter		Value
	γ	0
	δ	1
Phonon energy	$\hbar\Omega$	35 meV
Huang-Rhys Factor	S	4.5
Franck-Condon shift	$S\hbar\Omega$	0.16 eV
Trap energy	E_T	1.28 eV

It is worth noting that the Huang-Rhys factor S is not independent of the phonon energy $\hbar\Omega$. Varying the latter in the range 15 meV to 50 meV, the best fits were obtained with values of S that were given through $S = 0.16\mathrm{e}V/\hbar\Omega$, with a constant Franck-Condon shift $S\hbar\Omega$ of 0.16 eV. For the optical ionisation energy we calculate 1.44 eV, using the relation $E_{\mathrm{opt}} = S\hbar\Omega + E_T$.

The shoulders in the calculated spectra result from the summation over the individual photoionisation cross sections located at $p\hbar\Omega$ around E_T. The lack of this feature in the

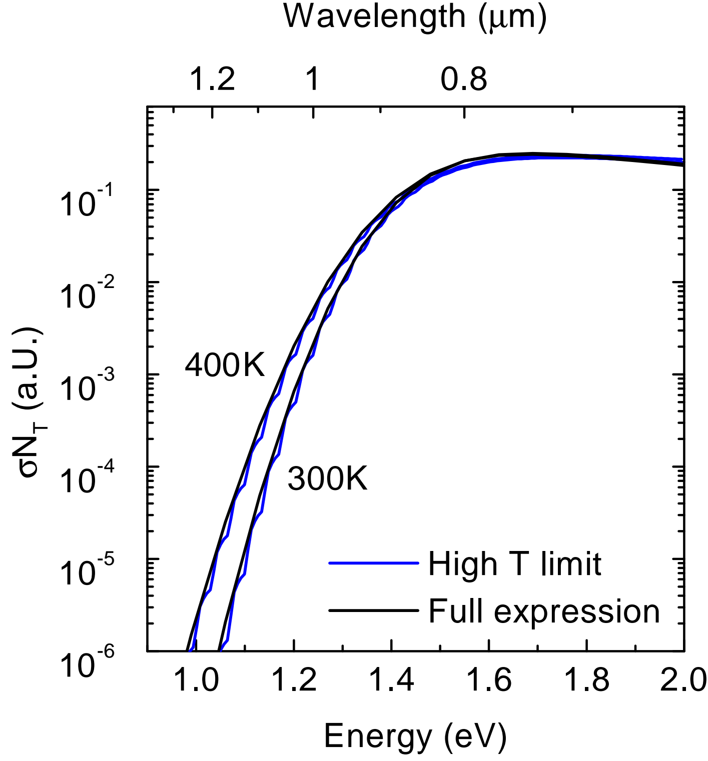

Figure 7.3: Comparison of the photoionisation cross sections after the high temperature strong coupling limit Eq. (7.7) and the exact treatment of the line shape function Eq. (7.6).

experimental data allows two conclusions. First, we can assume that the phonon energy of the defect is smaller than about 10 meV. Such closely spaced shoulders cannot be resolved within this experiment. However, such a small phonon energy would give rise to a large Huang-Rhys factor $(S \geq 16)$ and therefore to strong electron-phonon coupling.

On the other hand the defect may couple to a broad range of phonon energies and therefore no discrete structure would be resolved in the measured spectra. Since it is – within this experiment – not possible to extract information about the involved phonon energy, the value above should be regarded as an effective frequency. However, the main information about the configurational properties is given through the Frank-Condon parameter of 0.16 eV which is independent of the phonon energy.

From the Franck-Condon shift and the phonon energy a Huang-Rhys factor of 4.5 is calculated. This is a value just between strong and weak coupling. Also the phonon energy is comparable with the thermal energy. A comparison of the fitting results obtained with the exact treatment of the weighting function – as presented above – and the high temperature/ strong coupling limit is shown in Fig. 7.3. The photoionisation cross section in this limit is given by [Cha81]

$$\sigma_o(h\nu) \propto \frac{1}{h\nu} \int_{E_T+S\hbar\Omega}^{\infty} \frac{(h\nu' - h\nu)^{1/2+\gamma}}{(h\nu' - S\hbar\Omega)^{2\delta}} \exp\left(-\frac{(h\nu' - h\nu)^2}{4kTS\hbar\Omega}\right) dh\nu'. \tag{7.7}$$

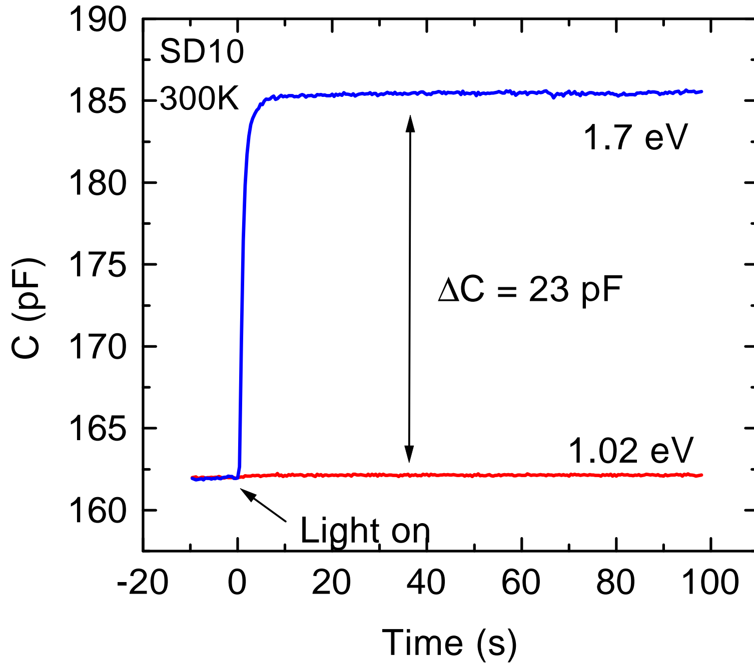

Figure 7.4: Two transients capacitances for photon energies $h\nu = 1.02$ eV and 1.7 eV. The change in illuminated steady state capacitance between the two photon energies is related to the defect density.

Apart from the shoulders that occur in the exact treatment, the theoretical photoionisation cross section of the two models coincide very well.

To determine the trap density N_T, the quantity $\Delta C = C_{SS}(h\nu_2) - C_{SS}(h\nu_1)$ – the change of the steady state capacitance under illumination between two photon energies – is needed. This is shown in Fig. 7.4. $h\nu_1$ has to be lower than the optical ionisation energy (here $h\nu_1 = 1.02$ eV) and $h\nu_2$ has to be above the optical ionisation energy (here $h\nu_2 = 1.7$ eV). The commonly used approximation for the defect density, Eq. (3.14), would lead to a defect density of the order of magnitude of the acceptor density. Therefore one has to use Eq. (3.17), which yields $N_T = 1.2 \times 10^{16}$ cm^{-3} for the 1.28 eV level.

The Stokes shift, i. e. the fact that the optical absorption maximum E_o is above the thermal ionisation energy (E_T), is due to the different configuration coordinates of the energy minima of the final and initial states (Q_0 and Q_i in Fig. 7.2). As sketched in Fig. 7.2 the intersection of the two parabola is between Q_0 and Q_i. As a consequence, the hole, once excited into the band minimum cannot be recaptured, since there is only a small overlap between the ground state of the band ($\beta = 0$) and any excited state of the lower parabola. Only if the hole acquires enough energy to overcome the energy barrier E_B, it can be recaptured by the defect. An energy barrier therefore leads to a significant lowering of the capture cross section of a defect. However, when Q_i is decreased towards Q_0 (smaller lattice relaxation), the intersection will shift to the the left of Q_0. At the same time the Franck-Condon shift is lowered, approaching zero, when $Q_0 = Q_i$. In the present case, the small Franck-Condon shift of 160 meV relative to the trap energy of 1.28 eV indicates a small lattice relaxation,

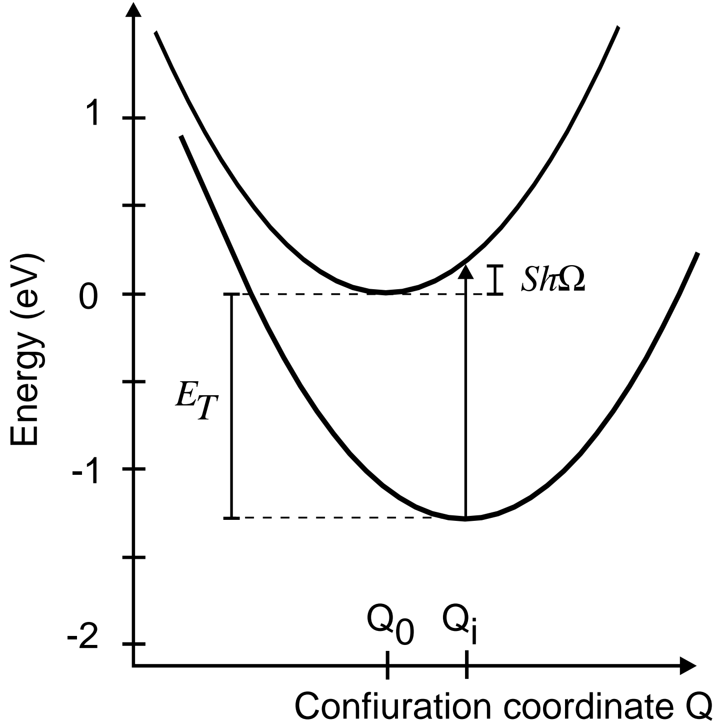

Figure 7.5: Configuration coordinate diagram for the 1.28 eV defect in CVD diamond. The small Franck-Condon shift indicates a small lattice relaxation.

the two parabola are only slightly shifted horizontally. This situation is illustrated in Fig. 7.5. To estimate the presence of a barrier, the parabolic energy curves of the initial and final states in Fig. 7.2 are described by

$$E_i = -E_T + \frac{1}{2}k_i(Q_i - Q)^2 \tag{7.8}$$

$$E_f = \frac{1}{2}k_f(Q_0 - Q)^2 \tag{7.9}$$

where k_i and k_f are the the curvatures of the initial and final parabolas, respectively. From Fig. 7.2 it is obvious, that

$$S\hbar\Omega = \frac{1}{2}k_f(Q_0 - Q_i)^2. \tag{7.10}$$

Equating Eqs. (7.8) and (7.9) and assuming $k_i = k_f$ [1] results in a crossover coordinate

$$Q_B = \frac{(S\hbar\Omega - E_T)}{\sqrt{2kS\hbar\Omega}}. \tag{7.11}$$

If Q_B has a negative sign, the two parabolas in Fig. 7.2 cross each other at negative Q-values. This means in particular, that there is no barrier for capturing holes from the valence band as

[1] This assumption $\omega_i = \omega_f$ is consistent within the model, since it has already been made for calculating the line shape function [Kei65].

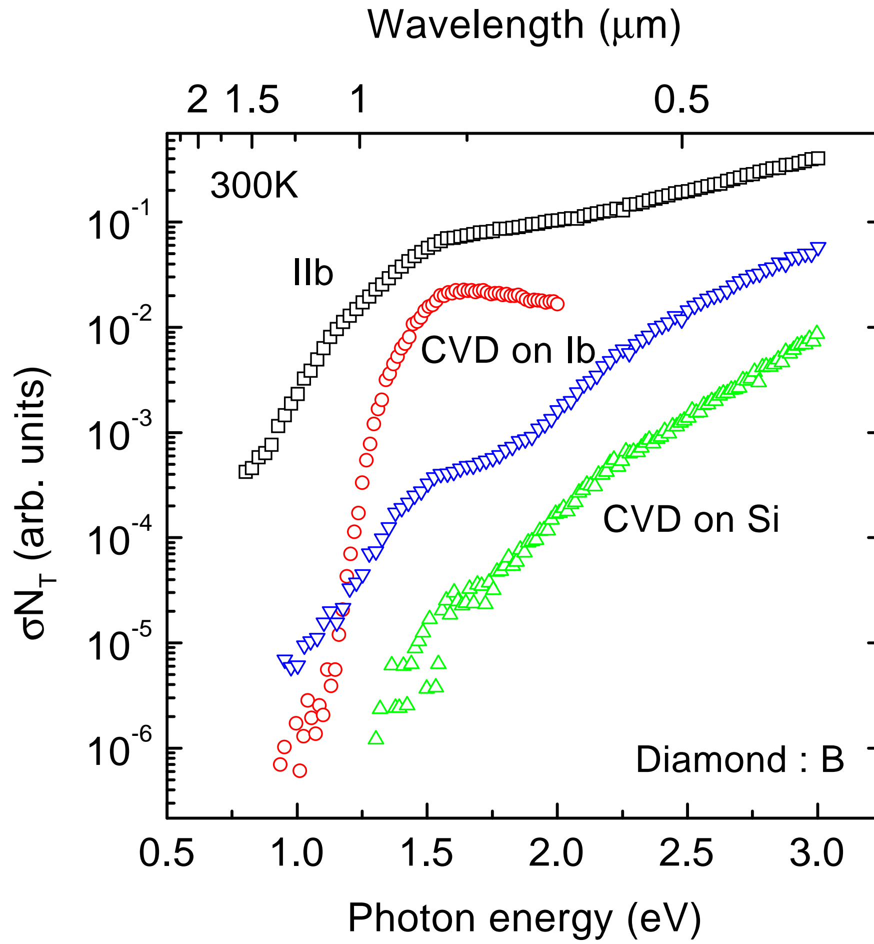

Figure 7.6: ODLTS spectra of various boron doped diamonds. The CVD samples are grown homoepitaxially on type Ib substrates (CVD on Ib) and heteroepitaxially on a Si substrate (CVD on Si). Additionally a synthetic type IIb sample is shown.

it would be the case for $Q_B > 0$. The sign of Q_B is determined only by the sign of the term $S\hbar\Omega - E_T$. In our case $S\hbar\Omega$ is smaller than E_T and therefore we expect no capture barrier for the defect detected by ODLTS.

Investigating other boron doped diamonds using the ODLTS technique reveals spectra as shown in Fig. 7.6. Besides the already presented homoepitaxial CVD sample, spectra of another homoepitaxially grown CVD diamond and a heteroepitaxially grown sample are shown. The uppermost spectrum represents a synthetic type IIb diamond where the boron concentration is 2×10^{16} cm^{-3}. The other samples are CVD grown boron doped samples. Their boron concentration is in the range of 5×10^{17} cm^{-3}. It is remarkable that in the spectral region 1.3 eV $\leq h\nu \leq$ 1.8 eV all of these diamonds, which originate from very different sources, show an absorption shoulder, no matter on which substrate they are grown. This indicates that in all samples the defect studied above with a thermal ionisation energy

of 1.28 eV is present. The different spectral shapes of the absorption for photon energies $h\nu < 1.3$ eV are due to the superposition of an additional trap at about 0.9 eV [Zei98]. Even in natural type IIb diamond a defect absorption could be detected at a corresponding energy by Ristein *et al.* [Ris97]. The ubiquity of this defect in boron doped diamond suggests the relation to a common impurity like nitrogen, an intrinsic defect like a vacancy or a carbon interstitial or even to a boron induced defect level. Artificial creation of such intrinsic defects via radiation damage can provide more insight into the microscopic nature of this defect. If the defect density is increased after radiation damage, an intrinsic nature would be very likely, if not, it is more probable that an impurity is responsible for this defect.

7.2 Ion implantation and annealing of type IIb diamond

Before presenting the results of ODLTS on carbon ion implanted IIb diamonds, a brief overview over existing work on radiation damage and the associated defects is given. Radiation damage in diamond has been the subject of a series of studies over a couple of decades. This has led to the identification of many defects induced by radiation damage, mainly done by high energy electron irradiation. The most prominent consequence of radiation damage is the GR1 absorption with a zero phonon line at 1.673 eV, present in luminescence and absorption spectra, which has been shown [Cla73] to be caused by the neutral vacancy V^0. However there are other lines associated with the neutral vacancy, named GR2-8, which are – in contrast to the GR1 line – photoconductive [Ver81]. These neutral vacancy caused absorption features are observed in both type IIa and type I crystals. In the latter ones one finds in addition to the neutral vacancy the negatively charged vacancy V^-, which causes the so called ND1 absorption with a zero phonon line at 3.149 eV [Dav77].

In contrast to the negative and neutral vacancy, the positive vacancy has received only little attention. In a comprehensive study, Mainwood and Stoneham[Mai97] make some predictions about the stability of charge states of the vacancy. Within this model the stable state of the vacancy should be negative, when the Fermi level is more than 3.2 eV above the valence band (e. g. type I diamond), neutral, when it lies between 1 eV and 3.2 eV (type IIa diamond) and positive when the Fermi level is not more than 1 eV above the valence banFd. This implies, that in type IIb diamond one would expect positive vacancies. Only recently Steeds *et al.* [Ste00b] observed a photoluminescence line in TEM irradiated boron doped CVD diamond at 636 nm (1.95 eV), which they tentatively attributed to the positive vacancy. There are only a few photoconductivity studies of electron irradiated type IIb diamonds [Ver81, Cla79, Hal82] and only Vermeulen *et al.* [Ver81] measured the spectrally resolved photoconductivity in the region 1 eV $\leq h\nu \leq$ 3 eV. However, their sample was so heavily irradiated that it became coloured and again the GR1-8 absorption centers were the dominant features in their spectra.

It is known from implantation dose dependent conductivity measurements that the boron acceptor is compensated by vacancies [Kal97]. Therefore we expect the Fermi level to shift towards midgap, once the vacancy concentration equals that of boron. To observe the positive charge state of the vacancy, the Fermi level has to be kept near the valence band edge and therefore the vacancies created by radiation damage must not exceed the boron concentration.

7.2.1 Experimental

A single crystal natural type IIb diamond was used which was characterised by $C-V$ and ODLTS experiments before implantation. For the measurements Ti/Pt/Au for Ohmic contacts was evaporated and Ag for Schottky contacts, which where 200×200 μm^2 in size. For capacitance measurements a test frequency of 6 kHz at room temperature and 680 Hz at 210 K was used. After removal of the Schottky contacts, three areas of the sample were implanted at R.T. with 160 keV C^+ ions with doses of 1×10^{10} cm^{-2} (dose I), 1×10^{11} cm^{-2} (dose II) and 1.1×10^{11} cm^{-2} (dose III). One area was not implanted. Due to their small penetration depth, carbon ions have been chosen to create the radiation damage, instead of the commonly used high energy electrons. In this way, the defect rich and therefore highly resistive layer is created within a few hundred nanometers below the surface and is therefore a part of the depletion layer of a Schottky diode. As a consequence, the series resistance of the diodes is not affected by implantation. After implantation, Ag Schottky contacts were re-evaporated. The ODLTS measurements have been performed at 2 V reverse bias after applying a filling pulse of 1.5 V forward bias for 2 sec.

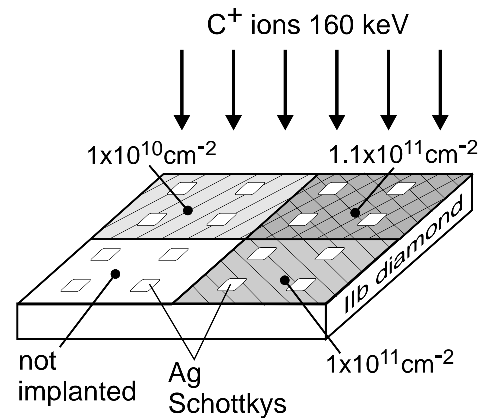

Figure 7.7: Contact and implantation geometry.

The isochronal annealing experiments have been carried out in a thermal annealing furnace under high vacuum. The samples were heated to the annealing temperature within less than 4 min, kept there for 1 h and cooled down to room temperature within 5 min. After each annealing step, $C-V$ and ODLTS measurements were carried out at 210 K.

7.2.2 Measurements

In this section the results of the $C-V$ and ODLTS measurements after implantation and annealing will be presented.

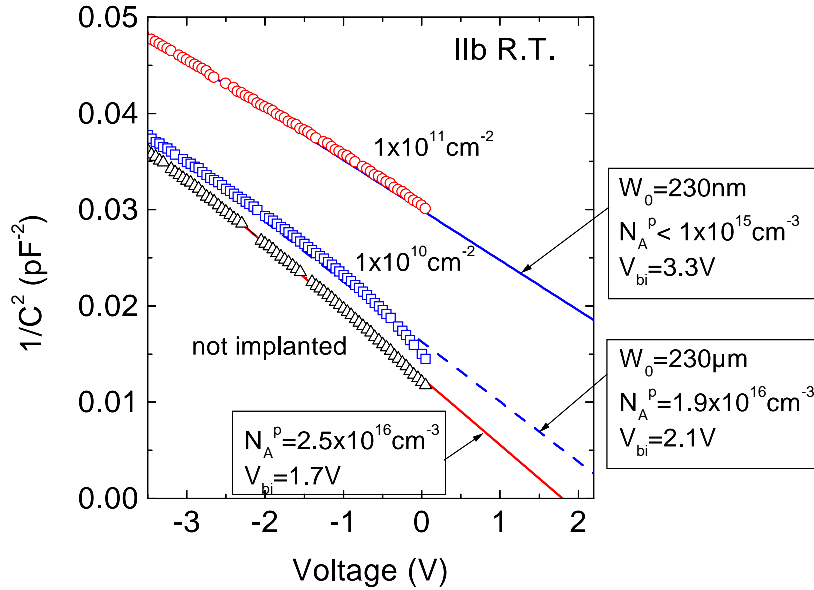

Figure 7.8: $1/C^2$ data of the type IIb diamond before and after carbon ion implantation with two different doses. The higher the dose, the more the $C-V$ characteristic deviates from an ideal behaviour. The line graphs represent the best fit to the data after a model accounting for the compensation of the acceptors in the radiation damaged volume.

Implantation

The $1/C^2$ data of the unimplanted sample is shown in Fig. 7.8 (triangles). It reveals an uncompensated acceptor density of 2.5×10^{16} cm^{-3} and a built-in voltage of 1.7 V. Also shown are the $1/C^2$ data of the samples implanted with two different doses. There is no change for the area that was not implanted, so one can exclude any influence of the processing. A slight increase (i. e. a slight decrease in capacitance) is observed for the diode implanted with 1×10^{10} cm^{-2}. In this region, the sample is still p-type with a slightly higher compensation ratio than without implantation.

The implantation doses 1×10^{11} cm^{-2} and 1.1×10^{11} cm^{-2}, however, induce a significant deviation of the $C-V$ profile compared to the unimplanted diode. Within the penetration depth W_0 of the carbon ions, they have created defects which fully compensate the boron acceptors, resulting in a highly resistive layer underneath the surface. The depth profile of the vacancy density created by ion implantation was calculated using TRIM-simulation [Zie85], which is shown in Fig. 7.9. Effects of immediate recombination of the vacancies with interstitials are not taken into account. Therefore the actual vacancy density is expected to be lower than calculated. From the TRIM plot, the compensation depth W_0 of 230 nm can be determined by the point, at which the vacancy density drops to zero. As shown in Appendix A the capacitance for a diode with a compensated layer of width W_0 underneath

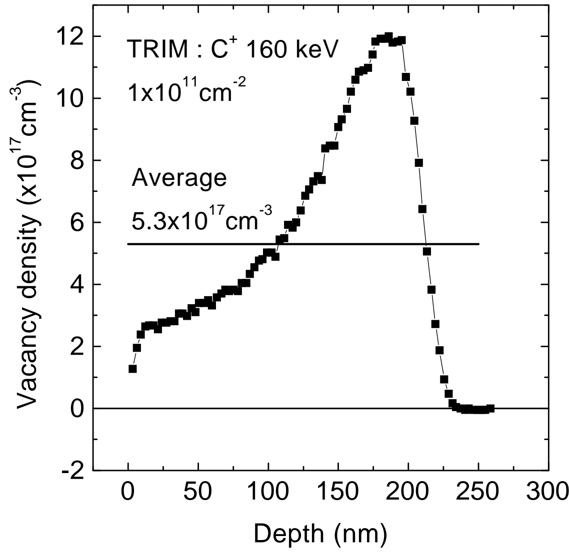

Figure 7.9: TRIM computer simulation of the vacancies created by 160 keV C^+ ions implanted in diamond with a dose of 1×10^{11} ions/cm^2. The density refers to the primary created one. Effects of immediate recombination with interstitials are not taken into account.

the Schottky contact can be described by

$$C(V) = \frac{\varepsilon A}{\sqrt{\frac{2\varepsilon}{qN_A}(V_{\mathrm{b}i} + V) + W_0^2\left(1 - \frac{N_A^p}{N_A}\right)}}, \tag{7.12}$$

where N_A is the bulk acceptor density. Thus, there are two fit parameters, namely the built-in voltage $V_{\mathrm{b}i}$ and the compensated acceptor density N_A^p. The best fits are obtained for the values $V_{\mathrm{b}i} = 2.1$ V, $N_A^p = 1 \times 10^{15}$ cm^{-3} and $N_A^p = 1.9 \times 10^{16}$ cm^{-3} for dose II and dose I, respectively. This shows, that indeed less than 5 % of the acceptors remain electrically active in the volume implanted with dose II, but around 80 % for the dose I.

Fig. 7.10 shows the ΔC_{SS} ODLTS spectrum as a function of photon energy for the different implantation doses. The waiting time to determine ΔC_{SS} was 200 sec. The unimplanted diode shows an increase in signal up to 1.15 eV, remains approximately constant in the range $1.25 \leq h\nu \leq 2.25$ eV and finally increases from 2.7 eV on. Upon implantation with C^+ ions three spectral regions can be distinguished. The low energy end of the spectrum from 0.5 eV to 1.3 eV is unaffected by implantation. At 1.3 eV a steep increase in signal is observed, saturating in the energy range 1.8 eV $\leq h\nu \leq$ 2.2 eV. The height of this plateau increases with increasing implantation dose. At 2.2 eV the signal increases again, establishing another constant value from 2.6 eV up to 3 eV. The height of this second step increases with the implantation dose as well.

In Fig. 7.11a three capacitance transients for different photon energies are shown. One can distinguish two time domains. In the region I ($0 < t < 2$ sec) a fast rise in the capacitance is detected, indicating a process with a small emission time constant. In region II ($5 < t < 20$

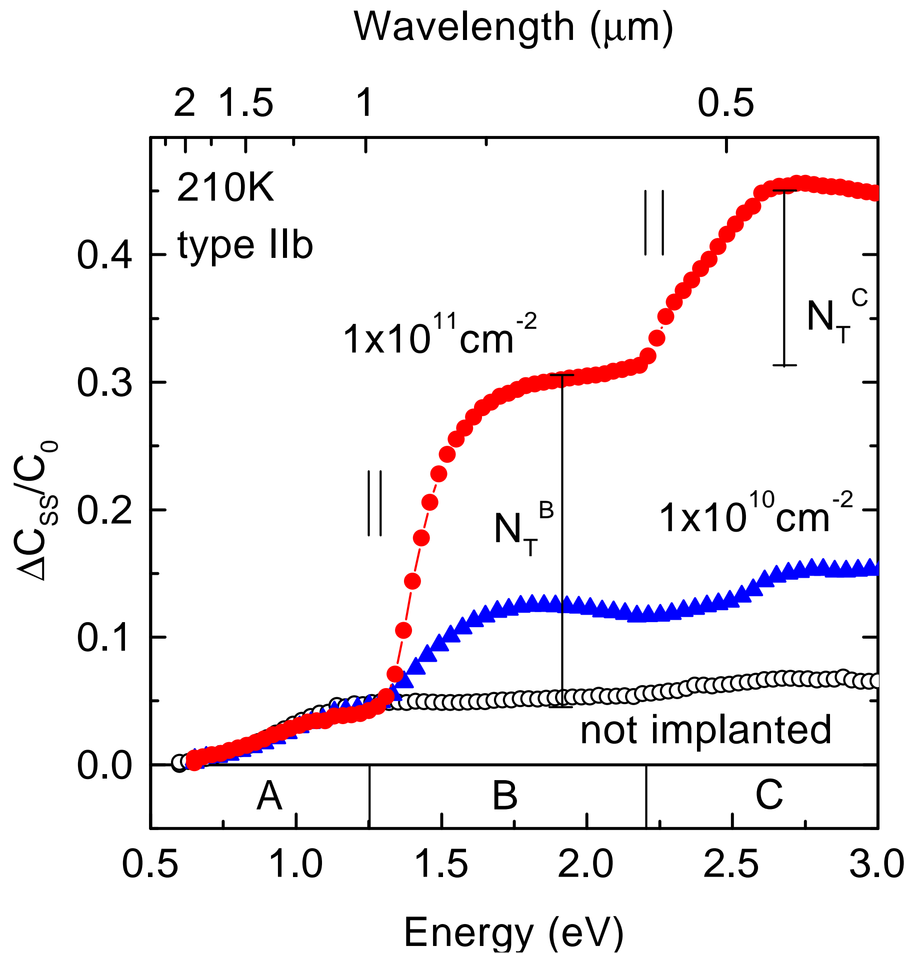

Figure 7.10: ODLTS signal for implanted and unimplanted type IIb diamond. Here $\Delta C_{SS}/C_0$ has been evaluated, representing the trap density.

sec) a more slowly increasing part can be seen, whose slope increases with increasing photon energy. These two regions represent two optical emission processes with different photoionisation cross sections σ_o. This is confirmed by the fact that the experimental transient can be very well reproduced by two exponential functions. Thus, plotting σ_o as obtained from the regions I and II will result in different spectra, representing the different defects causing the two emission processes. This is shown in Fig. 7.11b for an implanted (1×10^{11} cm^{-2}) and an unimplanted sample. The line graphs represent the photoemission rates with small time constant (i. e. for times $t < 2$ sec), whereas the symbol graphs represent the slow emission processes (i. e. $t > 5$ sec). For clarity, the curves of the two diodes are shifted against each other.

For the fast process (line graphs) no change upon implantation is observed in the range 0.8 eV $\leq h\nu \leq$ 2.3 eV. For photon energies $h\nu >$ 2.3 eV an increase in optical density after implantation is detected. For the slow process (symbol graphs), a strong change in

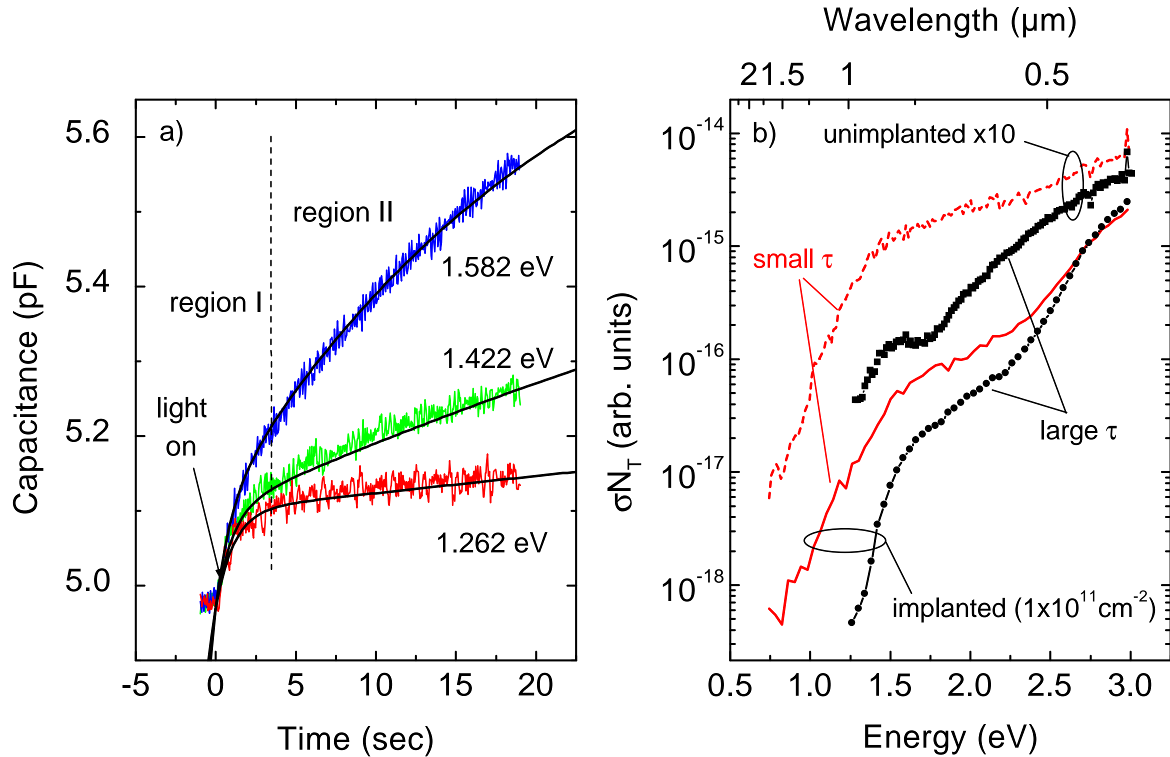

Figure 7.11: a) Capacitance transients for the sample implanted with 1×10^{11} cm^{-2} for different photon energies. A fast part (region I) of the transient in the the region $0 < t < 2$ sec followed by a slow rising part (region II) can be seen. b) Photoionisation cross sections of a type IIb diamond before (dashed line and open symbols) and after C^+ implantation (solid line and full symbols). The line graphs represent σ_o when evaluating the slopes of the transients in region I, whereas the symbols stand for the slopes evaluated in region II. For clarity the graphs for the unimplanted sample have been shifted upwards.

the spectrum upon implantation can be seen. Whereas only a small hump around 1.5 eV is detectable in the unimplanted sample, a clear absorption threshold at about 1.3 eV is observed in the implanted sample, which rises by nearly two orders of magnitude and shows an onset of saturation at around 1.7 eV. In this spectrum the increase in absorption for $h\nu >$ 2.7 eV can also be seen.

Since the differences between the implantation doses are only detectable for large τ (slow process), we show in Fig. 7.12 the $\sigma_o N_T$ spectrum for the unimplanted sample and two different implantation doses for the long time constants. The spectra have been normalised at 1.26 eV. Concerning the absorption starting at 1.3 V, one can clearly see an increase with increasing implantation dose. The same is true for the absorption starting at around 2.3 eV. This is fully consistent with the observation of the trap density obtained by the ΔC_{SS} evaluation (cf. Fig. 7.10), where an increase in trap density in the same energy ranges is found after implantation. A fit of the photoionisation cross section as presented in Sec. 2.3.2 for dose II is also shown (dashed line). It reveals a trap energy of 1.28 eV.

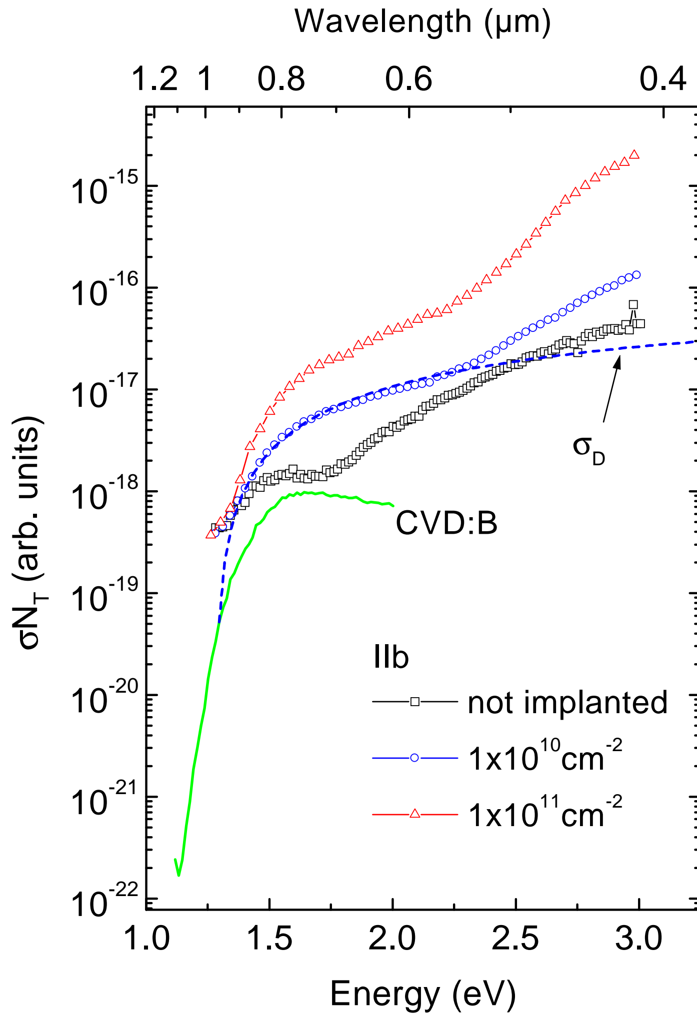

Figure 7.12: ODLTS signal for various samples implanted and unimplanted type IIb diamond samples as obtained from the initial slope technique. For comparison the spectrum of a CVD grown boron doped homoepitaxial diamond is also shown (solid line). The dashed line represents a theoretical optical cross section [Ink81], assuming an optical ionisation energy at 1.28 eV.

Annealing

The $C-V$ characteristics for the diodes after certain annealing steps are shown in Fig. 7.13. The $C-V$ curves of the sample implanted with dose II (lower graph) can be fitted by Eq. (7.12), assuming an increase of the compensation width W_0 after each annealing step. It increases from 230 nm (as implanted) to 400 nm (773 K anneal). A change of the passivated acceptor density N_A^p could not be determined, since a further decrease would not affect the fit. Three fitting curves are shown in the lower part of Fig. 7.13 with passivation widths W_0 of 230 nm, 320 nm and 400 nm. The $C-V$ curves of the sample implanted with dose I (upper graph in Fig. 7.13) can not be described satisfactorily assuming only an increase of W_0. An additional decrease of the passivated acceptor density N_A^p (i. e. increasing compensation) has to be taken into account. Two fits are shown with $W_0 = 230$ nm, $N_A^p = 1.8 \times 10^{16}$ cm^{-3} and $W_0 = 320$ nm, $N_A^p = 8 \times 10^{15}$ cm^{-3}.

In the following discussion we will refer to the three dominant absorption regions as

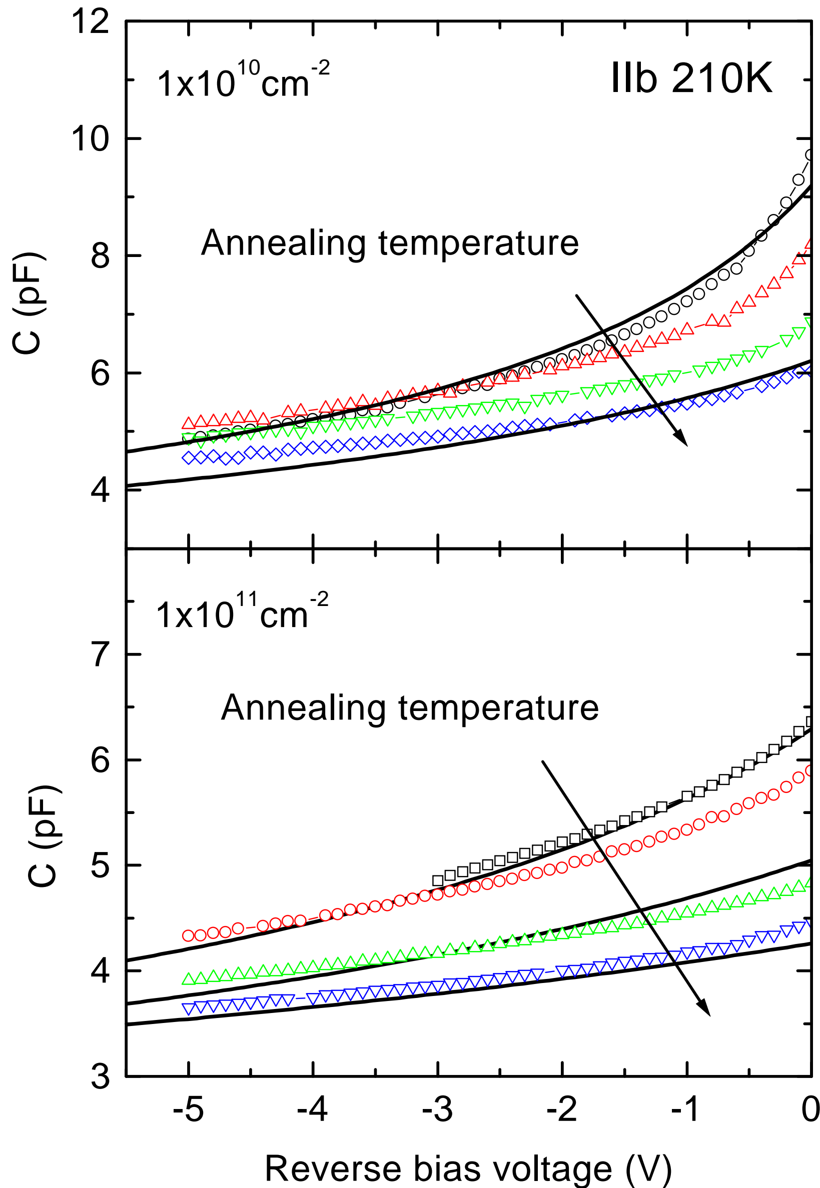

Figure 7.13: Change of the $C-V$ characteristics during 1h isochronal annealing of implanted diodes. The solid lines are fits according to Eq. (7.12)

region A (0.6 eV $\leq h\nu \leq$ 1.25 eV), region B (1.25 eV $\leq h\nu \leq$ 2.2 eV) and region C (2.2 eV $\leq h\nu \leq$ 3 eV). The ODLTS spectra ΔC_{SS} for selected annealing temperatures are shown in Fig. 7.14. The defect density in region B first stays approximately constant up to 550 K, then decreases rapidly between 550 K and 650 K, and finally remaining again approximately constant up to 773 K. The sample implanted with the lower dose shows a decrease to the same defect density after annealing. Another sample implanted with dose II was annealed at 1373 K for 10 min. The defect density after this annealing is approximately the same as for the other samples (open circles in Fig. 7.15). The temperature dependent defect density of the region B is shown in Fig. 7.15. Assuming first order annealing kinetics, the defect

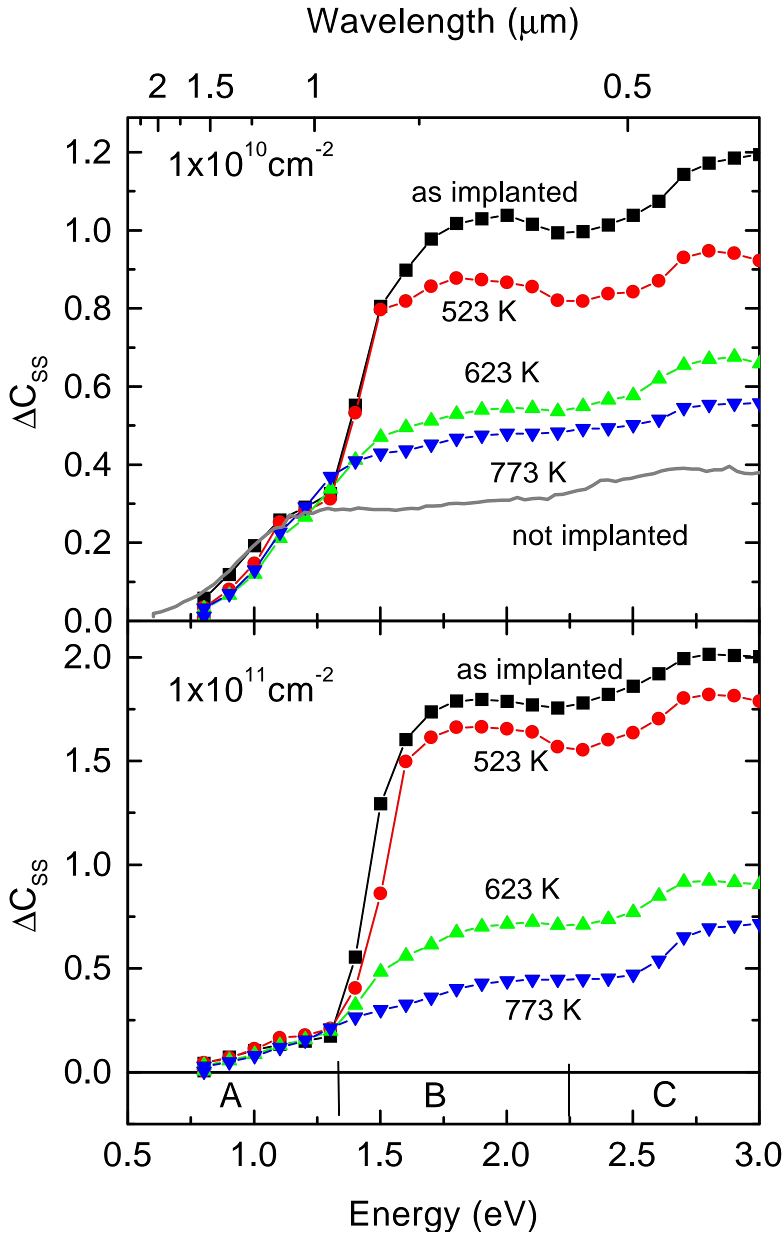

Figure 7.14: ODLTS spectra (ΔC_{SS}) during 1h isochronal annealing of implanted diodes (Implantation doses are 1×10^{10} cm^{-2} (upper graph) and 1×10^{11} cm^{-2} (lower graph). In the graph, the spectrum of an unimplanted diode is also shown (solid line).

density N_T can be described by

$$\frac{dN_T}{dt} = -rN_T \tag{7.13}$$

with the thermally activated annealing rate r

$$r = r_0 \, \mathrm{e}^{-\frac{E_m}{kT}}, \tag{7.14}$$

where E_m is the migration energy of the diffusing species and r_0 the rate prefactor of moving into a trapping site. This is given by the jump frequency, divided by the number of jumps

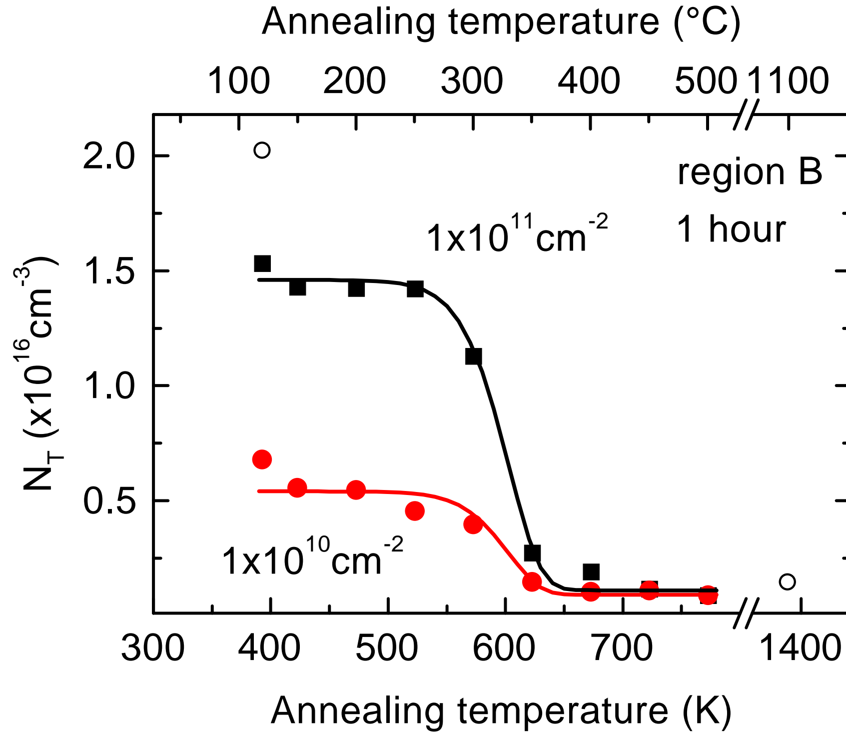

Figure 7.15: Trap density of the defect levels in region B during 1h isochronal annealing versus temperature. The solid lines are fits after a first order kinetics annealing, which yields a migration energy of 1.25 eV. The open circles represent another sample implanted with 1×10^{11} cm^{-2}, which was annealed at 1373 K for 10 min.

needed (n_j) to find a trapping site i. e. $r_0 = \nu / n_j$. Here, ν is assumed to be the frequency of a characteristic vibration, e. g. the Raman frequency 4×10^{13} s^{-1}. To estimate the number of jumps we can assume that this number corresponds to the ratio of lattice sites to trapping sites. The number of trapping sites is given by the detected defect density ($\approx 2 \times 10^{16}$ cm^{-3}) and the number of carbon atoms is 1.77×10^{23} cm^{-3}. This results in $r_0 \approx 1 \times 10^7/\mathrm{sec}$. Eq. (7.13) gives the remaining number of traps after annealing for time t_A

$$N = N_0 \, \mathrm{e}^{-r(T) t_A} + N_{\mathrm{res}}, \tag{7.15}$$

where the residual defect density N_{res} accounts for incomplete annealing. The use of the temperature dependent recombination rate r provides the relation $N(T)$. Using the value for r_0 as described above, the only fitting parameter is the migration energy E_m. The fits according to Eq. (7.15) for the trap in region B are shown as solid lines in Fig. 7.15. They reveal a migration energy of 1.25 eV.

The temperature dependence of the level in region C can not be evaluated reliably, since the minimum at 2.5 eV in the ODLTS spectra strongly influences the determined trap density. However, since the step height in the ODLTS spectrum is the measure for the defect density,

Energy range (eV)	Implantation dose (cm^{-2})	Step height (pF)	Eq.	Trap density cm^{-3}
	not implanted	0.26	(3.14)	2.1×10^{15}
0.6 - 1.25	1×10^{10}	0.25	(3.14)	2.0×10^{15}
(region A)	1×10^{11}	0.16	(3.14)	1.5×10^{15}
	1.1×10^{11}	0.18	(3.14)	1.7×10^{15}
	not implanted	0.05	(3.14)	2.2×10^{14}
1.25 - 2.0	1×10^{10}	0.44	(B.4)	7.3×10^{15}
(region B)	1×10^{11}	1.36	(B.4)	2.3×10^{16}
	1.1×10^{11}	1.2	(B.4)	2.0×10^{16}
	not implanted	0.07	(3.14)	5.4×10^{14}
2.0 - 3.0	1×10^{10}	0.19	(B.4)	3.2×10^{15}
(region C)	1×10^{11}	0.56	(B.4)	9.4×10^{15}
	1.1×10^{11}	0.6	(B.4)	1.0×10^{16}

Table 7.1: Calculated trap densities for the three dominant steps in the ODLTS spectrum in Fig. 7.10 for various implantation doses.

we can consider the defect density causing this absorption as approximately constant during the annealing procedure.

7.2.3 Discussion

The ODLTS signal $\Delta C_{SS}/C$ in Fig. 7.10 yields the trap density only in case of uniform trap distribution over the whole depletion layer. This condition is fulfilled for the unimplanted sample, so the trap density can be calculated by Eq. (3.14) and leads to densities in the range of 2×10^{15} cm^{-3}. This is also true for region A of the implanted samples, since this defect is not affected by implantation. The creation of the radiation induced traps however (regions B and C) is limited to 230 nm below the surface, which is only a fraction of the depletion layer width. Therefore Eq. (3.14) for calculating the trap density does not hold anymore. As shown in Appendix B, a relation is derived, which accounts for an inhomogeneous trap distribution. The actual defect densities – calculated with the appropriate formulas – for the regions A, B and C in the spectrum of Fig. 7.10 are given in Table 7.1. The error is estimated to be about 30%.

Obviously, the trap density in region B and C increases with the implantation dose, but the comparison of the created defect densities with the vacancy density as calculated with TRIM, shows a discrepancy by a factor of 20. Assuming that the observed defects are isolated vacancies or interstitials, leads to the conclusion that either 95 % of the primary created vacancies recombine immediately with their interstitials or that a second order process like

cluster formation is responsible for the creation of the observed defect density.

From the fit to the annealing data a migration energy of the defect of 1.25 eV has been found. This, as well as the low temperature where the defects anneal out, makes it unlikely that the diffusing species is the vacancy. For neutral vacancies, migration energies of 2.4 eV have been measured [Dav92] and typical annealing temperatures are 1070 K. Dannefaer *et al.* [Dan96] observed a decrease in the vacancy density at 1h isochronal anneal at 950 K. However, Lawson *et al.* [Law92] and Allers *et al.* [All98] observed two decay processes of the GR1 photoluminescence line (neutral vacancy). A slow one with a time constant of 77 h at 600 °C and a fast one with a time constant of 130 min at 460 °C. The latter one was attributed to the migration of the interstitial to the vacancy with subsequent annihilating. The extracted migration energy was 1.6 eV. Massarani and Bourgoin [Mas76] obtained 1.3 eV for the migration of the interstitial. The correspondence with the 1.25 eV obtained here suggests that the same process happens in our case as described by Allers *et al.*: The carbon interstitial becomes mobile at moderate temperatures (600 K), diffuses to and finally annihilates with the vacancy. The fact that the absorption does not fall to the intrinsic value even after annealing at 1370 K further supports the notion that the absorption in region B is caused by the vacancy.

Assuming that the vacancy is responsible for compensation [Kal97], the annealing behaviour of the $C-V$ data leaves some open questions: The capacitance also decreases upon annealing, which is due to an enlargement of the compensated layer width W_0. The participation of a donor mobile at 600 K is necessary to explain the increase of W_0. Although this seems much to low for the vacancy to become mobile, care has to be taken when comparing the results obtained in this work with the above mentioned literature data for the annealing temperatures of the vacancies. All of the samples investigated there were either IIa or type I diamonds, where the Fermi level is in the upper half of the band gap. According to Mainwood and Stoneham [Mai97] the vacancy is in a negative or neutral charge state in these samples, whereas in our type IIb samples we assume predominantly positively charged vacancies. Nothing is known about the migration energy of the positive vacancy, but it seems very likely that the migration of a positively charged vacancy is enhanced in our samples, since the processes observed here take place in the depletion layer of the Schottky junction, where the electric field can influence the motion of the vacancy. The presence of a considerable amount of neutral vacancies can be excluded in our samples, since we would expect to detect the characteristic quenching of the signal in the spectral region of the GR1 absorption as it is observed in photoconductivity [Ver81]. As can be seen in the spectra in Fig. 7.10, this is not the case here.

On the other hand, Massarani and Bourgoin state that the interstitial acts as a donor with a level 60 meV below the conduction band [Mas76], which can therefore also be responsible for the compensation of the boron acceptor. Adopting this assumption, it as a natural consequence that the compensated zone enlarges due to diffusion, when the interstitials become

mobile, i. e. at temperatures above 550 K. However, the donor character of the interstitial has not been established so far.

Positron annihilation spectroscopy in boron doped CVD diamonds as well as in natural type IIb diamonds support the assumption of positively charged vacancies clusters in these $p-$type layers. Dannefaer *et al.* [Dan96] detected only a very small fraction of positrons annihilating in vacancies at R. T. and attributed this to a Coulomb repulsion of the positron by the positive charge of the vacancy. The temperature dependent measurements of Uedono *et al.* [Ued99] revealed a sharp increase at 120 K of the intensity of the positrons annihilating in vacancies. The authors ascribed this to a charge state transition of the vacancy clusters from positive (above 120 K) to neutral (below 120 K).

Prins [Pri89] analysed the thermal dark conductivity of boron implanted and annealed layers. Based on Fermi-Dirac statistics he concluded from his data that the compensating centre is 1.23 eV above the valence band edge and attributed this to an agglomeration of vacancies. This is in good agreement with the result obtained here for the trap B.

More hints about the nature of the defects in region A and B can be obtained by comparing the $\sigma_o N_T$ spectrum with spectra obtained from diamonds grown under different conditions. For comparison, the spectrum of the CVD diamond discussed in 7.1 is also included in Fig. 7.12 (solid line). The spectral shape of the absorption around 1.5 eV is very similar to the one measured in a homoepitaxially grown boron doped CVD diamond film. Obviously, the responsible trap for the absorption in region A is not present in this sample, therefore the absorption in region B is more pronounced. For the CVD sample it has been shown in Sec. 7.1 that the region B absorption can be very well explained by assuming a defect at 1.28 eV above the valence band edge with a coupling to the lattice which is characterised by a Franck-Condon shift of 0.16 eV. It is worth noting that for the regions A and B, defect absorption has been observed in natural and synthetic type IIb diamonds and in boron doped CVD diamond films which can all be explained by assuming the two defects around 0.9 eV and at 1.28 eV [Zei98]. In combination with the results obtained here, the absorption in region B is attributed to a defect consisting of vacancies and/or interstitials, with an optical ionisation energy of 1.28 eV. The defect at around 0.9 eV is unaffected by carbon implantation, therefore it is more likely that it is caused by an impurity. Due to the fact that it is observed in many diamond samples, it should be related to a common impurity like nitrogen.

The comparison of the spectra evaluated for small and large time constants provides insight into the relative values of the photoionisation cross sections of the defects in region A and B. Considering the sample implanted with 1×10^{11} cm^{-2} (Fig. 7.11b)), we find that at 1.7 eV $\sigma_o N_T$ in region I is about 3 times larger than $\sigma_o N_T$ evaluated from region II. From the ΔC_{SS} spectrum (Fig. 7.10 and Table 7.1) it is known, that the defect density in region B is about 20 times larger than the one in region A. This implies, that the photoionisation cross

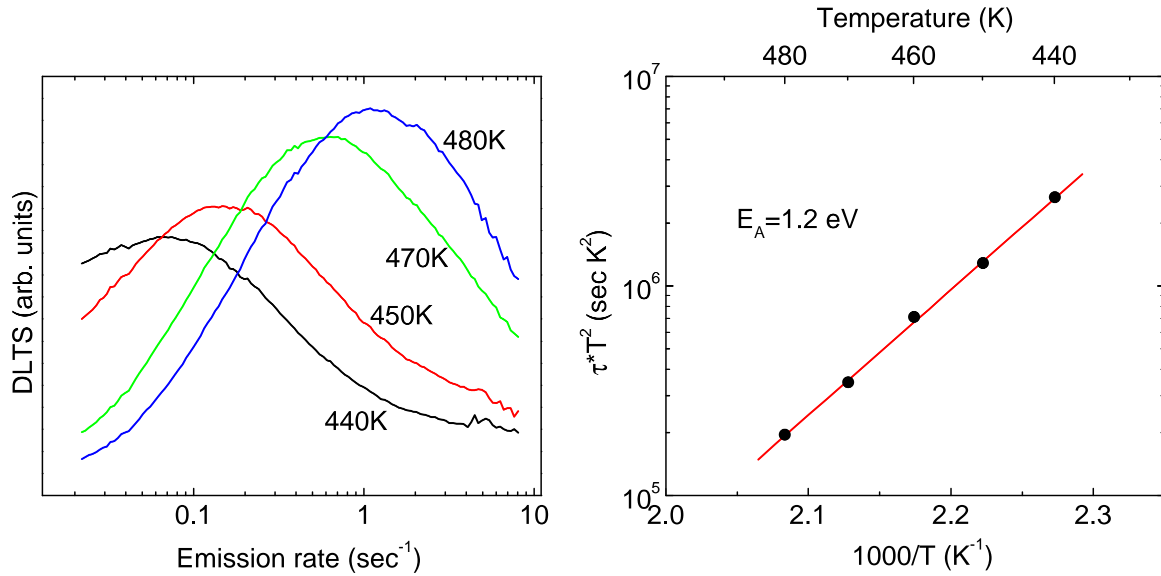

Figure 7.16: DLTS signals of a implanted type IIb Schottky diode (left). On the right, the corresponding Arrhenius plot is shown. It yields an activation energy of 1.2 eV.

section σ_o of the trap A is 60 times larger than the one of trap B. Using the the trap density as measured by the ΔC_{SS} method and typical photon fluxes of 10^{16} (cm^2 sec)$^{-1}$ into Eq. (3.28) leads to a photoionisation cross section of the order of 10^{-18} cm^{-2} for the 1.28 eV trap.

Nothing is known about the origin of the absorption in region C. The spectral shape of the ΔC_{SS} spectrum as well as the one of the $\sigma_o N_T$ spectrum can hardly be explained by assuming only one defect. Therefore we assume that at least two defects are responsible for the absorption in region C. Furthermore, as the shape of the $\Delta C_{SS}/C_0$ spectrum varies from diode to diode on the sample, influences of the contact properties cannot be excluded.

From the small Franck-Condon shift of the 1.28 eV defect, it was concluded in Section 7.1 that there is no capture barrier for holes associated with this defect. To check this assumption, DLTS measurements were performed on the implanted samples. In contrast to the CVD sample, DLTS experiments are possible here, due to the lower series resistance and smaller capacitance. The DLTS spectra and the corresponding Arrhenius plot is shown Fig. 7.16. The Arrhenius plot reveals an activation energy of 1.2 eV, slightly lower than determined by ODLTS. This supports the prediction of the model (cf. p. 59, that there is no capture barrier associated with this defect. Otherwise, DLTS as a non-equilibrium method, should lead to a value which corresponds to the thermal ionisation energy E_T plus the barrier energy E_B, i. e. significantly higher than the 1.28 eV (cf. Fig. 7.2). By use of Eq. (2.27) the capture cross section for holes can be calculated, which results in 9×10^{-15} cm^{-2}. Comparing this value with a typical value for a defect with a capture barrier (e. g. 10^{-18} cm^{-2} for Fe and Cr in GaAs [Lan75]) again manifests the non-existence of a capture barrier.

The following table summarizes the findings for the 1.28 eV defect, obtained in this work

Property		Value	
Trap energy above E_V	E_T	1.28	eV
Capture cross section (holes)	σ_h	9×10^{-15}	cm^{-2}
Photoionisation cross section	σ_o	10^{-18}	cm^{-2}
Franck-Condon shift	d	0.16	eV
Effective phonon energy	$\hbar\Omega_{\mathrm{eff}}$	35	meV
Tentative assignment		Positive vacancy (V^+)	

CHAPTER 8

Hydrogen-boron Interactions in type IIb Diamond

Hydrogen-defect interactions in semiconductors have been studied over many years and in a variety of materials [Pea92]. Concerning defect physics, hydrogen is of special interest, since bonding of hydrogen to defects substantially changes their properties. In amorphous silicon, hydrogen is known to passivate dangling bonds and therefore the electronic properties are improved [Sta80]. In crystalline semiconductors hydrogen forms complexes with defects leading to passivation in the case of shallow levels [Pea92] and new defect levels in the case of deep levels (i. e. Pt-H complex in Si [Sac99]). Interaction between hydrogen and point defects in natural or synthetic high temperature/high pressure diamond has received little attention up to now, since no hydrogen is present during the growth. The situation is different in chemical vapour deposited (CVD) diamond, which is grown in an atmosphere containing 99% hydrogen or more. Hydrogen bound to grain boundaries of polycrystalline CVD diamond is responsible for infrared absorption [Dis93, Fuc95] and for a number of EPR lines [Zho96]. Additionally, hydrogen microwave plasma treated diamond exhibits a highly conductive surface layer [Hay96]. However, hydrogen itself is not sufficient to create this effect, there is evidence that adsorbates are responsible for the surface conductivity [Gi99, Ris00].

Moreover, one would expect shallow level passivation by hydrogen similar to other semiconductors like Si, GaAs or GaN [Nak92, Bra98]. Chevallier and coworkers provided first evidence for electrical passivation of the boron acceptor after hydrogen plasma treatment [Che98]: Fourier infrared spectroscopy showed a decrease of absorption due to electronic transitions at the acceptor state, and SIMS measurements showed the characteristic plateau of the hydrogen concentration at the level of the boron concentration. In this chapter $C-V$ profiling of hydrogen or deuterium passivated synthetic type IIb diamonds are presented. They give additional evidence of the electrical passivation of the boron acceptor.

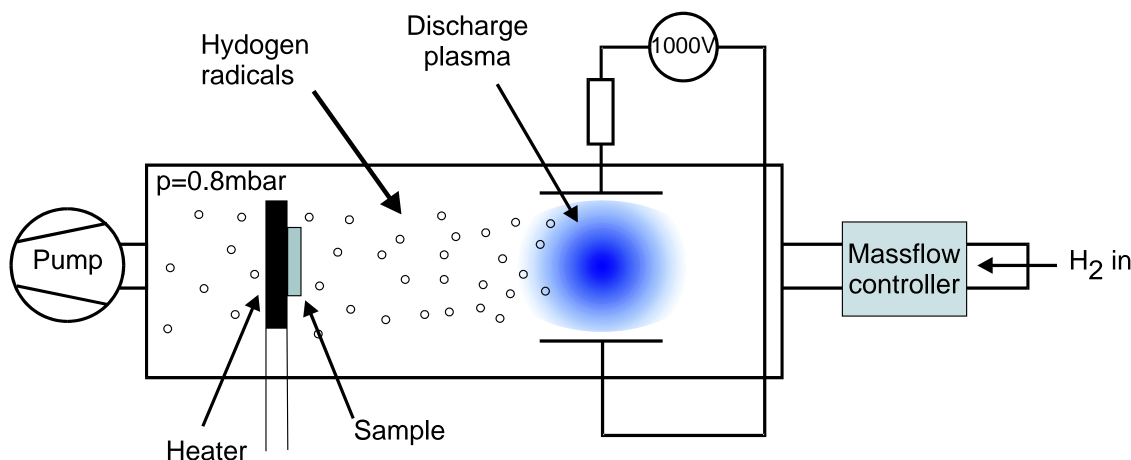

Figure 8.1: Hydrogen chamber for a DC remote plasma passivation.

8.1 Passivation reactor

In Fig. 8.1 the plasma reactor for hydrogen passivation is shown. It consists of a quartz tube wherein the sample is placed on a heated copper block. A typical sample temperature is 400 °C. The hydrogen or deuterium flux is established via a rotary pump and a mass flow controller which kept the flux at 20 sccm. The resulting pressure is 0.8 mbar. 10 cm upstream of the sample, the plasma is sustained by a DC discharge of 1.3 kV. Passivation times varied from 2 hours up to 24 hours. Before passivation, the samples are annealed at 900 °C in vacuum and kept in CrO_3:H_2SO_4 at 100 °C for two hours to remove any graphitic layer from the surface. After passivation, the samples are cooled down in the plasma and are again boiled in CrO_3:H_2SO_4 for one hour to remove deuterium from the surface, since it is known to affect the barrier heights of Schottky contacts [Moe94].

In addition to $C-V$ profiling, Hall experiments have been carried out. The investigated sample was a CVD grown boron doped diamond layer with 500 nm thickness on top of an undoped CVD buffer (12 μm) heteroepitaxially grown on a Si substrate. At room temperature, the free hole concentration of the untreated epi-layer is $(2.32 \pm 0.03) \times 10^{15}$ cm^{-3}. After passivation at 400 °C for 24 hours, the free hole concentration is $(1.01 \pm 0.02) \times 10^{15}$ cm^{-3}. After annealing at 900 °C for 10 min $(2.12 \pm 0.02) \times 10^{15}$ cm^{-3} holes are measured. These results indicate that indeed the free hole concentration is decreased after passivation and can be reactivated upon annealing. However, due to the polycrystallinity of the sample the hydrogen diffusion is strongly influenced by structural defects in the layer. To study the diffusive properties of hydrogen in diamond, single crystal samples are more suitable.

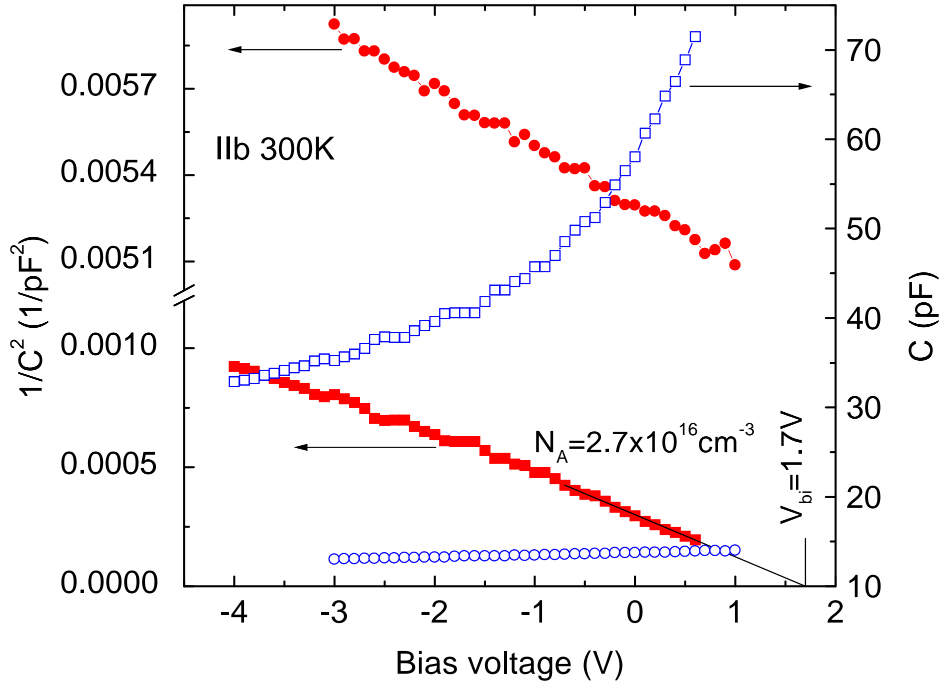

Figure 8.2: Capacitance voltage (open symbols) and $1/C^2$-data (solid symbols) of the deuterated (circles) and non-deuterated (squares) Schottky diodes on synthetic type IIb diamond.

8.2 $C-V$ profiling of passivated samples

In Fig. 8.2 the capacitance-voltage characteristics before and after deuteration of type IIb sample are shown. One can clearly identify a decrease in capacitance after deuteration. This corresponds to an increase of the depletion layer width, caused by a decrease of the effective acceptor density. From standard $C-V$-analysis (Sec. 2.4), one can calculate the acceptor density in the depletion layer volume from the slope of the $1/C^2$-plot. For the non-deuterated diode, we obtain an acceptor density of 2.7×10^{16} cm^{-3}. The built-in potential, determined from the intercept of a linear fit to the $1/C^2$-data with the abscissa, is 1.7 eV for the non-deuterated diode (Fig. 8.2). Applying these standard procedures to the deuterated diode, the slope would result in an acceptor density of 1×10^{16} cm^{-3} and a built-in potential of 26 V, obviously a meaningless value. Although the acceptor density appears to be smaller after deuteration, the value of the built-in potential is much too high for a Schottky barrier. So the standard $C-V$-analysis cannot be applied. Instead, we use the following model.

As it is known from secondary ion mass spectroscopy (SIMS) [Che98], the deuterium concentration profile is distinctly different from an error function distribution. Instead, it follows the boron density up to the penetration depth W_0 and then rapidly drops below the detection limit. We assume that in the region between the surface and W_0 deuterium–boron pairs are formed and therefore most of the boron acceptors are passivated. In this region the

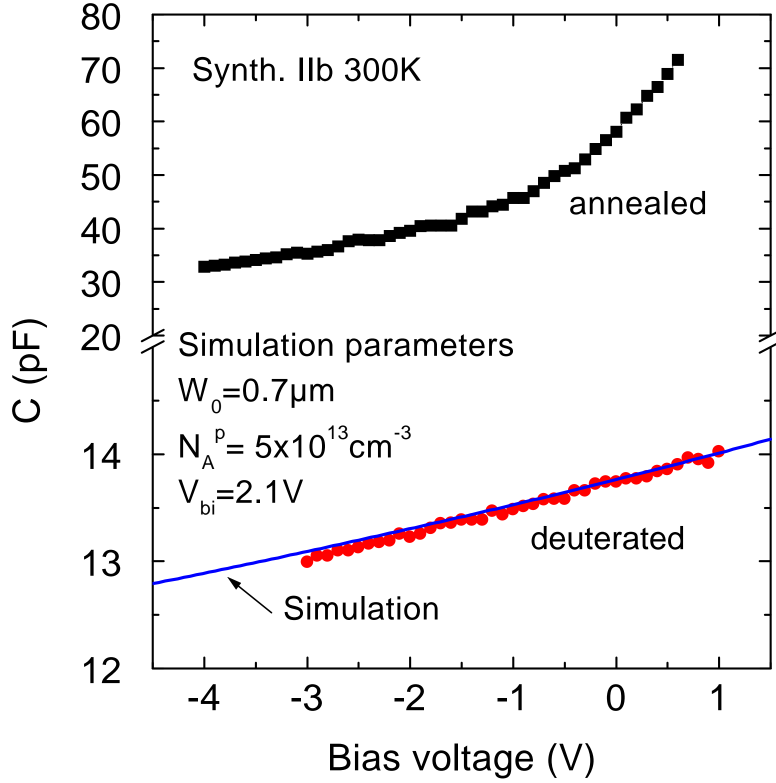

Figure 8.3: Capacitance–voltage characteristics of the deuterated (circles) und the non-deuterated (squares) diode. The solid line is a fit to the deuterated diode after the model presented in the text.

diamond becomes highly resistive and the Fermi level is shifted deep into the gap. In the region which has not been deuterated ($x > W_0$), the boron acceptors remain unpassivated and therefore the Fermi level is located at 370 meV above the valence band edge. Assuming a space charge distribution as shown in Fig. 8.6a, the $C - V$ characteristics – according to Appendix A – are described by

$$C(V) = \frac{\varepsilon A}{\sqrt{\frac{2\varepsilon}{qN_A}(V_{\text{bi}} + V) + W_0^2\left(1 - \frac{N_A^p}{N_A}\right)}}, \tag{8.1}$$

where N_A is the acceptor density in the unpassivated region and N_A^p the residual acceptor density in the passivated region. q is the unit charge and ε the dielectric constant of the diamond.

In Fig. 8.3 we plot $C(V)$ of the annealed (squares) and deuterated (circles) diode and a simulation of the deuterated capacitance according to Eq. (8.1). W_0 is obtained from the difference between deuterated and non-deuterated depletion layer width at zero bias which

is 700 nm. For $N_A^p < 10^{14}$ cm^{-3} and 2.1 eV for V_{bi}, we obtain a reasonable fit for the capacitance of the deuterated sample (see Fig. 8.3). This low residual acceptor density indicates that most of the boron acceptors have been passivated by deuterium. This is not surprising, since the SIMS data show that within the diffusion depth, the deuterium concentration equals the one of boron.

Heating the diode up to 400°C does not change the $C-V$-characteristics, but annealing at 900°C recovers the initial $C-V$-dependence.

The diffusivity D of deuterium can be calculated from W_0 and the deuteration time t, using

$$D = \frac{W_0^2}{t}, \tag{8.2}$$

which results in a value of 4.7×10^{-13} cm^2/s. Chevallier *et al.* report values of 8.5×10^{-14} cm^2/s at 400 °C. To understand the difference between these diffusion coefficients, it should be noted that the samples investigated in the work of Chevallier and coworkers were doped by 5×10^{19} cm^{-3}, while the sample in this work is only doped by 2×10^{16} cm^{-3}. The effect of doping density limited diffusion has been observed and modeled in boron doped silicon [Her90]. In this model, the effective diffusion coefficient is described by

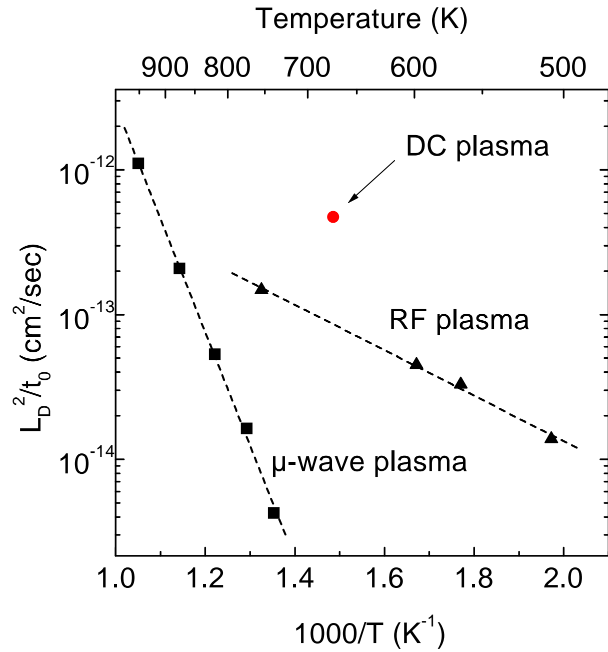

Figure 8.4: Diffusion coefficients as determined from various passivation techniques. The microwave and RF plasma passivation data are taken from Chevallier *et al.* [Che00].

$$D_{eff} = \frac{D_0 \, \mathrm{e}^{-E_m/kT}}{1 + r[B] \, \mathrm{e}^{E_B/kT}}, \tag{8.3}$$

where E_m and E_B are the migration and dissociation energies, respectively. $[B]$ is the fraction of boron atoms to lattice sites and r accounts for different hydrogenation conditions and configurational entropy of the hydrogen trapped at the acceptor. Up to now, the quantitative application of this model to the case of diamond is not possible, due to a lack of experimental data. Neither the migration nor the binding energy is known and the r factor differs between the available sets of experiments, due to different hydrogenation conditions. However, the tendency of an increasing effective diffusion coefficient with decreasing acceptor density can be qualitatively understood assuming trap limited diffusion.

Furthermore, it is worth noting that the measured diffusion coefficients strongly depend on the passivation method. As shown by Chevallier *et al.* [Che00], the diffusion coefficients as well as the activation energy of hydrogen diffusion strongly depends on the plasma source where the hydrogen radicals originate from (cf. Fig. 8.4). A microwave plasma leads to a higher activation energy and lower diffusivities than a RF plasma. In principle, the observation of different activation energies using different hydrogenation sources can be understood in terms of largely varying r factors in Eq. (8.3). Assuming $E_B > E_m$ as is the case for H in Si, D_{eff} is activated with E_B for high r values, whereas at low r factors E_m dominates at a given temperature. As stated by Herrero *et al.* [Her90], r decreases with increasing hydrogen flux. Keeping in mind that a microwave plasma has the highest hydrogen radical density, the results of Chevallier are in contradiction with this model. However, effusion experiments [Che00] show that a surface barrier exists for outdiffusion of hydrogen, which also affects the indiffusion. In this case, the measured activation energy is strongly influenced by variations of the barrier due to different hydrogenation conditions.

8.3 Bias annealing of passivated diodes

Another important issue of hydrogen diffusion is the charge state of the diffusing species. Here, $C-V$ analysis provides a method to probe the charge state by bias annealing of Schottky diodes. This procedure has been successfully applied to Si diodes [Tav85, Joh85, Zun89]. However, due to the high acceptor ionisation energy, the situation in diamond is different from the one in silicon. Whereas in silicon during passivation all acceptors are ionised, only a small fraction of boron acceptors are negatively charged at the passivation temperatures. If the hydrogen diffuses in a positive charge state, this would reduce the effective acceptor density, since due to the Coulomb interaction the hydrogen is attracted to the negatively charged acceptors.

As pointed out by Mehandru and Anderson [Meh94] the hydrogen released from a boron-hydrogen complex in diamond is either positively charged or neutral, corresponding to the two possible reactions

$$B:H \longrightarrow B_s^- + H_i^+ \tag{8.4}$$

$$B:H \longrightarrow B_s^- + H_i^0 + h^+. \tag{8.5}$$

To check which one of the two processes takes place, we have performed bias annealing experiments. For this purpose Ag Schottky contacts were deposited on a deuterium passivated sample. These diodes exhibit $C-V$ characteristics, which are shown in Fig. 8.5 (open symbols). The solid line is again a fit to the data according Eq. (8.1). To break up the boron

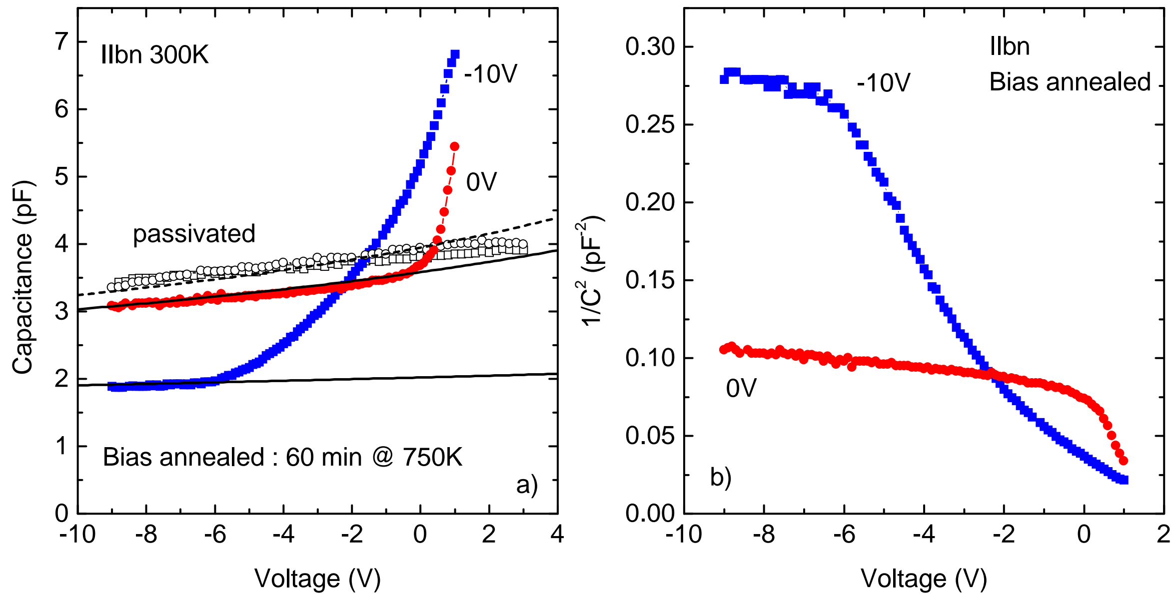

Figure 8.5: a) Capacitance–voltage characteristics of a deuterated (open symbols) and an annealed diode (full symbols) for different bias voltages during annealing. The solid lines are fits to the model presented in the text. b) $1/C^2$-plot of the annealed diodes.

hydrogen complexes, the diodes where heated to elevated temperatures with different applied bias. First, the diodes were heated within 30 min to 630 K, where $C-V$ characteristics were measured. At this temperature no significant change can be detected, indicating, that the B-H bonds are stable at 630 K. This is in agreement with the results of Chevallier *et al.* [Che00], who found no deuterium effusion at 630 K.

A similar bias annealing was then performed at 750 K. After 60 min the sample was cooled down to 300 K where $C-V$ characteristics were measured, which are shown in Fig. 8.5 (full symbols). Now, a significant change with respect to the passivated diodes can be seen. Again, this is consistent with the results of Chevallier *et al.* [Che00], where an onset of deuterium effusion at 770 K was reported. For the 10 V reverse biased diode, the capacitance is almost constant from -9 V to -6 V, similar to a fully passivated diode. From -6 V upward to 1 V, the capacitance is strongly voltage dependent, as for a normal Schottky diode. This can be seen more clearly in the $1/C^2$-plot in Fig. 8.5b. There is an almost constant value from -9 V to -6 V, whereas in the range of -6 V to 1 V an approximately linear behaviour is observed, characteristic for a normal Schottky diode.

However, for the diode annealed without bias (0 V), the behaviour is quite different. Here, the voltage independent part extends from -9 V up to 0 V. But from 0 V to 1 V, the capacitance increases strongly with voltage. This effect can be qualitatively understood by assuming a reactivated layer in the region of the depletion layer of the biased diode (Fig. 8.6b).

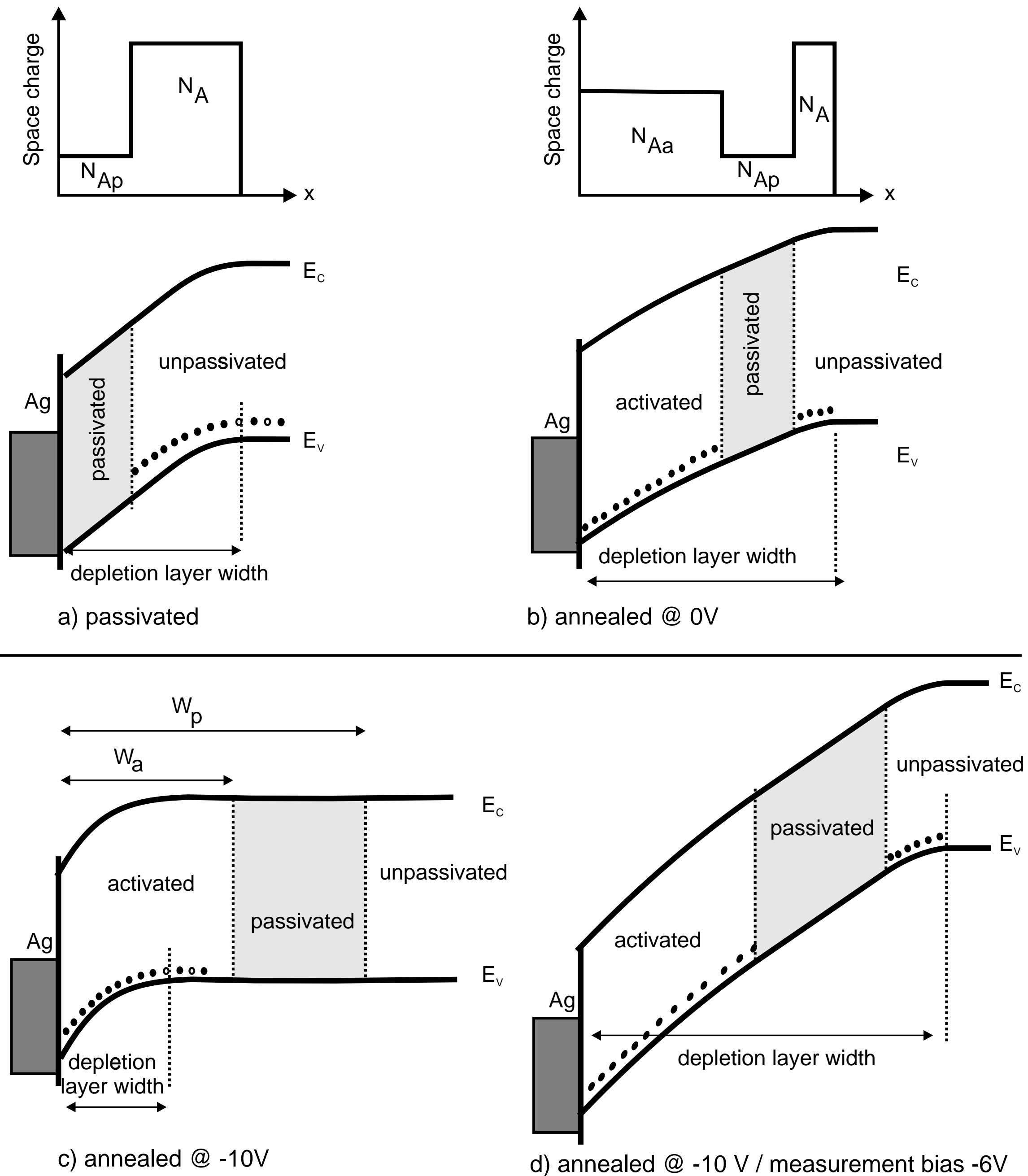

Figure 8.6: Schematic drawing of the energy band diagram near the surface of passivated and annealed IIb diamond Schottky diodes. a) passivated b) annealed at 0 V, measurement bias 0 V c) annealed at -10 V, measurement bias 0 V d) annealed at -10 V, measurement bias -6 V.

During annealing, the boron–hydrogen complexes are broken and the hydrogen is released. If the hydrogen is positively charged, it will drift in the electric field of the diode, thus being swept out of the depletion layer and finally be recaptured at the end of the space charge region by an unpassivated boron acceptor. As a consequence, the boron acceptors in

the depletion layer of the biased diode will be reactivated and the passivated layer will be shifted deeper into the bulk. One should keep in mind that even in the unbiased diode a space charge region exists due to the built–in electric field of the Schottky junction. A schematic picture of the energy band diagram before and after annealing is shown in Fig. 8.6a-c. The effect of shifting the passivated layer into the bulk is well known from Schottky diodes on p-type silicon, where similar bias annealing experiments have been carried out [Tav85]. The net acceptor profile then has been determined by $C-V$ measurements. It is worth noting that the Si diodes have been annealed at 150 °C – 200°C, whereas the diamond diodes in this work have been annealed at 480°C. Therefore one would expect a more pronounced effect due to the higher mobility of hydrogen at such elevated temperatures, since the migration energy for hydrogen in Si is 0.45 eV [Her90], whereas in diamond Mehandru and Anderson [Meh94] calculate a value of 0.1 eV.

Within this model, the $C-V$-characteristics of the annealed diodes can be interpreted as follows. Assuming that the passivated layer is shifted further into to bulk of the diamond due to the drift of the hydrogen in the electric field during annealing, we get a space charge distribution as shown in Fig. 8.6b. Integrating Poisson's equation twice yields the band scheme, which is shown in Fig. 8.6b. However, the reactivated acceptors are not sufficient to fully compensate the positive space charge in the metal. Therefore the depletion layer extends into the unpassivated region. This larger depletion layer gives rise to a smaller capacitance at 0 V bias anneal, than the one of the passivated diode. The voltage dependence is as small as for the passivated diode, since most of the voltage drops across the passivated layer. For small forward bias voltages (0 V to 1 V) the space charge region becomes so small that it no longer contains the passivated layer. Therefore the capacitance will become strongly voltage dependent. This effect can be seen in the $C-V$ characteristics.

For the diode annealed at -10 V bias, the hydrogen and thus the passivated layer is shifted deeper into the bulk and therefore the reactivated layer becomes larger. The width of this layer is larger than the depletion layer width at 0 V. As a consequence, the measured capacitance is bigger than for the 0 V annealed diode. The voltage dependence in this case is similar to a normal Schottky diode with decreasing acceptor density towards the passivated region. This can be clearly seen in Fig. 8.7 where the doping profile, calculated from the $1/C^2$ data after Eq. (2.46)

$$N_A = \frac{2}{A^2 q \varepsilon} \frac{1}{d(1/C^2)/dV} \tag{8.6}$$

is plotted. The data have been evaluated only up to -5 V, since at this voltage the depletion layer becomes so large that it reaches the passivated region. From this point on, the capacitance-voltage dependence is again flat, since most of the voltage drops across the highly resistive passivated layer. Both effects can be seen in the measured data.

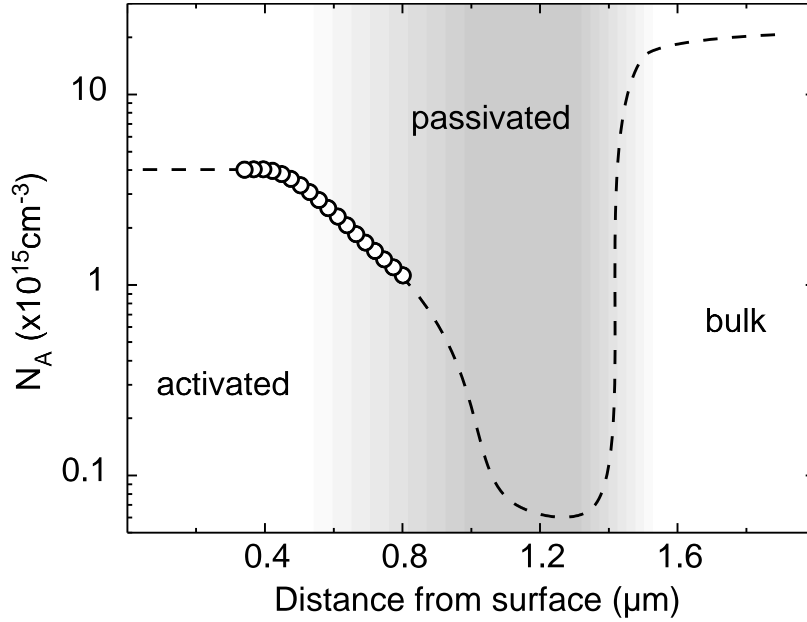

Figure 8.7: Acceptor density as a function of depth. The circles are calculated from the measured $1/C^2$ data. The dashed line is a sketch of the acceptor density after the model used for fitting the $C-V$ data.

The part of the $C-V$ profile, which is only weakly voltage dependent, i. e. where the depletion layer contains the passivated layer (Fig. 8.6b and d), can be fitted by a model similar to the one for the passivated diode, except that an additional layer – namely the reactivated one – must be taken into account. Solving Poisson's equation results in

$$W(V) = \sqrt{\frac{2\varepsilon}{qN_A}(V_{bi}+V) + W_p^2 + \frac{N_A^p}{N_A}(W_a^2 - W_p^2) + \frac{N_A^a}{N_A}W_a^2} \tag{8.7}$$

for the total depletion layer. The characteristic depletion layer widths W_a and W_p are defined in Fig. 8.6c. N_A^a, N_A^p and N_A stand for the reactivated, passivated and bulk acceptor densities, respectively. The other values have their usual meanings. Using this formula for the depletion layer width and $C = \varepsilon A/W$, the $C-V$ characteristics have been fitted. For N_A^a the value $4 \times 10^{15}\text{cm}^{-3}$ of Fig. 8.7 has been taken. For N_A^p an upper limit of $5 \times 10^{13}\text{cm}^{-3}$ has been used (Sec. 8.2). N_A was determined from $C-V$ profiling of untreated Ag Schottky diodes, which is $2.2 \times 10^{16}\text{cm}^{-3}$. It turns out that the fit is only weakly dependent on W_a but strongly dependent on W_p. For the 0 V annealed diode the fit parameters are W_a =500 nm and W_p =750 nm, for the 10 V annealed diode we obtain W_a =800 nm and $W_p = 1.4\mu$m.

Through these experiments, the charge state of the diffusing hydrogen can also be determined. From the fact that an electric field during annealing affects the hydrogen motion, it is clear that the diffusing hydrogen is charged. Since a reverse bias (Schottky metal positive and back contact negative potential) causes the hydrogen to move deeper into to sample the hydrogen must be positively charged.

CHAPTER 9

Li doped CVD Diamond

Despite intense research on shallow donors in diamond, only phosphorus has been reproducibly shown to be incorporated as a donor with an activation energy of 0.6 eV [Koi97]. In 1999 Sakaguchi *et al.* claimed that sulfur acts as an even more shallower n-type dopant with an activation energy of 0.38 eV and an electron mobility of up to 500 cm^2/Vs [Sak99], which, however, is controversially discussed at the moment [Kal99, Gar00].

Besides the group V elements nitrogen and phosphorus, the group I elements lithium and sodium have been predicted to act as shallow donors in diamond [And93, Kaj91]. For the interstitial lattice site, theory predicts an approximate energy level of 0.1 eV and 0.3 eV for Li and Na below the conduction band, respectively. Li on the substitutional site is predicted to have acceptor character [And93]. However, due to the the rigid diamond lattice the formation energies to incorporate a donor are rather high. Values of 5.5 eV for Li and 15.3 eV for Na have been calculated [Kaj91]. Within the low concentration limit, where the equilibrium solubility is given by (number of sites)$\times$exp$(-E_{\text{Formation}}/kT)$, this implies a vanishingly small solubility and therefore doping by in-diffusion will not be practical. This has been already confirmed experimentally. Nijenhuis *et al.*[Nij97] have performed optical and electrical characterization of Li-diffused type IIa diamond. Although SIMS measurements showed a Li concentration of up to 10^{20}cm^{-3}, no doping effect could be found. From their optical measurements they concluded that Li had segregated into small clusters, thus becoming electrically inactive.

A possible way to overcome the solubility limitation is the use of non-equilibrium processes like ion implantation or doping during CVD growth. The former has the disadvantage to create implantation defects which may act as compensation centers. There have been several attempts to dope diamond by Li or Na implantation [Pra93, Job96]. Although the Arrhenius plots of the conductivity data of implanted layers show activation energies between 0.1 and 0.2 eV, it is not clear whether these activation energies are due to a thermal excitation of a donor, especially, since the conductivity in the Arrhenius plots exhibits no strictly linear

relationship and the sheet resistances of the layers are very high. By plotting the resistance data vs. $(1/T)^{1/4}$, Prawer *et al.* showed that the dominant transport mechanism in these layers is variable range hopping [Mot87].

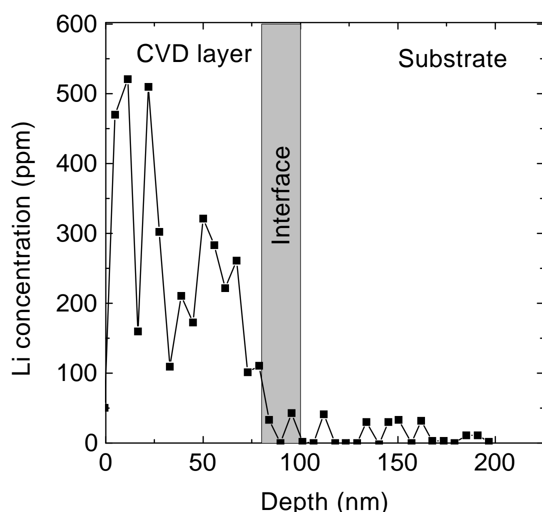

Figure 9.1: Depth profile of Li and H as measured by ERDA [Ste00a].

In this chapter results of dark conductivity and spectrally resolved photoconductivity (PC) experiments carried out on Li doped CVD diamond are presented. The samples were grown at the University of Augsburg in a microwave plasma CVD chamber on type Ib substrates [Ste99]. The substrate temperature was in the range between 620°C and 800 °C. Li has been added to the process gas by sublimating the organic precursor lithium-t-butoxide ($LiOC_4H_9$). The presence of Li in the plasma was monitored by optical emission spectroscopy (OES). The Li concentration was determined by elastic recoil detection analysis (ERDA) and was in the range between 4 ppm and 290 ppm. A typical depth profile is shown in Fig. 9.1.

Electrical contacts to the sample were made by standard photolithography using lift-off technique. Ohmic behaviour of the contacts was achieved using Ti (300 Å) Pt (150 Å) Au (1500 Å) which was annealed for 10 min at 600 °C .

9.1 Dark conductivity

According to theory Li should create a donor level 0.1 eV below the conduction band. However, in the samples investigated here no evident effect of shallow doping could be found. The resistivities of the layers were of the order of $10^{12}\Omega$cm at 300K . Due to the experimental limitation (R$\leq 10^{15}\Omega$), no activation energy for the conductivity could be measured below room temperature. The temperature dependent conductivity is shown in Fig. 9.2 and reveals no unique activation energy. Approximate values are 1 eV between room temperature and 500 K and 1.3 eV between 570K and 700 K. This result shows that indeed more shallower levels than the nitrogen donor at 1.7 eV have been introduced and that they govern the activation energy of the conductivity. However, these levels are much deeper than the 0.1 eV predicted by theory.

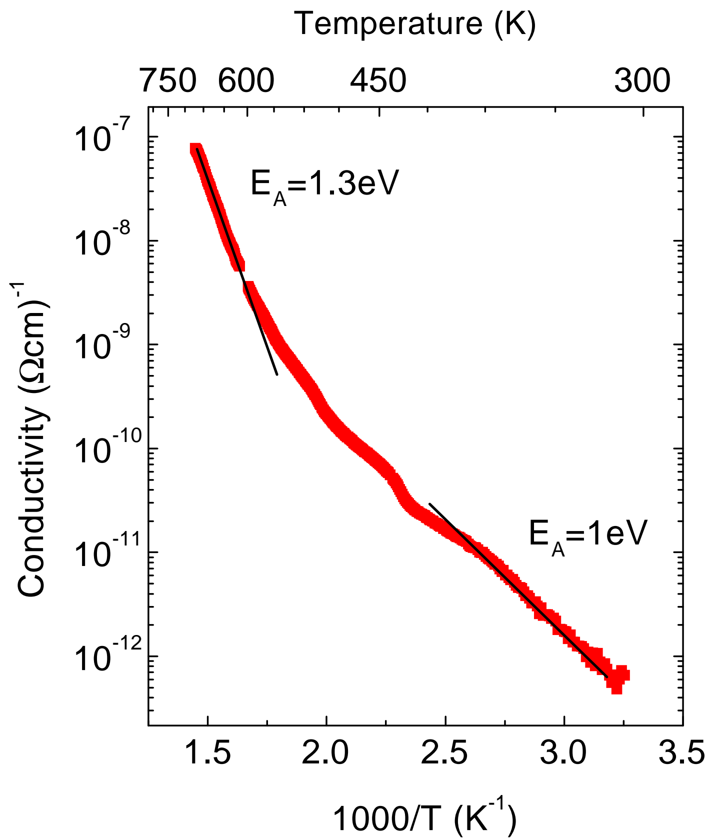

Figure 9.2: Temperature dependent dark conductivity of a Li doped CVD diamond layer on a type Ib substrate. The curved Arrhenius plot indicates a combination of various transport mechanisms.

9.2 Photoconductivity

To obtain a more complete picture of the Li induced defect states, photoconductance (PC) measurements have been performed. In Fig.9.3 a typical PC spectrum of a Li doped CVD diamond at 100K (solid line) is shown. One can clearly see the absorption of the N deep donor starting at 2.0 eV which probably arises from the Ib substrate. For comparison a PC spectrum of a bare Ib crystal is also included in the plot (dotted line). In addition to the nitrogen photoionisation, an absorption starting at 1.5 eV is detected. This feature has also been observed in photothermal deflection spectroscopy (PDS) on heteroepitaxially grown Li doped CVD diamond layers [Nes96].

Scanning a second time at 100K without heating the sample, a peak shaped photoresponse arises at $h\nu \approx 1.0$ eV (dashed curve in Fig.9.3). This absorption vanishes after annealing the sample at room temperature.

The occurrence of peaks in the photoconduction spectra of 3D-solids is unusual. A photoionisation spectrum of a deep level normally shows a shoulder or a very broad peak, which results from the continuous density of states of the band involved in the optical transitions. Although peaks in photoconductivity have been observed in diamond (e. g. the GR2-8 and

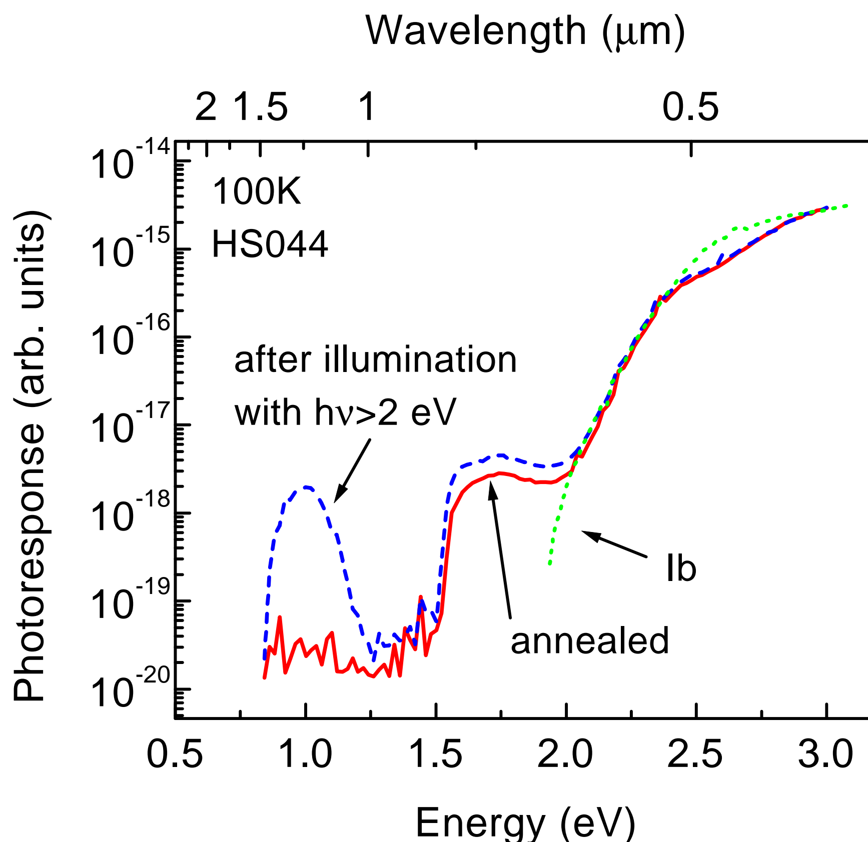

Figure 9.3: Photoconductivity of Li doped CVD diamond. The solid line represents the spectrum after cooling down in the dark. After illumination with photons $h\nu > 2.0$ a peak at 1.0 eV is obtained (dashed line). The dotted line represents the photoconductance of a type Ib single crystal.

ND1 lines [Far72]), it is supposed that the peak observed in the present spectra is due to a redistribution of charge carriers during the measurement. The line widths of the centers mentioned is around 0.05 eV or less and is tentatively explained by either photothermal ionisation [Kog77] or an excited state of the defect resonant with the conduction band. This state, once excited, immediately loses its electron, and therefore contributes to the photoconductivity. However, the width of the peak observed here is 0.3 eV. This is hardly compatible with the explanations given above, since typical width of photothermal ionisation peaks of i. e. the boron acceptor in CVD diamond are 60 meV [Roh98].

Instead the following model is suggested. Assuming a defect at $\approx E_C - 0.9$ eV and a Fermi level located around $E_C - 1.4$ eV, the level at 0.9 eV will not be occupied after annealing the sample, since the occupation is in thermal equilibrium. Therefore no photoconductivity will occur around 0.9 eV photon energy. This corresponds to the first spectrum (solid line). If electrons are optically excited into the conduction band by light ($h\nu > 2.0$ eV) they will be partially trapped at empty states above the Fermi level, giving rise to a metastable

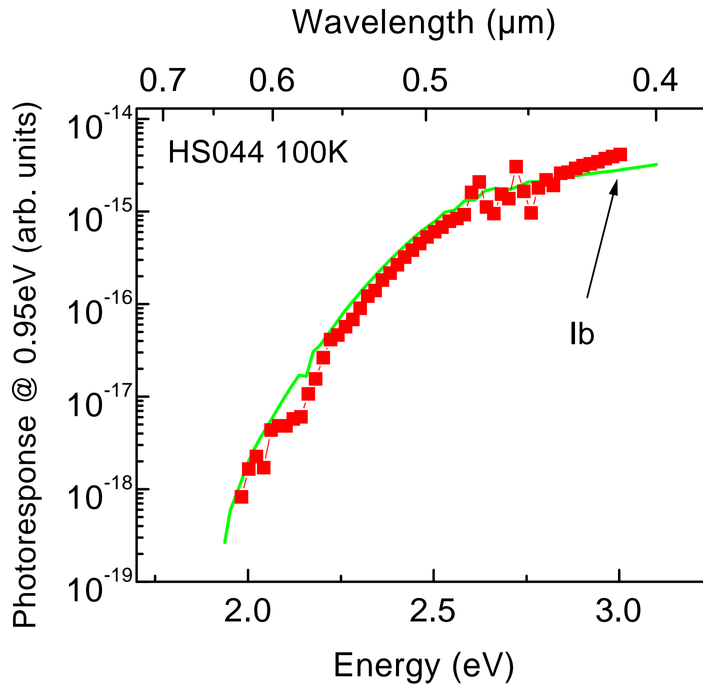

Figure 9.4: Photoconductivity excitation spectrum at a detection wavelength of 1300 nm (0.95 eV) of Li doped CVD diamond (full symbols). The excitation follows the photoionisation of the nitrogen donor (solid line).

occupation of the 0.9 eV level. It is now clear that during the second measurement (dashed line), electrons are transferred from the 0.9 eV defect into the conduction band but will not recombine with the defect where they originate from, but with another deeper trap, which is near the Fermi level (Fig. 9.7). In this case the photoionisation helps to approach thermal equilibrium, by transferring electrons from the 0.9 eV level to a defect closer to the Fermi level. Therefore the occupation of the defect is changed during scanning, and for photon energies larger than its photoionisation threshold, no photoconductivity will be detected, since all electrons have already been transferred to deeper levels.

9.3 Photoconductivity excitation spectroscopy

Photoconductivity excitation spectroscopy (PCE) is an appropriate tool to study the trap filling mechanism of the 0.9 eV level. The principle of this experiment is to measure the photoconductivity at 1300 nm (0.95 eV) (defined by an interference filter with a bandpass of 50 nm), while simultaneously shining excitation light on the sample. In order to separate the photoconductivity originating from the two light beams, the detection light is chopped while the excitation light is continuous. The wavelength of the excitation light was scanned from 1240 nm (1 eV) to 413 nm (3 eV). The result of this measurement is shown Fig. 9.4. Up to 2 eV no signal in the PCE can be detected. For $h\nu > 2$ eV, a strong enhancement can be seen and the spectral shape follows the photoionisation of the nitrogen donor, whose photoconductivity is also shown in the plot (as obtained from a photoconductance measurement on

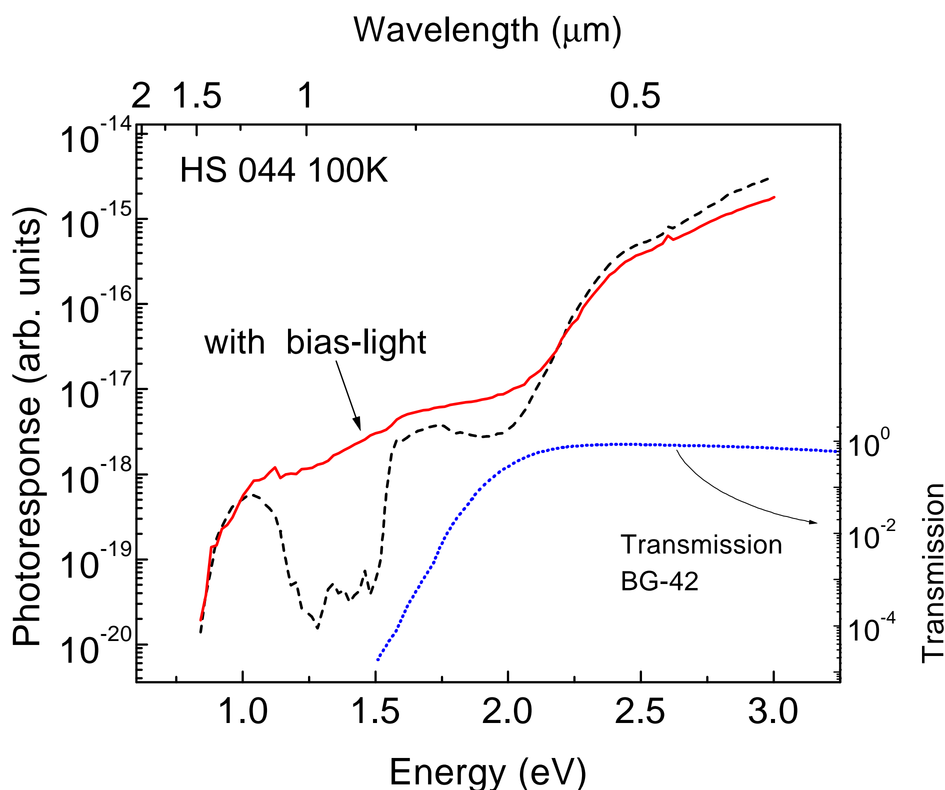

Figure 9.5: Bias enhanced photoconductivity (solid line) and PC without bias light (dashed line). In addition the dotted curve indicates the spectral transmission of the filter used for broad band excitation of the 0.9 eV level.

a type Ib diamond). Obviously, the photoionisation of the nitrogen donor is responsible for the photosensitization of the 0.9 eV level. However, it is not clear from this measurement, whether the N donor itself is directly responsible for the photosensitization (i. e. empty states at 1.7 eV) or if it is just the increased carrier density in the conduction band.

Next, a bias-light enhanced photoconductance measurement was performed. Here, in addition to the monochromatic, chopped light, the sample was illuminated with the light of a halogen lamp passed through a BG-42 filter, whose transmission curve is shown in Fig. 9.5. This bias illumination gives rise to a continuous filling of the shallow traps, whereby a steady state occupation of the 0.9 eV level was achieved, which can be probed now by the spectroscopic light. The result of this experiment is shown in Fig. 9.5 (solid line). The minimum at 1.25 eV is lost and a continuous absorption spectrum is detected as it is typical for a defect to band transition. The region between 1.5 eV and 2.0 eV is also enhanced by the bias light, leading to the conclusion that the defect at 1.5 eV is also metastably occupied.

Concerning the microscopic nature of the defects detected in these Li doped samples, one would wonder whether they are introduced by Li itself. No correlation between Li concentration detected by ERDA and the defect absorption at 1.7 eV can be deduced, but a

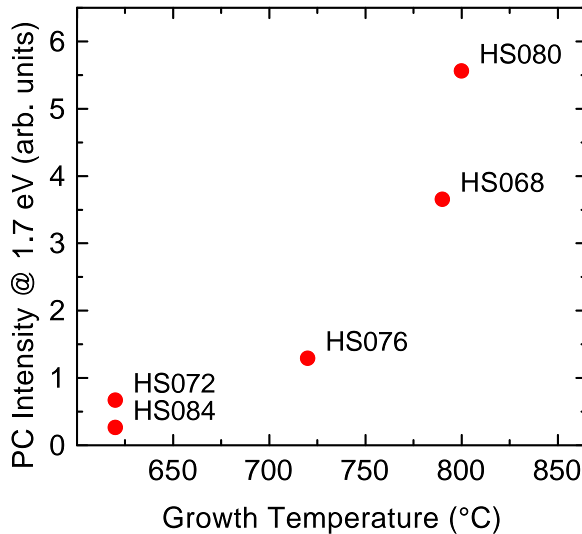

Figure 9.6: Photoconductance at 1.7 eV photon energy versus growth temperature.

correlation with the growth temperature is found. (cf. Fig. 9.6). From ERDA measurements, it is known that other impurities like iron, nickel and cobalt are present in concentrations of $\approx$ 30 ppm [Ste99, Ste00a]. Although the luminescence line of Ni at 1.4 eV is well known [Col92], there is no photoconductivity associated with this element. The other metals can also be excluded, since they are commonly used as catalysts in HPHT synthesis [Dav94] and no photoconductivity associated with these impurities is reported. Turning to the organic Li source itself ($LiOC_4H_9$) one can imagine oxygen as a possible impurity in the layers. However, ERDA measurements only reveal an upper limit of 100 ppm for the oxygen concentration. Effects due to isolated vacancies are also excluded, since the GR1 center at 1.67 eV should quench the PC and the GR2-8 lines should give rise to peaks in the range of 2.85 eV $\leq h\nu \leq$ 3.15 eV [Ver81]. No such effects can be detected in the diamond layers. Furthermore, cathodoluminescence measurements did neither show the GR1 nor the ND1 center, which are related to the neutral and negative vacancies, respectively.

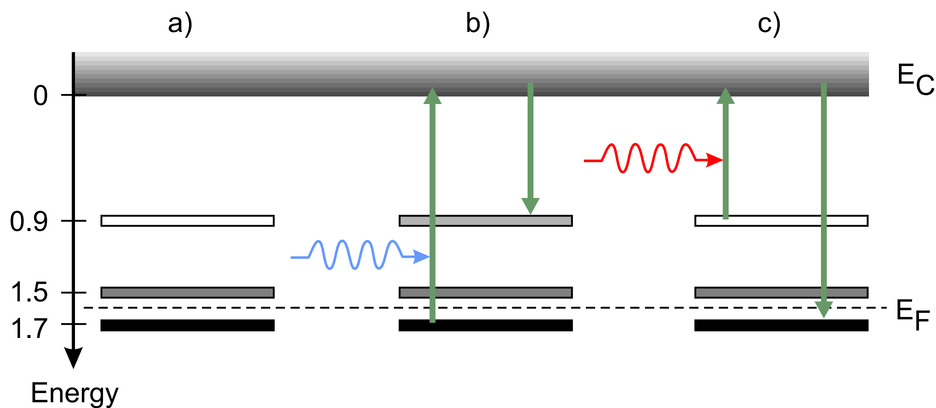

Figure 9.7: (a)Energetic position of the levels found in Li doped CVD diamond. Scheme of transitions between the different levels during photoexcitation (b) and bleaching (c).

Assuming that Li is related somehow with the level at 0.9 eV, the experimental observations can be explained within the following model. During growth, a level at 1.5 eV is created with the participation of an entropy enhanced defect[1] (i.e vacancy or interstitial). For undoped samples this level would not be detectable, since the Fermi level, due to nitrogen, is at 1.7 eV. Introducing the hypothetical level due to Li at 0.9 eV, electrons will be donated to the empty states at 1.5 eV, rendering the 0.9 eV level empty. The idea of transferring electrons to the 1.5 eV level is supported by the observation of the same spectral PC around 1.5 eV in lightly phosphorus doped samples [Hae00]. Here P has the same effect as Li of donating electrons. In Fig. 9.7 the levels detected in the Li doped layers are summarized together with the main excitation mechanism.

[1]The entropy enhancement accounts for the fact that the defect density increases with temperature

CHAPTER 10

Group-III Nitrides

The group-III nitride system consists of InN, GaN and AlN and their ternary and quaternary alloys. The equilibrium lattice structure is the hexagonal wurtzite structure, but there exist also cubic forms [Bra95]. The lattice constant and the band gap of the nitride system is shown in Fig. 10.1. Additionally, diamond, Si and the GaAs-GaP system are also included. Direct and indirect band gaps are visualized by blue circles and red squares, respectively. Contrary to diamond, the bandgap of the nitrides is direct and can be varied from 1.9 eV (InN) over 3.4 eV (GaN) to 6.2 eV (AlN). This fact makes the nitrides also superior to the GaP-GaAs system commonly used for LEDs in the red to green region, since $GaAs_{1-x}P_x$ has an indirect band gap for $x > 0.45$.

For lack of an inexpensive lattice matched substrate, the nitrides are grown heteroepitaxially on sapphire ($\alpha-Al_2O_3$), but also 6H-SiC is used, which, however, is more expensive. The lattice mismatch between sapphire and GaN is 16 %, which is partly responsible for the high dislocation density of 10^{10} cm^{-2} of the epitaxial layers. However, due to the high growth rate (100 μm/h) of hybrid vapour phase epitaxy (HVPE) [Gol98] it is possible to grow thick GaN within a few hours, which may provide substrates for homoepitaxial growth. The most common growth method for epitaxial layers is metal-organic vapour phase epitaxy (MOCVD) [Amb96]. Here, the nitrogen source is ammonia and the metals are provided by metal organic compounds like Triethyl-Gallium or Trimethyl-Gallium. As carrier gas hydrogen is used. This results in a rather high impurity contamination of the layers with carbon and hydrogen. Besides MOCVD, molecular beam epitaxy (MBE) is also suitable for nitride growth [Ang98]. Here, the most commonly used nitrogen source is plasma cracked molecular nitrogen. This results in a much lower impurity concentration in the layers compared to MOCVD growth. Like diamond, GaN can also be grown in a high pressure/ high temperature synthesis, where liquid Ga at typically 1700 K is encapsulated in a nitrogen pressure of about 1.5 GPa. This results in crystals of a few millimeter in size [Grz93]. Unfortunately, the free electron density of those crystals is up to 10^{20} cm^{-3} due to oxygen contamination of

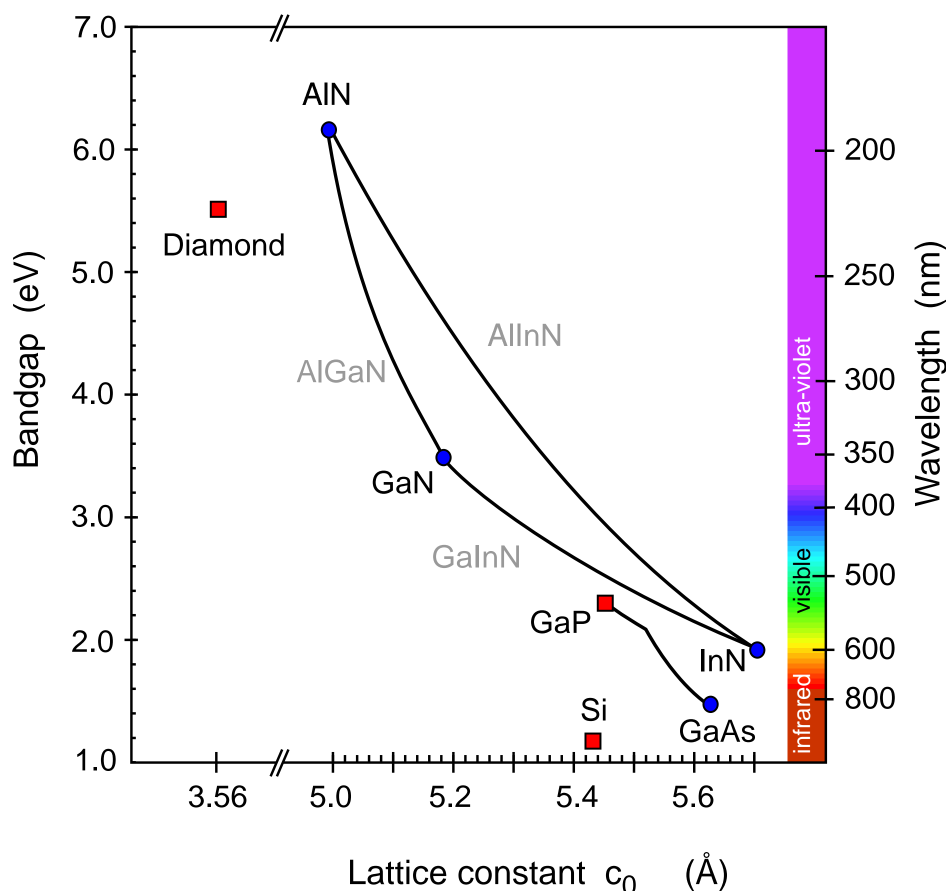

Figure 10.1: Band gap of the nitrides versus c lattice constant. For comparison, the cubic crystals diamond, Si and the GaP-GaAs system are included. The latter one is up to now the most important one for LED devices. The circles indicate a direct bandgap, while the squares stand for a indirect band gap.

the source gas or from the reactor walls.

A peculiarity of the nitrides is spontaneous and stress induced polarization [Amb99]. The lack of inversion symmetry and the strong ionic character of the chemical bond, which transfers electrons from Ga to the N atom, results in a high spontaneous polarization of the crystal. If the layers are strained when grown heteroepitaxially, an additional strain-induced or piezoelectric polarization adds to the spontaneous one. This causes electric fields of several MV/cm in the material [Amb99]. In AlGaN/GaN heterostructures this effect leads to accumulation of charge carriers at the heterostructure interface, even without intentional doping. This effect is used to fabricate field effect transistors [Dim00].

Nominally undoped GaN is always n-type with carrier concentrations of the order of 10^{17} cm^{-3}. Two possible donors have been discussed to be responsible for this unintentional doping, namely the nitrogen vacancy [Pan75, Loo97] and substitutional oxygen [Chu92, Mei00]. Furthermore, Si is a donor with an activation energy of 26 meV in GaN when in-

corporated on the Ga site. The incorporation of Si is very easy, since the sticking coefficient is approximately 1 [Ang98]. The most prominent acceptor is magnesium with a thermal activation energy of 170 meV [Göt96]. This large activation energy includes, as in case of B in diamond, that only a fraction of Mg acceptors is ionised at room temperature. Additionally, the low sticking coefficient hampers an effective incorporation of Mg into the layers. Only about 1% of the available atoms is incorporated into the layer during epitaxial growth [Dim00]. Furthermore, when Mg doped GaN is grown via MOCVD, Mg-hydrogen complexes are formed, leading to a passivation of the Mg acceptor [Bra98], which results in a deep level at 1.12 eV above E_V [Roh98, Yi96]. Therefore an annealing step has to be done to reactivate the Mg acceptor after growth. Besides Mg, beryllium, cadmium and zinc have shown acceptor characteristics [Lag74].

CHAPTER 11

Si in AlGaN Alloys

For n-type doping of the AlGaN system, Si is most commonly used as the donor. Doping AlGaN alloys with silicon results in a significantly decreased activation energies of the dark conductivity with respect to the unintentionally doped samples (cf. Fig. 11.1). The activation energy increases from 18 meV (GaN) to 320 meV (AlN). In contrast, the activation energy of similarly prepared but nominally undoped alloys are much higher (open circles in Fig. 11.1). Assuming a shallow effective mass character of the Si donor, one can compare these experimental results with the values calculated with the hydrogen model for shallow donors.

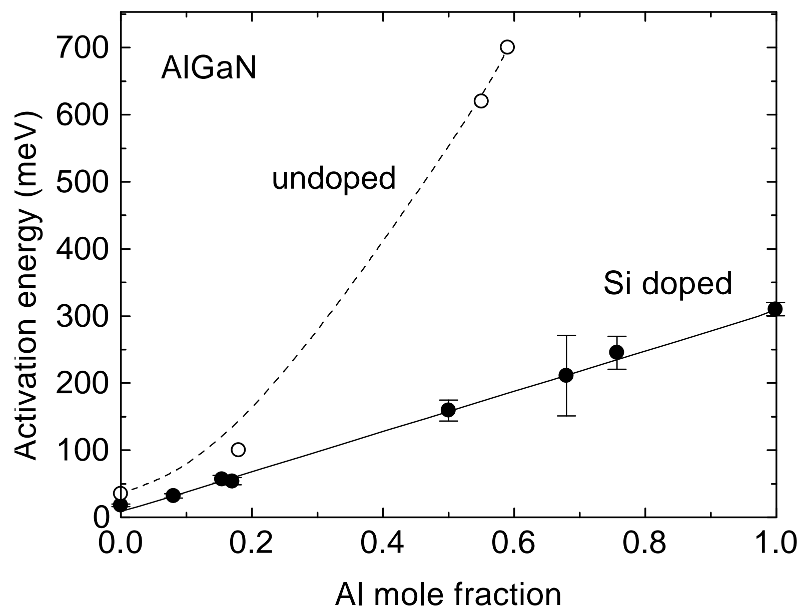

Figure 11.1: Activation energies of the dark conductivity of Si-doped (full circles) and nominally undoped (open circles) $Al_xGa_{1-x}N$. The lines are a guide to the eye.

Material	eff. mass m_0	ε_S	E_d^{theo} meV	E_d^{exp} meV
Ge	0.082…1.64	16.0	4.08…87.4	9…12
Si	0.019…0.98	11.9	18…94	21…54
GaAs	0.067	13.1	5.3	6
Diamond	0.88	5.7	378	374
GaN	0.18…0.2	9.53	22…29	22…36
AlN	0.33	8.5	62	320

Table 11.1: Calculated (E_d^{theo}) and measured (E_d^{exp}) values of the ionisation energies of shallow dopants in various semiconductors. A range of value accounts for an anisotropic effective mass.

Within this model, the ionisation energy E_d of an effective mass donor is described by

$$E_d = \left(\frac{1}{\varepsilon_S}\right)^2 \left(\frac{m^*}{m_0}\right) E_H, \tag{11.1}$$

where ε_S is the permittivity of the semiconductor, m_0 is the mass of the free electron and m^* the effective mass of the charge carrier in the band. E_H =13.6 eV is the ionisation energy of the hydrogen atom. As can be seen, E_d strongly depends on the dielectric constant of the semiconductor, i. e. the smaller it is, the higher is E_d. As shown in Tab. 11.1, this simple approximation predicts the depth of the shallow levels very well for a wide range of semiconductors, including GaN. For AlN however, there is a difference of more than a factor five between the calculated and the measured value. Although corrections to the simple hydrogen model (e. g. central cell corrections) have not been taken into account, it is obvious that Si is no shallow donor in AlN, a transition from a shallow to a deep state must has taken place. This can be well understood in terms of a structurally relaxed Si donor atom, the so called DX-state. This model has been proposed by Chadi and Chang [Cha88] to explain the observations concerning Si in AlGaAs alloys. In these alloys it is known from previous work [Lan92, Lan77, Moo92] that Si – from a certain Al content up – can lower its energy by a large lattice relaxation and the capture of a second electron, the so called DX transition

$$2d^0 \rightleftharpoons d^+ + DX^- + U. \tag{11.2}$$

Here d denotes a substitutional shallow impurity and DX the relaxed deep state. The superscripts specify the charge states. The donors d^0 need not be spatially close to each other. U stands for the correlation energy, which is negative and favours the capture of a second electron. The structural relaxation of the Si atom in AlN is shown in Fig. 11.2. Due to the wurtzite structure of the nitrides, two inequivalent relaxed sites are possible: Either the bond

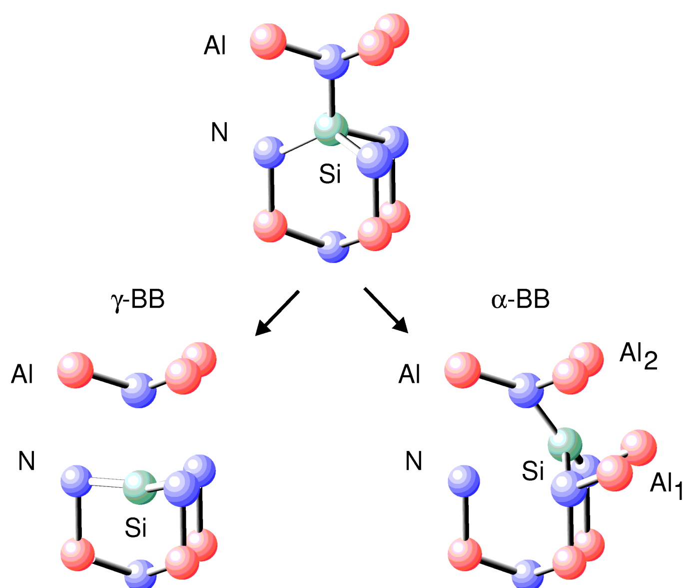

Figure 11.2: Structural relaxation of the Si donor in AlN into the DX-site. Due to the wurtzite structure two inequivalent relaxed sites are possible.

in c-axis (γ-BB) direction or in a-axis (α-BB) direction is broken. Up to now it is not clear which site is favoured [Bog97, Par97]. Since the DX formation reaction leads to a self-compensation of the Si donor, it is of great fundamental as well as practical interest to check whether a similar reaction occurs in AlGaN alloys with high Al content. But even in very low Al containing AlGaAs, where the substitutional donor is the ground state, it has been shown that the Si DX-center, which is resonant with the conduction band in these alloys, influences the transport properties [Kir88, Moo92], e. g. current noise.

So far, for Al-rich AlGaN only theoretical work about the Si lattice relaxation exists. However, the theoretical predictions are contradictory: While Park and Chadi [Par97] and Boguslawski and Bernholc [Bog97] have predicted that the DX-state is the stable configuration for Si in AlN, van de Walle [Wal98] has argued that Si always remains a shallow effective mass donor over the whole composition range. In the case of oxygen in AlGaN alloys, high pressure experiments on GaN as well as measurements of spectrally resolved and persistent photoconductivity (PPC) in AlGaN have shown that for Al contents $x \geq 0.35$ this dopant exhibits a DX-like behaviour [Wet97, Clu98]. Concerning the group III nitrides, high pressure experiments and PPC experiments in $Al_{0.6}Ga_{0.4}N$ have pointed towards a localized deep state of Si [Ski99]. However, the PPC observed at ambient pressures in these samples is very small and no spectral photoionisation threshold was reported. To investigate a possible DX-behaviour in AlGaN, the Si donor in AlGaN samples with high Al content has been studied using different techniques. Various kinds of dark and photoconductivity measurements revealed the optical threshold, the persistent photoconductivity and the capture barrier. EPR measurements evidenced that indeed the diamagnetic DX^- is the stable ground state. Finally noise experiments gave additional information about the emission kinetics of the DX state.

The experiments in this chapter have been carried out on the samples with the parameters listed in Table 11.2

11.1 Photo and dark conductivity

Assuming a normal shallow donor character for Si in AlN, one would expect infrared absorption and photoconductivity at photon energies around 320 meV. However, such a behaviour was not observed. Instead, as shown in Fig. 11.3, after cooling the sample to 20K in the dark, there is a strong photoconductivity threshold at about 1.4 eV. This again is in discrepancy to the effective mass model. The photocurrent, once excited, persists after switching off the light at as much as eight orders of magnitude above the dark current. The full symbols in Fig. 11.3 represent the spectrally resolved photoconductivity after cooling down the sample in the dark. The full lines are the spectra recorded after the first one without heating the sample in the meantime. These spectra show the large persistent photoconductivity. A similar behaviour is observed for $Al_{0.75}Ga_{0.25}N$:Si and $Al_{0.68}Ga_{0.32}N$:Si, however, the slope of the rising part (1 eV $\leq h\nu \leq$ 2 eV) is not as steep as for the pure AlN. For comparison, a PC spectrum measured at 60K of nominally undoped AlN is also shown in Fig. 11.3 (dashed line). No PPC can be seen. Moreover this undoped sample, below 50K, shows no photoconductivity at all. Since oxygen impurities are present in similar concentrations in both samples, the absence of a photoionisation threshold in nominally undoped AlN shows that the $DX-$like behaviour observed in AlN:Si is indeed due to Si incorporation.

The temperature dependent conductivity of different AlGaN:Si alloys are shown in Fig. 11.4. Upon cooling down the AlN sample from room temperature to 130K in the dark, an activated behaviour with the already mentioned activation energy of 320 meV is observed (c.f. Fig. 11.1). At 20K, the samples have become highly resistive. Illumination with light at 550 nm increases the conductivity by many orders of magnitude. Subsequently heating of the sample to 45K again in the dark slightly increases the conductivity. A further increase in

Sample		Nom. [Si] (cm^{-3})	N_D^{C-V} (cm^{-3})	Thickness μm
AlN	060798	3×10^{19}	n.a.[a]	1.5
$Al_{0.75}Ga_{0.25}N$	100497	1×10^{19}	n.a.[a]	1.5
$Al_{0.68}Ga_{0.32}N$	240699		1.2×10^{18}	1
$Al_{0.28}Ga_{0.72}N$	050398		1×10^{19}	1

[a] not available due to the lack of rectifying contacts.

Table 11.2: Parameters of the samples investigated.

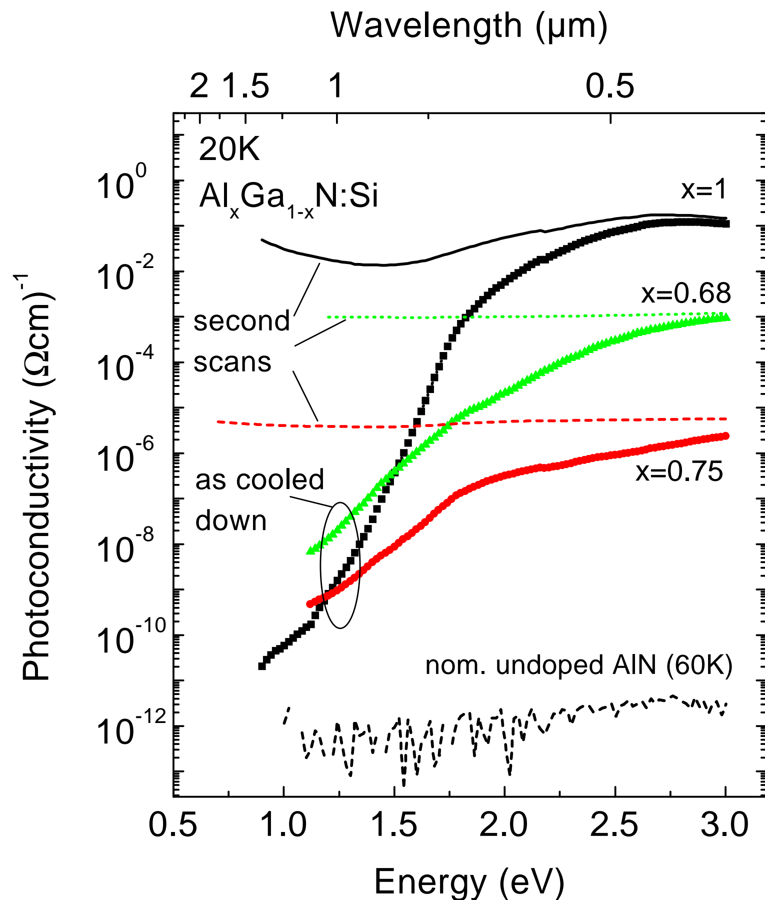

Figure 11.3: Spectrally resolved photoconductivity of different AlGaN alloys. The symbol graphs show a first scan after cooling the samples in the dark, the line graphs are the second scans. As a reference, the PC of a nominally undoped AlN sample is also shown (lowest graph).

temperature leads to quenching of the persistent photoconductivity. From 160 K on upwards, the normal activated behaviour is restored. This behaviour is similar for the samples with Al mole fraction x=0.75 and x=0.68. However, the effect of persistent photoconductivity is not as strong as for the AlN and the quenching of the PPC sets in at higher temperatures. The $Al_{0.28}Ga_{0.72}N$:Si however, behaves completely different. Here, hopping processes dominate the conduction slightly below room temperature down to 20 K. The conductivity is hardly affected by light, which shows that at this Al content no metastability of the Si donor occurs.

11.2 EPR measurements

Persistent photoconductivity itself is no prove for a DX state. Macroscopic barriers like dislocations and small capture cross sections due to coulombic repulsion can also cause PPC [Cra68, Lan92]. Indeed, PPC phenomena are also reported in pure GaN and AlGaN alloys

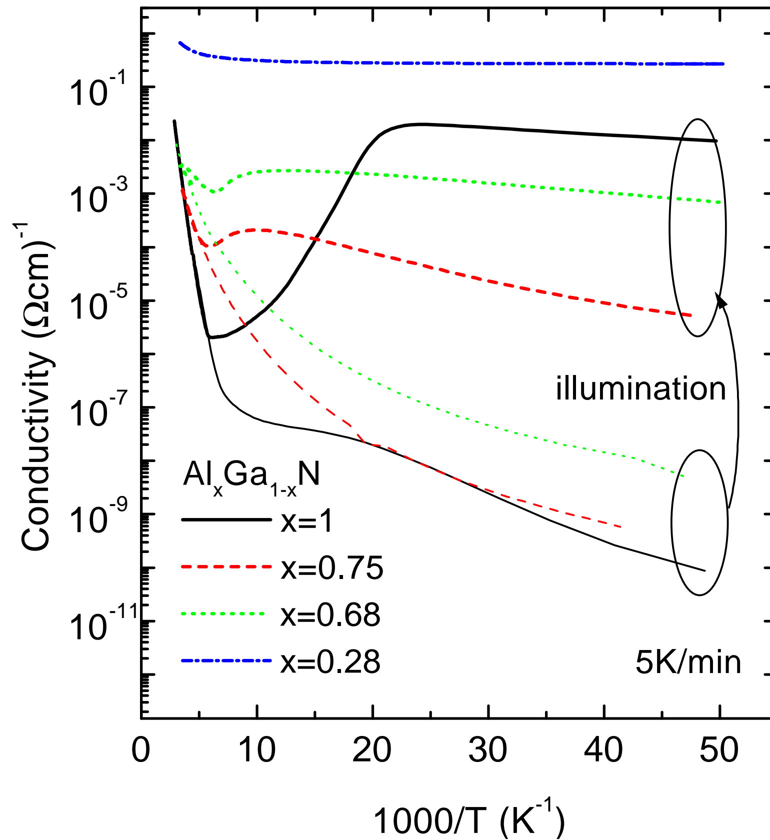

Figure 11.4: Temperature dependent dark conductivity of various AlGaN alloys. The thin lines are the cool down data, while the thick lines represent the heat up data, after the samples were illuminated at 20 K for 60 sec with 550 nm light.

with low Al content [Hir97, Li97]. Therefore EPR experiments are essential to prove the DX-nature of the defects responsible for PPC in AlGaN.

EPR experiments have been performed using a standard X-band EPR spectrometer with a TE_{102} microwave cavity. For g-factor calibration, DPPH was used. A detailed description of the spectrometer and the spin resonance technique is given in [Bay00a]

In AlN:Si neither at room temperature nor after cooling down to 4 K, an EPR signal can be detected at a level of 10^{16} spins/cm^3 per G line width. After illumination, a strong persistent resonance with an isotropic g-factor of 1.9885 ± 0.0001 appears (Fig. 11.5), while in GaN anisotropic donor resonances are observed [Car93]. Using different edge filters to cut off the high energy end of the lamp spectrum, it was confirmed that the spin density reveals the same dependence on photon energy as the photoconductivity. The signal shown in Fig. 11.5 was recorded at microwave powers of 16 μW, since at higher powers the line shape becomes increasingly asymmetric due to electron spin to nuclear spin cross relaxation [Den96]. The line width ΔH_{pp} decreases with increasing temperature, reaching a minimum

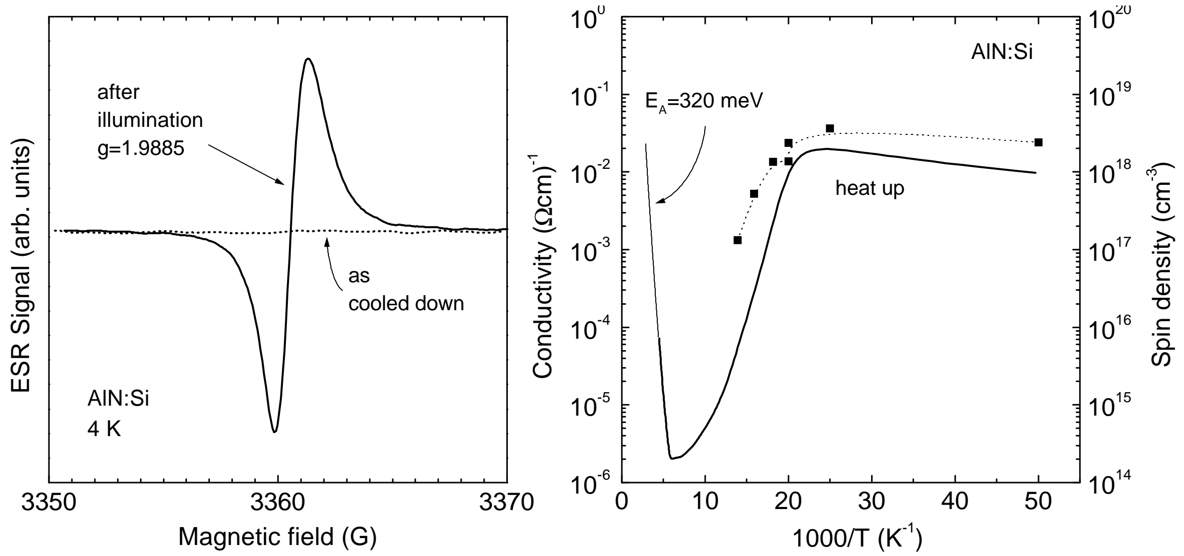

Figure 11.5: Left : EPR spectrum of AlN:Si after illumination. Right : Temperature dependent spin density after illumination of AlN:Si, as determined by EPR experiments (symbols). In addition the conductivity is shown (solid line).

of $\Delta H_{pp} = 1$ G at 30 K [Bay00a]. This is consistent with the resonance being due to an impurity band rather than due to electrons in the conduction band. In an impurity band exchange interaction leads to increased averaging of inhomogeneous hyperfine broadening with temperature, as observed for the residual donor in GaN [Car93]. The temperature dependence of the spin density in comparison with the conductivity after illumination at low temperature is shown in Fig. 11.5 (full symbols). For better comparison with the conductivity data, the same logarithmic scale is used. The spin density - as well as the conductivity - increases up to 45 K and then quickly drops below the detection limit. A maximum spin density of $3 \times 10^{18}\text{cm}^{-3}$ is observed at 45 K. If these spins were due to mobile electrons in the conduction band, a strong free carrier absorption should be observable. However, FTIR measurements at low temperatures failed to detect such an absorption. Furthermore, assuming that the persistent photoconductivity is caused by the persistent electrons detected in EPR, we obtain a mobility of only 10^{-2} cm^2/Vs. Both observations, namely the missing free carrier absorption and the low mobility support the notion that the charge carriers observed in EPR are due to a partially occupied donor impurity band. Furthermore, the measured spin density is at the limit for the Mott metal-insulator transition for Si in AlN as calculated in Fig. 2.1. The question whether these donor states are deep rather than shallow effective mass-like states can be addressed by examining the observed g-factor in detail. Based on a five band $k \cdot p$ model in the quasi-cubic approximation, the g-factors of shallow donors in GaN and AlGaN alloys with Al contents below 0.3 have been derived previously [Car93, Car97, Cha76]. Extending these calculations to higher Al contents and using the results of recent band structure calculations as well as experimental results for bandgap, spin-orbit splitting and electron effective mass,

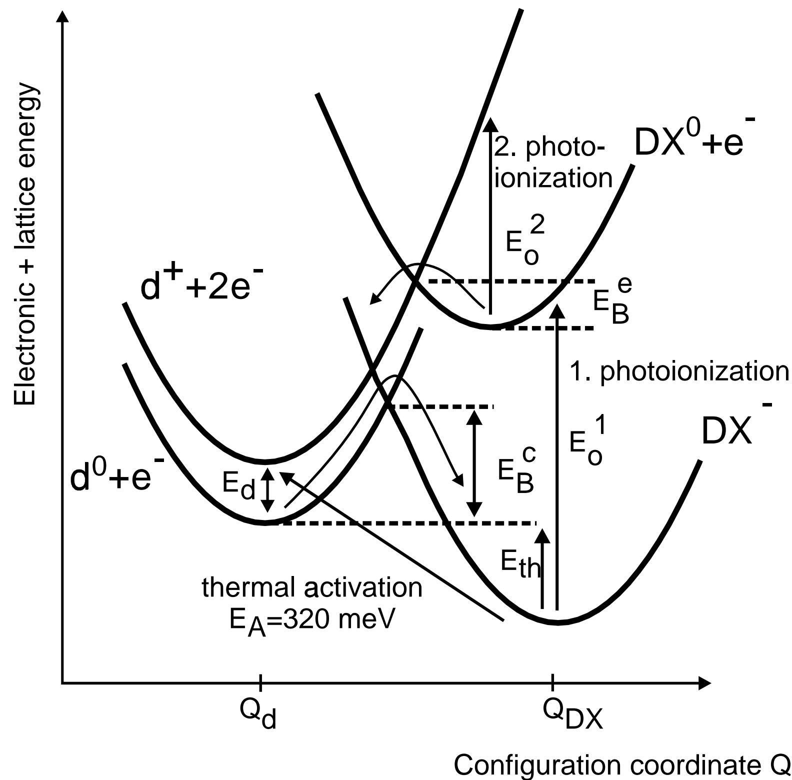

Figure 11.6: Configuration coordinate diagram of the Si DX-center in AlGaN.

the experimentally observed g-factor in AlN is found to be fully consistent with an effective mass donor rather than a deep state [Maj97, Kna97]. Details about the calculation are given in [Bay00b].

11.3 Microscopic model

As a summary of the experimental results, we can state the following: (1) The thermal activation energy of the conductivity of 320 meV in n-type AlN is due to silicon incorporation. (2) At low temperatures a photoconductivity threshold exists at about 1.4 eV photon energy. (3) The photoconductivity persists after switching off the light. (4) After cooling in the dark no EPR-signal can be seen. (5) Upon illumination an EPR signal caused by electrons bound to a shallow effective mass state is found. (6) The EPR signal as well as the persistent photoconductivity vanish above 60K.

All of these results can be well explained in terms of the DX model sketched in Fig. 11.6. The lowest parabola represents the DX^- state, which is occupied by two electrons. This state has undergone a large lattice relaxation (cf. Fig. 11.2) and is the stable ground

state. The parabola above this ground state symbolizes the thermodynamically metastable DX^0 state plus one electron in the conduction band. The lower left parabola shows the substitutional – also metastable – neutral shallow donor d^0 of the Si atom, the upper left parabola represents the ionised d^+ state, both with one and two electrons in the conduction band, respectively.

Thermally, the DX^- state can emit electrons directly into the conduction band, which is responsible for the 320 meV activation energy and is the energy separation between the two parabola $DX^-$and d^+ (item 1). Optical transitions, however, must be vertical in the configuration coordinate diagram and therefore the photoconductivity threshold is well above 320 meV (item 2). After photoionisation of the DX^- into DX^0 a second photoionisation or thermal emission process $DX^0 \rightarrow d^+ + e^-$ takes place. Such a two step photoionisation process has already been observed by Dobaczewski and Kaczor [Dob91] for Te DX-centers in AlGaAs, and has been shown to lead to a markedly non-exponential time dependence. At low temperatures, the d^+ state will immediately capture a free electron and thereby reform the metastable substitutional shallow donor d^0. All together, the photoionisation process can be written as

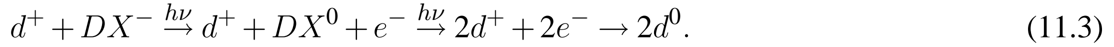

$$d^+ + DX^- \overset{h\nu}{\rightarrow} d^+ + DX^0 + e^- \overset{h\nu}{\rightarrow} 2d^+ + 2e^- \rightarrow 2d^0. \tag{11.3}$$

This reaction corresponds to an optical excitation out of the stable DX^- ground state into the metastable d^0 state. This state is separated from the DX^- state by the energy barrier E_B^c which at sufficiently low temperatures prevents the d^0 to undergo the DX-formation reaction (11.2) and thereby to return back to equilibrium. The observed persistent photoconductivity is believed to arise from hopping conduction in the donor band of the d^0 in accordance with the temperature dependence of the EPR line shape and doping level. In addition, the extremely low mobility strongly points towards transport not taking place in the conduction band. The photoconductivity is persistent because of the energy barrier E_B^c between d^0 and DX^- (item 3). Although this barrier has not only an electronic part, but also an ionic one since a lattice reconstruction must take place during the $d^0 \rightarrow DX^-$ transition, we may consider this barrier – from an electronic point of view – as a capture barrier for electrons. When cooling the sample slowly in the dark, the system remains in its ground state, where DX^- and d^+ are occupied according to Eq. (11.2). Neither one of those two states is paramagnetic and therefore no EPR signal can be detected (item 4). In contrast, a donor with 320 meV depth would not be ionised at low temperatures, i. e. an unpaired electron would be at the donor state, and should therefore give rise to an EPR signal. Illumination will turn the d^+ and DX^- states into two d^0 states according to Eq. (11.3), which cannot decay back because of the energy barrier separating the substitutional and DX-configurations. The d^0 state gives rise to the observed EPR signal (item 5) and the persistent photoconductivity. When the thermal energy is high enough to overcome the barrier, the equilibrium (i.e. DX^- and d^+)

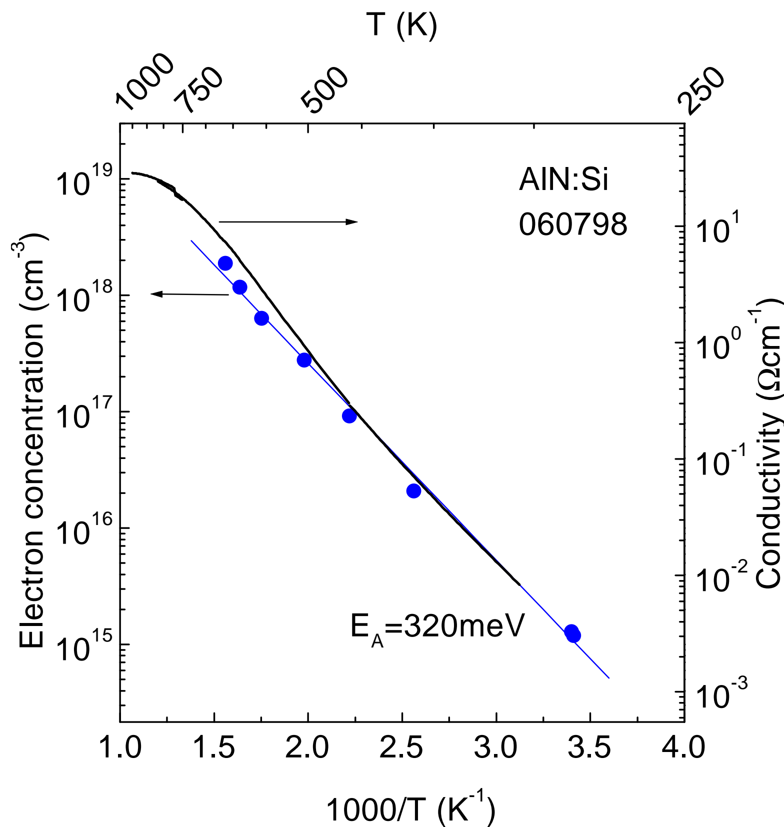

Figure 11.7: Temperature dependent Hall (circles) and conductivity measurements. For comparison the same scale for both measurements has been used.

is restored and both, the PPC and EPR signal vanish (item 6).

Based on the experimental results reasonable characteristic energies for the configuration diagram in Fig. 11.6 can be provided. E_d, which would be the ionisation energy of the shallow effective mass donor, can be estimated using the hydrogen model (11.1) which results in $E_d = 60$ meV, where $m^* = 0.33$ has been used [Maj97]. As will be shown in Sec. 11.4.1, the energy barrier between d^0 and DX^- is 80 ± 40 meV. The activation energy of the conductivity at temperatures above 160 K, $E_A = 320$ meV, is given by the sum of E_d and E_{th}. Using the effective mass value for E_d results in 260 meV for E_{th}. For the optical transition energies E_o^1 and E_o^2 it should be noted that the optical threshold is determined by the larger one of these two energies. Therefore an unambiguous assignment is not possible at this point. A further discussion is provided in Sec. 11.4.1.

Although this model seems to be quite consistent, some open questions remain. First, the detected spin density by EPR is about a factor of ten below the nominal doping density. To check whether all Si atoms are electrically active, high temperature Hall and conductivity measurements have been performed. The results are shown in Fig. 11.7. Since the limited temperature range of the Hall setup was not sufficient to reach carrier exhaustion, conductivity measurements have been carried out up to temperatures, were the conductivity becomes

constant with temperature. To estimate the order of magnitude of free electrons at these temperatures, the conductivity data have been normalised to the electron concentration at room temperature as determined by Hall effect. This leads to approximately 1×10^{19} cm^{-3} electrically active Si dopants, indicating that indeed all Si atoms act as dopants. The discrepancy between the number of spins detected by EPR and the number Si dopants is attributed to doping inhomogeneity of the sample. In regions with higher doping density, the Mott metal-insulator transition has taken place leading to very short spin relaxation times which in turn broadens the resonance line width to an extent that these spins cannot be detected by EPR. Therefore the spins observed are most likely in regions with low Si doping density. The identical photoionisation threshold and temperature dependence of the PPC and EPR shows however, that the $DX-$like behaviour is identical in low and high Si doped AlN.

In the AlGaAs system, Si undergoes the DX relaxation for Al contents larger than 23 %. For the oxygen donor in AlGaN this transition has been determined by pressure dependent Raman measurements at an Al content of 40 % [Wet97]. Wetzel *et al.* also investigated Si doped samples, but the maximum applied pressure there, which corresponds to an Al content of 56 %, was not sufficient to stabilize the Si DX state. In the present work the Si DX-state was found to appear for Al mole fraction $x \geq 0.68$, therefore we can specify the DX transition of Si in $Al_xGa_{1-x}N$ to occur in the range of Al content

$$0.56 \leq x \leq 0.68 \tag{11.4}$$

11.4 Dynamics

So far, only steady state situations – either after illumination or in the dark – have been analysed. From the measurement of the decay and rise dynamics of the PC, further information about the configuration coordinate diagram can be obtained. The decay of the photoconductivity after switching off the light provides information about the capture barrier E_B^c, the rise of the PC after switching on the light provides insight into the intermediate DX^0 configuration. These are all measurements at low temperatures. At high temperatures, where all thermally dominated time constants have become much smaller, noise measurements are a good way to measure the generation/recombination dynamics of the system.

11.4.1 Conductivity

PC rise

Assuming first order kinetics of the photoexcitation, one would expect an exponential rise of the photoconductivity as the solution of Eq. (3.19). However, the actual photocurrent

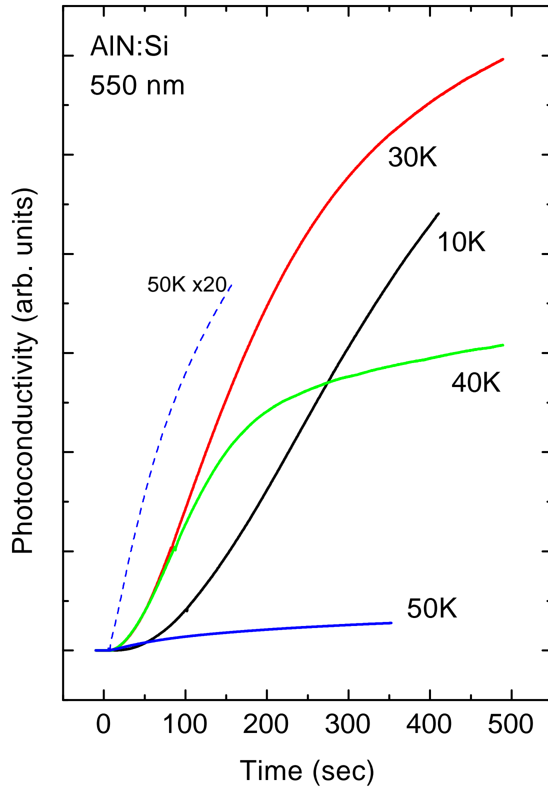

Figure 11.8: Photoconductivity transients of AlN:Si for different temperatures after cooling down in the dark. The light is switched on at $t = 0$.

transients exhibit a significant deviation from an exponential behaviour (cf. Fig. 11.8). Especially at low temperatures and short times after switching on the light, one can see a quadratic rise of the PC instead of a linear time dependence. With increasing temperature the linear part becomes more dominant and the onset of saturation is visible within the observation time. At 50 K a strong decrease of the steady state PC is observed, the quadratic part has vanished completely (cf. magnified plot). Because of the two step photoionisation process which a DX state undergoes, first order kinetics are not appropriate to describe the temporal evolution of the electron density. Therefore a model based on rate equations for the different states has been developed. Fig. 11.9a visualizes the four states and all transition rates occuring in the photoionisation process. e_{if} stands for emission and c_{if} for capture processes from state i to state f. The superscripts o and th denote optical and thermal transitions, respectively. However, the system as sketched in Fig. 11.9a corresponds to a system of four coupled differential equations, which cannot be solved anymore analytically. Therefore the following assumptions have been made. Once the d^+ state is created, it will capture immediately an electron and become d^0 at the low temperatures considered here, i. e. c_{34} is much larger than all the other rates. Therefore the two states d^+ and d^0 are considered as a single state d, with the appropriate emission and capture rates (cf. Fig. 11.9b). The system of differential equations describing the simplified model is given by

$$\frac{\partial n_1(t)}{\partial t} = -e^o_{12} n_1(t) + c_{21} n_2(t) + c_{31} n_3(t) \qquad (11.5)$$

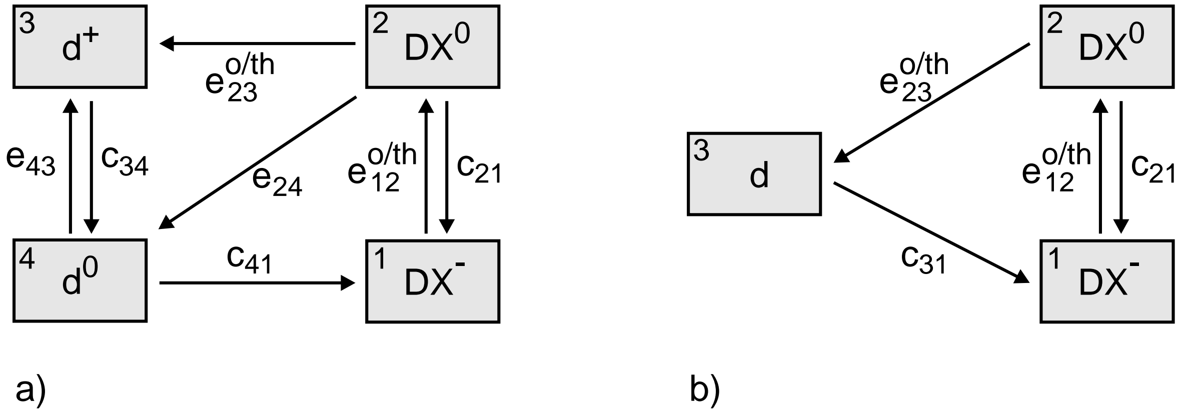

Figure 11.9: a) Schematic of the states and transition rates involved in transitions between the d and DX states. b) Simplified model

$$
\begin{aligned}
\frac{\partial n_2(t)}{\partial t} &= -(e^o_{23}+e^{th}_{23}+c_{21})n_2(t)+e^o_{12}n_1(t) \\
n_3(t) &= N_{DX}-n_1(t)-n_2(t)
\end{aligned}
$$

where $n_i(t)$ is the time dependent electron concentration in state i and N_{DX} is the total density of DX centers. At low temperatures the conductivity is proportional to the number of electrons in state d ($n_3(t)$). After cooling down the sample in the dark, the states DX^0 (2) and d (3) are empty, while the DX^- (1) is occupied. Therefore the initial conditions for the rising photoconductivity transient are

$$
n_1(0)=N_{DX}, \qquad n_2(0)=0 \qquad \text{and} \qquad n_3(0)=0. \tag{11.6}
$$

With this set of equations, the photoconductivity transients at different temperatures can be fitted. The thermal capture rate c_{31} is directly accessible experimentally via the decay time constants of the PPC as determined in the following Section. The optical emission rates e^o_{12} and e^o_{23} are set once and kept fixed for all temperatures, since the photon flux has been kept constant during the set of measurements. Reasonable fits were obtained using the values listed in Tab. 11.3. The fits are shown in Fig. 11.10 The fact that the transition rate from the excited DX^0 state back into the DX^- ground state is the smallest of all rates, indicates that indeed the DX^0 state is the highest lying one. Otherwise it would be very easy to capture an electron and relax back in the to DX^- state. This however is not possible if the DX^0 state is above the d state, in this case it is favourable to emit thermally or optically a second electron. The significant temperature dependence of this process (e^{th}_{23}) indicates that there is also a barrier – labeled E^e_B in Fig. 11.6 – which has to be surmounted by the electrons. A fit to the emission rate yields a barrier height of roughly 5 meV.

Although the agreement between the fits and the experimental transients is rather good, this model should not be stressed to much, since calculated carrier densities are compared

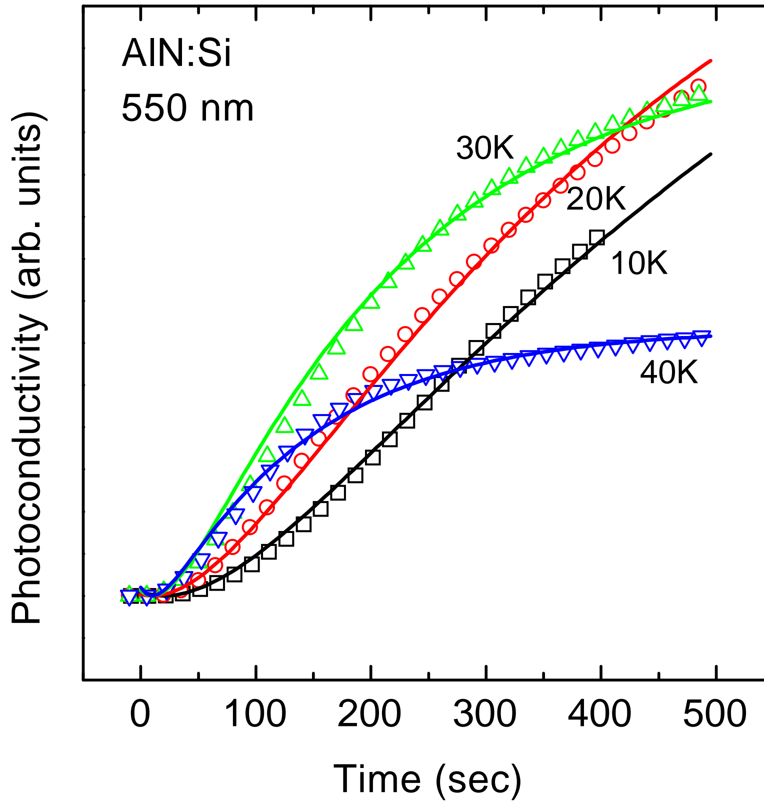

Figure 11.10: Rising photoconductivity transients (open symbols) and fits after Eq. (11.5) (solid lines). The fitted transition rates are listed in Tab. 11.3.

	Rate (sec^{-1})				
Temperature	e^o_{12}	e^o_{23}	e^{th}_{23}	c_{21}	c_{31}
10 K	0.0001	0.0003	0.0009	8×10^{-5}	0.012
20 K	0.0001	0.0003	0.0017	8×10^{-5}	0.014
30 K	0.0001	0.0003	0.0045	8×10^{-5}	0.033
40 K	0.0001	0.0003	0.007	8×10^{-5}	0.066

Table 11.3: Transition rates used for fitting the temperature dependent rising transient of the photoconductivity in AlN:Si.

with the measured conductivity. Therefore the mobility has not been taken into account, which may be a very crude approximation. Since we have assumed hopping conduction between the d^0 states, the mobility is expected to change strongly with d^0 density. This change in mobility will affect the time dependent conductivity. However, the main characteristics of the PC transients, namely the quadratic rise and the quenching with increasing temperature can be understood very well with the present model.

A drawback of the photoconductivity spectra shown in Sec. 11.1 is the fact that they do not represent the photoionisation cross section from which an exact optical threshold could be determined. Due to the persistence of the photoconductivity, the initial conditions, i. e.

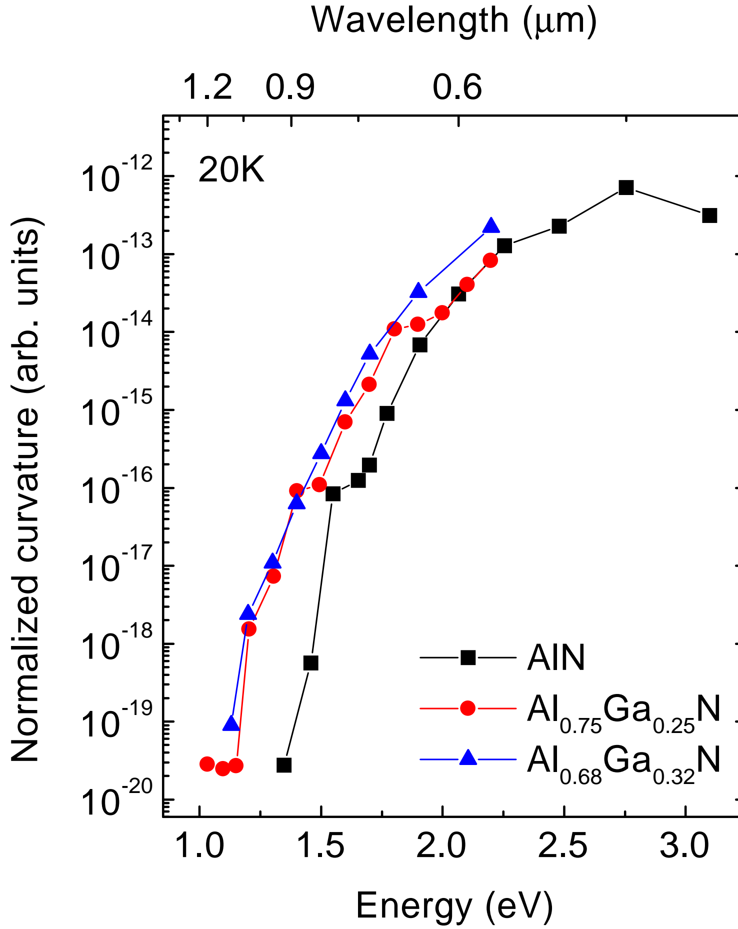

Figure 11.11: Curvature of the PC transients normalized to the photon flux for three AlGaN alloys. As shown in the text, the curvature is proportional to the photoemission rate.

the occupation of the different levels, are different at every point in the spectra. Therefore photoconductivity transients have been measured for different wavelengths at 20 K, each after having warmed up the sample to temperatures above the PPC quenching. As already mentioned, the slope of the PC transients at $t = 0$ vanishes due to the quadratic rise of the PC. Therefore the method of evaluating the initial slope to determine the photoionisation rate is unsuitable in this case. However, using the solution of (11.5), the second derivative with respect to the time, i. e. the curvature of the transient, is given by

$$\left.\frac{\partial^2 n_3(t)}{\partial t^2}\right|_{t=0} \propto (e^o_{23} + e^{th}_{23})e^o_{12} \overset{e^o_{23} \ll e^{th}_{23}}{\approx} e^{th}_{23}e^o_{12}. \quad (11.7)$$

Keeping in mind that for an optical emission rate the relation $e^o = \sigma_o \Phi$ holds, we thus have a method at hand, which relates the curvature of the PC transient to the photoionisation cross section.

The curvature of the PC transients normalized to the photon flux for the three AlGaN samples is shown in Fig. 11.11. To fit a theoretical photoionisation cross section to the data, the formula for a phonon broadened photoionisation cross section in the strong coupling

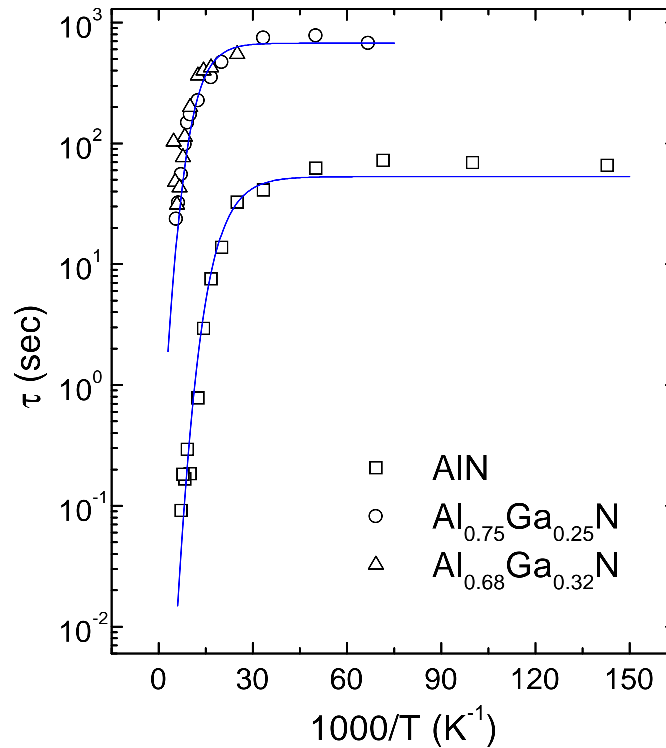

Figure 11.12: Temperature dependent PPC decay time constants for three AlGaN alloys. The solid lines are fits according to the MPE model.

limit (large Franck-Condon shift E_{FC}, here $\approx$ 1.2 eV) Eq. (7.7) has to be used [Cha81]. However, such a fit cannot be satisfactory, since it involves only one level, while in the DX photoionisation two levels are involved. Additionally, the rising flank in Fig. 11.11 is much too flat to be caused by thermal broadening at 20 K. However, it seems more likely that effects of piezoelectric fields and internal strain, rather than the two step process broaden the absorption threshold. Because of this complication no attempt has been made to fit the data. Broadening due to alloy disorder can be ruled out, since the shape of the AlN sample is similar to the one of the alloys. Therefore only the threshold energies of the photoionisation of 1.4 eV for AlN and 1.1 eV for the 68% and 75% Al containing alloys can be given. Here, a clear trend towards decreasing Franck-Condon shift (AlN: 1.1 eV; $Al_{0.75}Ga_{0.25}N$: 0.9 eV) with decreasing Al content can be seen.

PPC decay

Although the photocurrent is called persistent, it decays with a large time constant after switching off the light. The temperature dependence of this time constant provides information about the capture barrier. The decay time constant τ is related via $1/\tau = v_{th}\sigma n$ to

the capture cross section σ and the electron density n. Unfortunately n and v_{th} cannot be estimated in this case with sufficient accuracy. The electron density is not known within a factor of 10 plus it is supposed to be inhomogeneous over the sample. The thermal velocity is also difficult to estimate, since at the low temperatures hopping conduction has to be taken into account, where the simple relation $v_{th} = \sqrt{2kT/m^*}$ does not hold anymore. Furthermore, the spontaneous polarization especially in AlN gives rise to a high electric field in the layer [Amb99]. Photogenerated electrons will therefore be pushed to the top or bottom of the layer, resulting in an inhomogeneous depth profile. Therefore, in the further discussion, we only deal with the time constant τ, which is a directly observable value. Where DLTS is not applicable – like in this case due to the high doping level – this method is common to determine capture barriers [Nel77].

The temperature dependence of the PPC decay time constants for the three AlGaN alloys are shown in Fig. 11.12. They are obtained by fitting a stretched exponential function to the PPC decay currents. In the low temperature range ($1000/T > 30$), the time constant is not temperature dependent, whereas for higher temperatures, it becomes thermally activated. This behaviour can be very well understood using the multi phonon emission (MPE) model [Hen77]. Within this model the capture cross section is expressed by [Eng70]

$$\sigma = A\sqrt{4\pi E_{FC}kT^*}\,\mathrm{e}^{-\frac{E_B}{kT^*}} \tag{11.8}$$

where

$$kT^* = \frac{\hbar\Omega}{2}\coth\frac{\hbar\Omega}{2kT} \tag{11.9}$$

is the effective temperature. $E_{FC} = S\hbar\Omega$ is the Franck-Condon shift and E_B the barrier height. The matrix element A is assumed to be temperature independent. This expression results from the fact that non radiative transitions involve the overlap of vibronic states at the same energy. This overlap is described by the line shape function for optical transition of phonon assisted absorption. Since we are interested in the overlap at the same energy, the line shape function for $h\nu = 0$ has to be used. The line shape function was discussed in Sec. 7.1. In Eq. (11.8), however, the strong coupling limit was used, where the line shape function is a Gaussian function [Lax53]. At high temperatures, where $T = T^*$, Eq. (11.8) shows the classical thermally activated capture. At low temperatures, where $kT^* = \hbar\Omega/2$, the zero point vibrations play the role of temperature. Thus, the capture cross section will no longer be temperature dependent.

A fit of the MPE model to the data is shown as solid lines in Fig. 11.12. The fit parameters, which are within the errors the same for all three samples, are given in the following Table

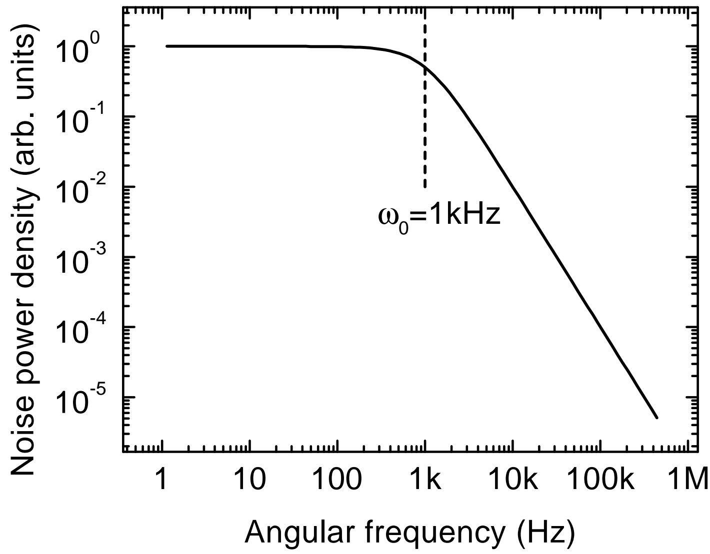

Figure 11.13: Noise power density of a generation–recombination noise with a characteristic time constant $T_0 = 10^{-3}$ sec.

Barrier height E_B (meV)	Phonon energy $\hbar\Omega$ (meV)	Franck-Condon shift E_{FC} (eV)
80 ± 40	13 ± 5	1.3 ± 0.1

The phonon energies that result from the fits are rather low compared with the results obtained in AlGaAs. Here the best fists were obtained for optical phonons (34 meV) [Lan92] and acoustic phonons ($\approx$ 10 meV) (e. g. EL2 [Mar77]). The comparable maxima in the phonon DOS of AlN are in the range of 35 meV (acoustic branch) and 95 meV (optical branch) [Nip98]. However, it is not possible to explain the PPC decay time constants with such high photon energies. Even for Si DX centers in GaAs phonon energies around 10 meV have been used [Nel77, Lan77]. These low phonon energies are needed to make the zero point vibrations very weak and shift this regime to very low temperatures, where the DX features occur. This makes the capture cross section as low as 10^{-31} cm^{-2}. Such a low capture cross section can only occur in the case of centers with a large lattice relaxation, like the DX state. Due to this relaxation, the overlap between the wave functions of the relaxed and unrelaxed state is small and optical capture becomes impossible. Otherwise the capture cross section would not fall below 10^{-21} cm^{-2}, a typical value for optical capture [Lan92]. This is the reason why no photoluminescence from DX-centers is observed.

11.4.2 Noise

Noise in semiconductors due to charge carrier density fluctuations can provide information about generation–recombination dynamics of charge carriers and properties of the involved traps. However, purely thermal noise, whose noise power density $S(\omega)$ is frequency inde-

pendent [Zie86]

$$S = 4kTR, \tag{11.10}$$

is not suitable to characterise any physical properties of the sample other than the resistance. To observe noise associated with generation recombination processes of charge carriers, a current has to flow through the sample. The noise is caused by number or mobility fluctuations of free electrons around their mean value as determined by Fermi-Dirac statistics. The most simple system describing the fluctuations is a two-level system, where the electron can either occupy a band state and contribute to the current or be trapped at a defect site and hence does not participate at the current flow. It has been shown that in this case (generation–recombination or $g-r$ noise) the noise power density is given by [Mac54]

$$S(\omega) = \frac{1}{\pi}\frac{\sigma\tau}{(\sigma+\tau)^2}\frac{1/T_0}{\omega^2+1/T_0^2} \tag{11.11}$$

where σ and τ are the mean life times in the trapped and band state, respectively. T_0 is the characteristic time constant and is given by

$$\frac{1}{T_0} = \frac{1}{\sigma}+\frac{1}{\tau}. \tag{11.12}$$

The noise power at zero frequency is given by

$$S(0) = \frac{1}{\pi}\frac{(\sigma\tau)^2}{(\sigma+\tau)^3} \tag{11.13}$$

From this formula it is obvious that the noise power as well as the characteristic time constant are symmetric with respect to τ and σ. If the life times are significantly different, e. g. $\sigma \ll \tau$, then T_0 is dominated by the smaller time constant, here σ. This is to say that the state with shorter life time dominates the behaviour of the characteristic time constant T_0. A spectrum with $T_0 = 10^{-3}$ sec is shown in Fig. 11.13. The noise power is constant up to the inverse time constant T_0 and then drops as f^{-2}. However, such a clear $g-r$ noise spectrum is observed very rarely. In most cases, a $1/f$ spectral dependence of the noise is measured. The microscopic reason for this frequency behaviour is not clear up to now. One possible explanation is a superposition of several $g-r$ processes, which results in an approximate $1/f$ spectrum [Wei88].

Experimentally, a constant current is driven through the sample and the fluctuation of the voltage that drops over the sample due to the resistance fluctuations is analysed by a fast Fourier transform spectrometer (cf. Fig. 11.14). Thus, resistance fluctuations are probed. Details of the noise experiment are given in [Goe00]. A noise spectrum of the Si doped AlN

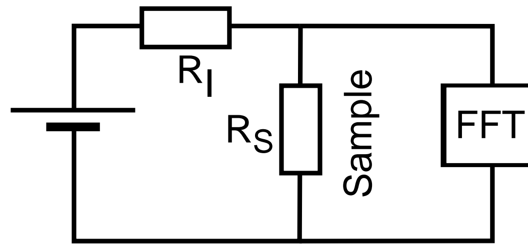

Figure 11.14: Setup for noise measurements. To get reliable measurements, $R_I \geq 10R_S$.

sample at two temperatures is shown in Fig. 11.15. The $g-r$ character of the spectra is slightly distorted by an additional $1/f$-noise, but the characteristic frequency of 600 Hz (319 K) and 4 kHz (368 K) can be clearly seen. Obviously, the characteristic frequency changes with temperature, i. e. the generation recombination time constant is temperature dependent. Additionally, the noise power level for frequencies smaller than the inverse time constant T_0 decreases with increasing temperature. To obtain a reliable measure of the $g-r$-noise power density, $S(\omega = 1/T_0)$ has been used. At this frequency the influence of the additional $1/f$ noise is minimal. From an ideal $g-r$ noise spectrum it follows that $S(\omega = 0) = 2S(\omega = 1/T_0)$. The Arrhenius plot of the extrapolated noise power at zero frequency $S(0)$ and the characteristic time constant T_0 is shown in Fig. 11.16. Obviously, the life times σ and τ are thermally activated. In order to interpret these data, the following assumptions are made

$$\begin{aligned} \sigma &= \sigma_0 \, \mathrm{e}^{E_\sigma/kT} \\ \tau &= \tau_0 \, \mathrm{e}^{E_\tau/kT}. \end{aligned} \tag{11.14}$$

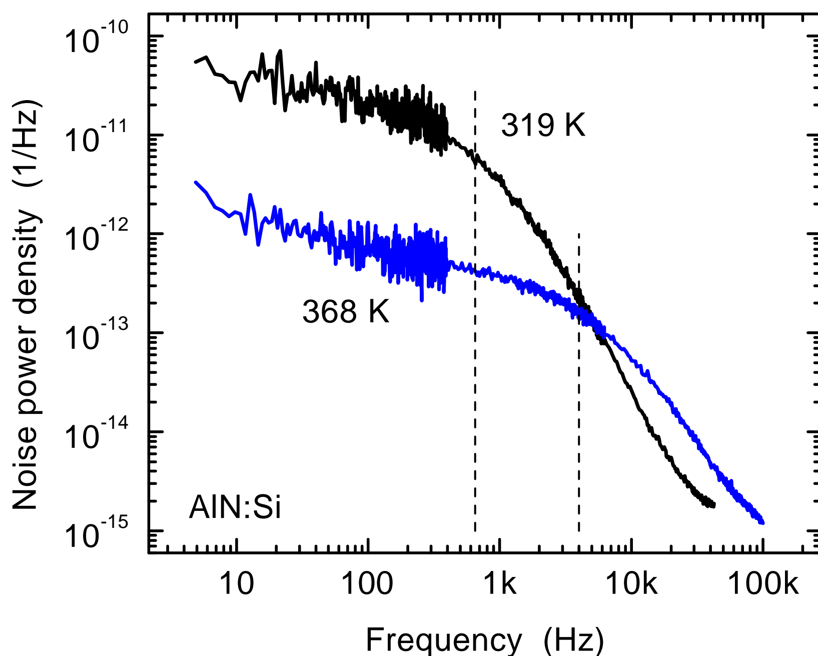

Figure 11.15: Spectral dependence of the current noise in Si:AlN for two temperatures. A clear temperature dependent shoulder can be seen, which is characteristic for a generation–recombination noise.

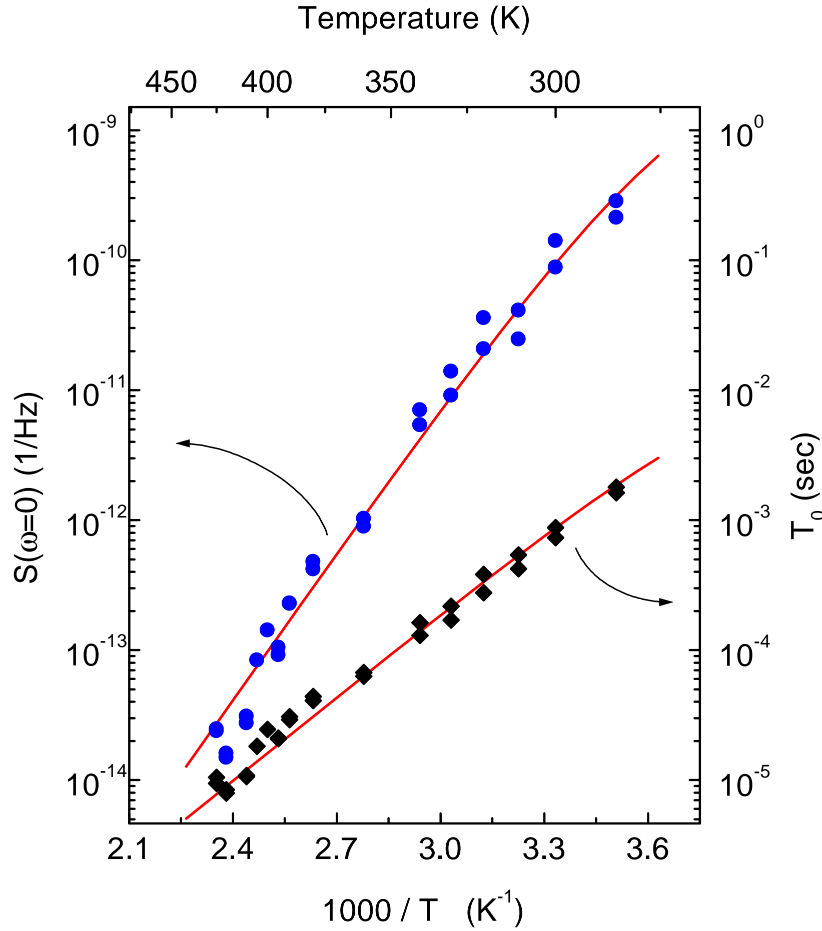

Figure 11.16: Temperature dependence of the characteristic time constant T_0 and the noise power at zero frequency $S(0)$ of the generation–recombination noise in Si:AlN. The solid lines are fits according to Eqs. (11.13) and (11.12).

Using such a thermally activated behaviour, a fit to $S(0)$ and T_0 in Eqs. (11.13) and (11.12), respectively, has four free parameters. However, using the model for the DX center as presented in Sec. 11.3 provides clues to the choice of the activation energies E_σ and E_τ. Unlike in conductivity or Hall experiments, where the energy difference E_A between initial (DX) and final (d^+) state is measured, the noise experiment is determined by the kinetics. Therefore, also the barrier E_B separating these states must be taken into account (cf. Fig. 11.6). Thus, choosing σ to be the time constant for emission, gives an activation energy $E_\sigma = E_A + E_B$. For the capture process only the barrier E_B has to be surmounted by the electrons and therefore this process is activated with $E_\tau = E_B$, the barrier energy.

For the initial guess of the prefactors in Eq. (11.14) it is instructive to look at the sign of the slope of $S(0)$ versus temperature. When $\sigma \ll \tau$, i. e. at high temperatures, we obtain

$$S(0) \overset{\sigma \ll \tau}{\cong} \frac{\sigma_0^2}{\tau_0}\, \mathrm{e}^{(2E_\sigma - E_\tau)/kT} \tag{11.15}$$

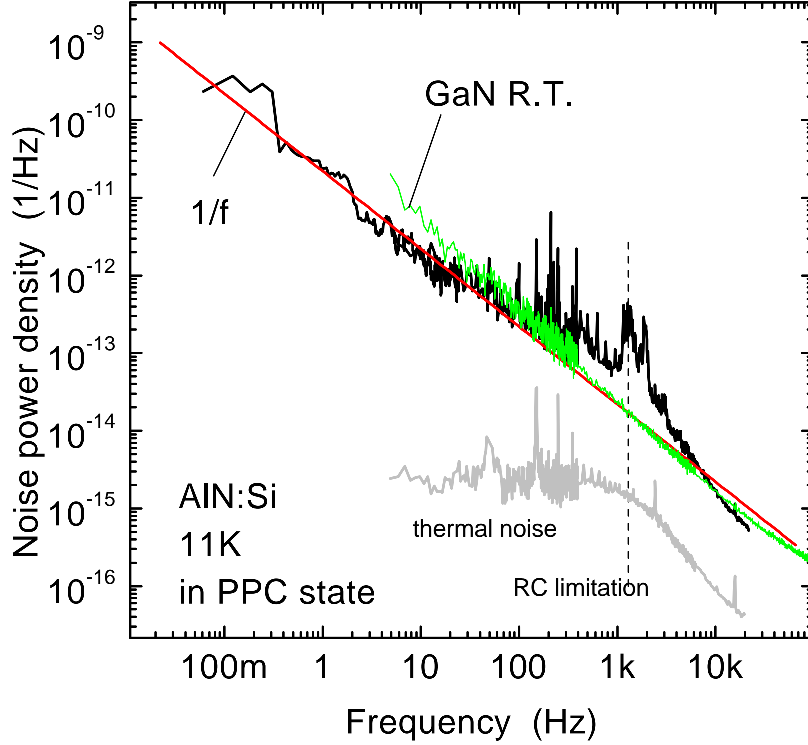

Figure 11.17: Noise spectrum of Si:AlN at 11 K in the PPC state. The DX states are emptied by photoionisation, the transport properties are dominated by shallow d states. For comparison the noise spectrum of pure GaN:Si at R.T. is also shown.

and therefore

$$\frac{\partial(\ln S(0))}{\partial 1/T} = C_1(2E_\sigma - E\tau), \tag{11.16}$$

where C_1 is positive for all temperatures. With the assignment for the activation energies as made above ($E_\sigma = E_A + E_B$; $E_\tau = E_B$), it follows that $E_\sigma > E_\tau$ and therefore $\partial(\ln S(0))/\partial(1/T) < 0$ according to (11.16). This is the case for AlN:Si in the temperature range investigated here. To fulfill the condition $\sigma \ll \tau$ although $E_\sigma > E_\tau$, the prefactor τ_0 has to be much bigger than σ_0. A fit to the data leads to the following values

Parameter	Value	
E_σ	420	meV
E_τ	100	meV
σ_0	1	arb. units
τ_0	2×10^6	arb. units

As already stated above, E_τ corresponds to the barrier height. The value obtained here (100 meV) is in good agreement with the one extracted from the PPC decay time constants (80 meV). Subtracting the barrier height from E_σ yields the activation energy for the dark conductivity $E_A = 320$ meV, in perfect agreement with the experimental result.

The noise measurements above room temperature as presented above gave additional evidence of a capture barrier and have demonstrated its influence on the transport properties even at ambient temperatures, where no persistent effects like PPC are observed. Another measurement to confirm that the noise at room temperature is indeed caused by the DX level, is a noise experiment at low temperature (e. g. 11 K) in the persistent photoconductivity state.[1] In this case the DX levels have been emptied by photoexcitation and the substitutional donors dominate the current transport characteristics, since the energy barrier prevents them from relaxing back to the DX state. Since no DX $g-r$ noise is possible anymore, one would expect a $1/f$ noise as it is observed typically in Si doped GaN where no DX behaviour of Si is detected. As it is shown in Fig. 11.17 the noise power depends on frequency as $f^{-\alpha}$ where $\alpha \approx 1$. This is compatible with the $1/f$ behaviour and therefore proves again the ability of optically transferring electrons from the DX state to a shallow donor state.

[1] However, the conductance of the sample in the PPC state is still so low that the resulting RC time constant caused by parasitic capacitances shifts the cut-off frequency to about 1 kHz (dashed line in Fig. 11.17).

CHAPTER 12

Summary and Outlook

In the context of this thesis, new results about defect properties in diamond and AlGaN alloys with high Al content have been obtained. The experimental techniques used were capacitance-voltage ($C-V$) profiling and conventional and optically induced Deep Level Transient Spectroscopy (DLTS and ODLTS). During the optimization of the $C-V$ measurement it turned out that it is necessary to use variable test frequencies of the $C-V$ measurement between 60 Hz and 10 kHz to account for the series resistance of the diodes and the emission rate of the shallow dopants. For this purpose a new $C-V$ detection unit consisting of a Lock-In amplifier, a pulse generator and a mixer was designed and built. For samples where the DLTS technique could not be applied due to the high resistance or the lack of rectifying contacts, use of spectrally resolved photoconductivity and related techniques has been made. Additionally, thermally activated dark conductivity and Hall measurements were used to further characterize the samples' transport properties. For all experiments, computer programs have been written to enable automatization of the measurements. For high temperature conductivity and annealing studies a heating stage has been built which allows the temperature to be varied between R.T. and 950 K with heating rates of up to 100 K/min.

$C-V$ profiling offers a possibility to determine dopant densities and built-in potentials of Schottky contacts. For the natural and synthetic diamonds investigated here, acceptor densities of 2×10^{16} cm^{-3} and built-in potentials of 1.7 V of Ag contacts were found. This method enabled also the demonstration of hydrogen passivation of the boron acceptor in diamond. The hydrogenation was performed in a DC remote plasma at 400 °C . The $C-V$ characteristics after passivation were interpreted based on a two layer model: a highly resistive layer where all boron acceptors have been passivated by hydrogen and the bulk layer, where the acceptor density remains unchanged. For this situation, the Poisson equation has been solved which enabled a fitting of the measured $C-V$ curves. From the fitting parameters, the passivation depth could be determined, which in turn was used to calculate the diffusivity of the hydrogen. A value of 4.7×10^{-13} cm^2/s at 400 °C was obtained.

Annealing the passivated Schottky diodes at 750 K showed a significant change of the $C-V$ profile. This could be modeled assuming a three layer model: a reactivated layer underneath the surface, then again a passivated region and finally the unpassivated bulk material. This was attributed to thermal release of the hydrogen from the boron acceptor with a subsequent drift in the electric field of the Schottky diode and a recapture by an unpassivated boron atom at the end of the depletion layer. Since there was a significant difference between unbiased and biased diodes, it was concluded that the diffusing hydrogen is positively charged.

ODLTS investigations of synthetic type IIb diamonds, homoepitaxial and heteroepitaxial boron doped CVD layers were carried out in the photon energy range between 0.6 eV and 3 eV. In all samples a defect absorption in the range 1.2 eV and 1.7 eV could be detected, which is most clearly pronounced in the homoepitaxial CVD sample. To explain the shape and especially the temperature dependence of the absorption in this sample, the photoionisation cross section has been calculated based on the model of lattice relaxation upon photoionisation. To this end calculations for the line shape function of phonon assisted transitions between the defect states have been combined with matrix elements for defect to band absorption. From the fit of the resulting photoionisation cross section to the experimental data, a trap energy of 1.28 eV above the valence band and a Franck-Condon shift of 0.16 eV could be extracted.

The ubiquity of this defect absorption stimulated ODLTS investigations of carbon ion implanted samples, to confirm the idea that this defect is an intrinsic one, involving vacancies and/or carbon interstitials. This proved to be true, as the defect density increased with increasing implantation dose. Additionally a second defect absorption in the range of 2.5 eV to 3 eV also increased. Not only the ODLTS spectra changed upon implantation, but also the $C-V$ characteristics changed significantly. This could again be modeled assuming a highly resistive, compensated layer due to radiation damage within the penetration depth of the carbon ions. Annealing studies of the diodes revealed a thermal quenching of the 1.28 eV defect at 550 K. From a fit to the annealing data, a migration energy of the involved species of 1.25 eV was calculated. This is in good agreement with data available in the literature for an interstitial migrating to and annihilating with a vacancy. However, certain aspects of the annealing behaviour of the $C-V$ curves are in contradiction with this model, therefore no complete microscopic model could be developed.

According to theory Li reveals shallow n-type doping properties on the interstitial lattice site. Therefore homoepitaxially grown, Li doped CVD diamond layers have been investigated by means of thermally activated dark- and spectrally resolved photoconductivity. The dark conductivity revealed only a slightly lower resistivity than a nitrogen doped Ib crystal, activation energies varied between 1.3 eV and 1 eV. Spectrally resolved photoconductivity together with photoconductivity excitation spectroscopy identified two new levels in the Li doped samples compared to the Ib substrate: one at 0.9 eV and a second level at 1.5 eV be-

low the conduction band. The first one can be metastably occupied by UV illumination and is bleached easily during a subsequent photoconductance measurement, resulting in a peak shaped excitation spectrum. A model is proposed, where Li in conjunction with another, probably lattice defect, introduces the mentioned levels and electrons are transferred from the 0.9 eV level into the 1.5 eV level.

Motivated by theoretical work, the doping behaviour of Si in AlGaN alloys with high Al content was studied. The activation energy of the dark conductivity increases from 20 meV (GaN) to 320 meV (AlN). The latter observation is in contradiction with the simple effective mass model which predicts an ionisation energy of 60 meV instead. Additionally, no photoconductivity at 320 meV was found, but a photoionisation threshold at about 1.4 eV at low temperatures could be detected. This photoconductance, once excited, was found to be persistent up to 60 K. Similar to the photoconductivity, no EPR signal could be detected after cooling down the sample, but a strong, also persistent EPR line with a g factor of 1.9885 appeared after illumination. All these facts were explained in terms of a Si DX state in AlN. Experiments on AlGaN alloys with 75 % and 68% Al content showed a similar behaviour. Based on this model, the photoconductivity transients were fitted by a rate equation model, which explained their main features, namely a quadratic rise of the photoconductivity and a quenching at higher temperatures. From the decay time constants of the persistent photoconductivity, the barrier height, which prevents the photoexcited electrons to be recaptured by the DX state and thus causes the persistency, was determined to 80 ± 40 meV by fitting the multi phonon emission model to the data. Finally, noise experiments at room temperature and above showed a clear generation–recombination ($g - r$) noise spectrum. The thermal activation of the characteristic time constant yielded an activation energy of 390 meV which agrees well with the sum of activation energy of the dark conductivity (320 meV) and the barrier height (80 meV). In contrast to the $g - r$ behaviour observed at ambient temperature, a $1/f$ noise spectrum was found at low temperatures in the persistent photoconductivity state. This is in full agreement with a shallow donor which persists at low temperatures after photoexcitation.

Although first work concerning Si in AlGaN has been done and revealed evidence of a DX relaxation of the Si donor, open questions remain. Since the wurtzite lattice provides two inequivalent relaxed sites for the Si DX state, it is interesting which site is favoured. A high resolution X-ray diffraction experiment could help in solving this question. Furthermore the role of the huge electric field induced by polarization of the nitrides on the DX behaviour is not understood. Measurements under uniaxial pressure could give hints about the dependence on the internal electric field.

Concerning defect spectroscopy in diamond, highly sophisticated methods have to be applied to definitely identify the microscopic nature of the implantation defect. A suitable technique would be a combination of capacitance spectroscopy and spin resonance tech-

niques to obtain a microscopic signature of the defect. Another possibility would be trying to correlate a luminescence feature with the ODLTS absorption, since radiation induced luminescence lines are widely studied in the case of diamond. This would lead to a knowledge of the energetic position in the band gap of the radiation defects in diamond, which is only very sparse until now.

APPENDIX A

Influence of a Compensated Layer on the $C-V$ Profile

We assume a diode with a space charge distribution as shown in Fig. A.1a. The bulk acceptor density N_A is reduced within the width W_0 to a much lower value N_A^p. This reduction can be caused by e. g. compensation or passivation. For simplicity, N_A^p is assumed to be constant within W_0.

The electric field can be calculated by integrating Poisson's equation. For $0 \leq x \leq W_0$ (passivated region) we obtain

$$E^p(x) = -\frac{qN_A}{\varepsilon}\left[W - x\frac{N_A^p}{N_A} - W_0\left(1 - \frac{N_A^p}{N_A}\right)\right], \tag{A.1}$$

for $W_0 \leq x \leq W$ (unpassivated region) we calculate

$$E(x) = -\frac{qN_A}{\varepsilon}(W - x), \tag{A.2}$$

where N_A is the acceptor density in the unpassivated region and N_A^p the residual acceptor density in the passivated region. q is the unit charge and ε the dielectric constant of the sample. The electric field is shown in Fig. A.1b. In the region where the space charge is low, the electric field is only weakly varying in space.

Integrating Eqs. A.1 and A.2 again, leads to the potential distribution representing the band edges shown in Fig. A.1c. The built-in potential is given by

$$V_{\mathrm{b}i} = \frac{qN_A}{2\varepsilon}\left[W^2 - W_0^2\left(1 - \frac{N_A^p}{N_A}\right)\right] \tag{A.3}$$

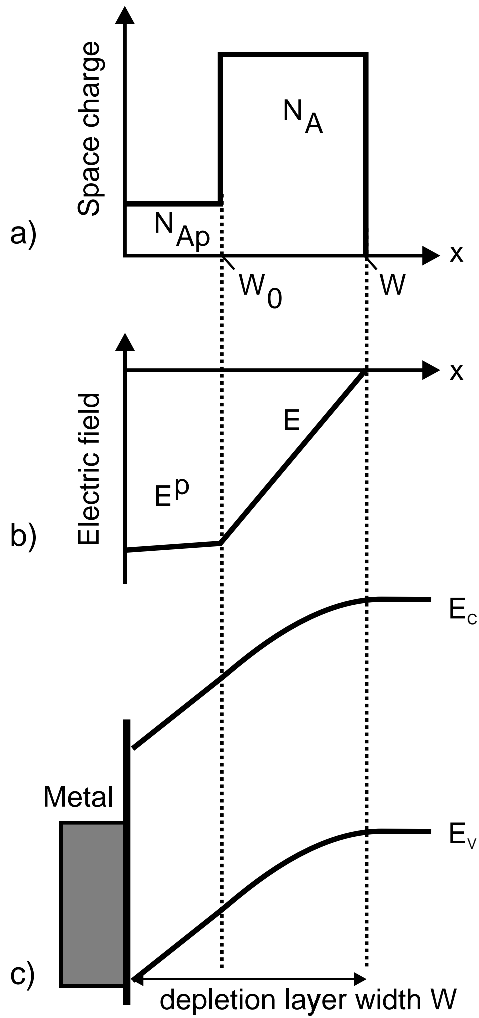

Figure A.1: Sketch of the space charge (a), the electric field (b) and the band edges (c) of a diode with an inhomogeneous space charge density.

Using the relation $C = \varepsilon A/W$, where A is the area of the diode, we find

$$C(V) = \frac{\varepsilon A}{\sqrt{\frac{2\varepsilon}{qN_A}(V_{\mathrm{b}i} + V) + W_0^2\left(1 - \frac{N_A^p}{N_A}\right)}}. \tag{A.4}$$

This relation is valid even when N_A^p is not constant as shown in Fig. A.1. Since the space charge is integrated twice and $W > W_0$ always holds, only the average value $1/W_0 \int_0^{W_0} N_A^p(x)dx$ is important.

APPENDIX B

Inhomogeneous trap distribution

We consider the case of a diode with a space charge distribution as sketched in Fig. B.1. It is a normal Schottky diode where within a depth W_0 additional traps have been introduced and the compensation ratio of the shallow acceptor is higher, resulting in a lower acceptor density N_A^p than the one in the bulk (N_A). The depletion layer W extends deeper into the bulk of the semiconductor than the implanted layer, i. e. $W > W_0$. The formula for the capacitance of a Schottky diode with a step function acceptor density (dashed line in Fig. B.1) has been derived in Appendix A. The actual shape of the space charge profile is not relevant for the calculation of the capacitance as long as $W > W_0$, since only the integral over the space charge is important. We only have to add the trap density N_T^+ of the charged

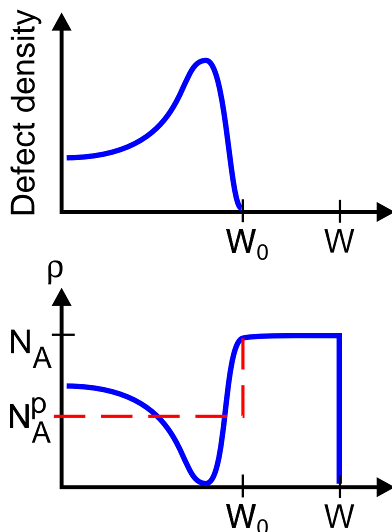

Figure B.1: Sketch of the spatial distribution of the traps induced by ion implantation and the resulting charge density ρ within the depletion layer. The dashed line is the distribution as assumed for the calculation of the $C-V$ curves.

implantation defects to the acceptor density in the implanted layer N_A^p. This results in

$$C(V) = \frac{\varepsilon A}{\sqrt{\frac{2\varepsilon}{qN_A}(V_{\mathrm{b}i}+V)+W_0^2\left(1-\frac{N_A^p-N_T^+}{N_A}\right)}}. \tag{B.1}$$

Using the abbreviation $C_b = \varepsilon A/W_b$, where $W_b = \sqrt{2\varepsilon/(qN_A)(V_{\mathrm{b}i}+V)}$ we get

$$C(V) = \frac{C_b}{\sqrt{1+\frac{W_0^2}{W_b^2}\left(1-\frac{N_A^p-N_T^+}{N_A}\right)}}. \tag{B.2}$$

Expanding the square root leads to

$$C(V) \approx C_b\left(1-\frac{1}{2}\frac{W_0^2}{W_b^2}\left(1-\frac{N_A^p-N_T^+}{N_A}\right)\right) \tag{B.3}$$

Using $\Delta C_{SS} = C(t=\infty) - C(t=0)$ (the change in steady state capacitance) and assuming, that $N_T^+(t=\infty) = 0$ (since the trapped holes have been emitted) we get an expression for the trap density N_T

$$N_T = 2N_A \frac{\Delta C_{SS}}{C_b}\frac{W_b^2}{W_0^2}. \tag{B.4}$$

W_b and C_b are determined from the unimplanted diodes. This formula is the one known for a homogenous distribution[Lan74] with an additional weighting factor W_b^2/W_0^2.

Assuming that the time dependence of the occupied trap density can be described by an exponential function $N_T^+ = N_T(1-\exp(-\nu t))$, where ν is the emission rate, we can write the first time derivative for short times of the capacitance (B.3) as

$$\left.\frac{dC}{dt}\right|_{t<1/\nu} = \frac{C_b}{2N_A}\frac{W_0^2}{W_b^2}N_T\sigma_o\Phi. \tag{B.5}$$

Here the relation $\nu = \sigma_0\Phi$ was used, where σ_o and Φ are the photoionisation cross section of the defect and the photon flux, respectively. Using the expression (B.4) for the trap density we can write for the photoionisation cross section

$$\sigma_o = \frac{dC/dt}{\Phi\Delta C_{SS}}. \tag{B.6}$$

which is the same as for a homogenously distributed trap density. This is quite plausible, since in the fraction $\frac{dC}{dt}/\Delta C_{SS}$ all effects of inhomogeneity are canceled.

Bibliography

[All98] L. Allers, A. T. Collins and J. Hiscock, Diamond. Rel. Materials **7**, 228 (1998)

[Amb96] O. Ambacher, R. Dimitrov, D. Lentz, T. Metzger, W. Rieger and M. Stutzmann, J. Cryst. Growth **167**, 1 (1996)

[Amb99] O. Ambacher, J. Smart, J. R. Shealy, N. G. Weimann, K. Chu, M. Murphy, W. J. Schaff, L. F. Eastman, R. Dimitrov, L. Wittmer, M. Stutzmann, W. Rieger and J. Hilsenbeck, Appl. Phys. Lett. **85**, 3222 (1999)

[And93] A. B. Anderson, S. P. Mehandru, Phys. Rev B **48**, 4423 (1993)

[Ang98] H. Angerer *Herstellung von Gruppe III-Nitriden mittels Molekularstrahlepitaxie*, in *Selected Topics of Semiconductor Physics and Technology* edited by G. Abstreiter, M.-C. Amann, M. Stutzmann and P. Vogl, (Walter Schottky Institut, TU München, Germany 1998) Vol. 15

[Ash86] N. W. Ashcroft, M. Mermin, *Solid State Physics*, Saunders, Philadelphia 1976

[Bay00a] M. W. Bayerl, *Magnetic Resonance Investigations of Group III-Nitrides*, in *Selected Topics of Semiconductor Physics and Technology* edited by G. Abstreiter, M.-C. Amann, M. Stutzmann and P. Vogl, (Walter Schottky Institut, TU München, Germany 2000) Vol. 32

[Bay00b] M. W. Bayerl, M. S. Brandt, O. Ambacher, J. A. Majewski, M. Stutzmann and D. J. As, submitted to Phys. Rev. B

[Ben98] L. X. Benedict, E. L. Shirley and R. B. Bohn, Phys. Rev. B, **57**, R9385 (1998)

[Ber00] P. Bergonzo, F. Foulon, A. Brambilla, D. Tromson, C. Jany and S. Hann, Diamond Rel. Materials **9**, 1003 and 960 (2000)

[Bog97] P. Boguslawski and J. Bernholc, Phys. Rev. B **56**, 9496 (1997).

[Bra95] O. Brandt, H. Yang, B. Jenichen, Y. Suzuki, C. Däweritz and K. Ploog, J. Appl. Phys. **52**, R2253 (1995)

[Bra98] M. S. Brandt, P. Herbst, H. Angerer, O. Ambacher and M. Stutzmann, Phys. Rev. B **58** 7786 (1998)

[Bro55] J. J. Brophy, Phys. Rev. **99**, 1336 (1955)

[Bun55] F. B. Bundy, H. T. Hall, H. M. Strong and R. H. Wentorf, Nature **176**, 51 (1955)

[Bun67] F. P. Bundy and J. S. Kasper, J. Chem. Phys. **46**, 3437 (1967)

[Böe90] K. W. Böer, *Survey of Semiconductor Physics*, van Nostrad Reinhold, New York, 1990

[Car93] W. E. Carlos, J. A. Freitas, M. Asif Khan, D. T. Olson, and J. N. Kuznia, Phys. Rev. B **48**, 17878 (1993).

[Car97] W. E. Carlos, 7th Int. Conf. Shallow-Level Centers in Semiconductors, ed. C. A. J. Ammerlaan, and B. Pajot, World Scientific, Singapore, 1997, p. 13

[Cha76] D. J. Chadi, A. H. Clark, and R. D. Burnham, Phys. Rev. B **13**, 4466 (1976).

[Cha81] A. Chantre, G. Vincent, D. Bois, Phys. Rev. B **23**, 5335 (1981)

[Cha88] D. J. Chadi and K. J. Chang, Phys. Rev. Lett. **61**, 873 (1988).

[Che98] J. Chevallier, B. Theys, A. Lusson, C. Grattepain, A. Deneuville, E. Gheeraert, Phys. Rev. B **58**, 7966 (1998)

[Che00] J. Chevallier, D. Ballutaud, B. Theys, F. Jomard, A. Deneuville, E. Gheeraert and F. Pruvost, Diamond Rel. Materials **9**, 1171 (2000)

[Chu92] B.-C. Chung and M. Gershenzon, J. Appl. Phys. **72**, 651 (1992)

[Cla64] C. D. Clark, P. J. Dean and P. V. Harris, Proc. R. Soc. London A **277**, 312 (1964)

[Cla73] C. D. Clark, J. Walker, Proc. R. Soc. London A **234**, 241 (1973)

[Cla79] C. D. Clark, B. J. Parsons and L. A. Vermeulen, J. Phys. C : Solid State Phys. **12** 2597 (1979)

[Clu98] M. D. McCluskey, N. M. Johnson, C. G. van de Walle, D. P. Bour, M. Kneissl and W. Walukiewicz, Phys. Rev. Lett. **80**, 4008 (1998).

[Coh89] M. J. Cohen and J. R. Chelikowsky, *Electronic structure and optical properties of semiconductors*, 2nd ed. Springer, Berlin 1989

[Col69] A.T. Collins, E.C. Lightowlers and P.J. Dean, Phys. Rev., **183**, 725 (1969)

[Col71] A. T. Collins and A. W. S. Williams, J. Phys. C: 6Solid State Phys. **4**, 1789 (1971)

[Col92] A. T. Collins, Diamond Rel. Mat. **1** 457 (1992)

[Cra68] M. G. Craford, G. E. Stillman, J. A. Rossi and N. Holonyak, Jr., Phys. Rev. **168**, 867 (1968)

[Dan96] S. Dannefaer, W. Zhu, T. Bretagnon and D. Kerr, Phys. Rev. B **53**, 1979 (1996)

[Dav76] G. Davies, J. Phys. C: Solid State Phys. **6**, L537 (1976)

[Dav77] G. Davies, Nature **269**, 498 (1977)

[Dav92] G. Davies, S. C. Lawson, A. T. Collins, A. Mainwood and S. J. Sharp, Phys. Rev. B **46**, 13157 (1992)

[Dav94] G. Davis (ed.) *Properties and Growth of Diamond*, emis data review series, inspec, London (1994)

[Dea65] P. J. Dean, E. C. Lightowlers and D. R. Wright, Phys. Rev. **140**, A352 (1965)

[Den96] G. Denninger, R. Beerhalter, D. Reiser, K. Maier, J. Schneider, T. Detchprohm, and K. Hiramatsu, Sol. State Commun. **99**, 347 (1996)

[Der75] B. V. Deryagin and D. V. Fedosev, Sci. Am. **233** 102 (1975)

[Dim00] R. Dimitrov, *AlGaN/GaN Transistoren*, in *Selected Topics of Semiconductor Physics and Technology* edited by G. Abstreiter, M.-C. Amann, M. Stutzmann and P. Vogl, (Walter Schottky Institut, TU München, Germany 2000) Vol. 28

[Dis93] B. Dischler, C. Wild, W. Müller-Sebert and P. Koidl, Physica B **185**, 217 (1993)

[Dob91] L. Dobaczewski and P. Kaczor, Phys. Rev. Lett. **66**, 68 (1991).

[Dob94] L. Dobaczewski and P. Kaczor, J. Appl. Phys. **76**, 194 (1994)

[Eng70] R. Englman and J. Jortner, Mol. Phys. **18**, 145 (1970)

[Far69] R. G. Farrer, Solid State Comm. **7**, 685 (1969)

[Far72] R. G. Farrer and L. A. Vermeulen, J. Phys. C: Sol. State Phys. **5** 2762 (1972)

[Fie92] J.E. Field (ed.) *The properties of natural and synthetic diamond*, academic press, London 1992

[Fow31] R. H. Fowler, Phys. Rev. **38**, 45 (1931)

[Fuc95] F. Fuchs, C. Wild, K. Schwarz, W. Müller-Sebert and P. Koidl, Appl. Phys. Lett. **66**, 177 (1995)

[Gar00] J. Garridas, C. E. Nebel and M. Stutzmann, submitted to Appl. Phys. Lett.

[Gi99] R. S. Gi, K. Tashiro, S. Tanaka, T. Fujisawa, H. Kimura, T. Kuruso and M. Iida, Jpn. J. Appl. Phys. **38**, 3492 (1999)

[Glo73] G. H. Glover, Solid-State Electron. **16**, 973 (1973)

[Goe00] S. T. B. Gönnenwein, M. W. Bayerl, M. S. Brandt and M. Stutzmann, J. Non-Cryst. Solids **266 - 269**, 237 (2000)

[Gol98] Y. Golan, X. H. Wu, J. S. Speck, R. P. Vaudo and V. M. Phanse, Appl. Phys. Lett. **73**, 3090 (1998)

[Gri75] H. G. Grimmeis and L.-Å. Lebedo, J. Phys. C Solid State Phys, **8**, 2615 (1975)

[Grz93] I. Grzegory, J. Jun, S. Krukowski, M. Bockowski and S. Porowski, Physica B **185**, 99 (1993)

[Göt95] W. Götz, N.M. Johnson, R. A. Street, H. Amano, I. Akasaki, Appl. Phys. Lett. **66**, 1340 (1995)

[Göt96] W. Götz, N.M. Johnson, C. Chen, J. Walker, D.P. Bour and R. A. Street, Appl. Phys. Lett. **68**, 667 (1996)

[Hae00] K. Haenen, private communication, Hasselt 2000

[Hal82] A. J. Halperin and L. A. Vermeulen, J. Phys. Chem. Solids **43** 691 (1982)

[Har94] M. L. Hartsell, H. A. Wynarts and B. A. Fox, Appl. Phys. Lett. **65**, 430 (1994)

[Hay96] K. Hayashi, S. Yamanaka, H. Watanbe, T. Sekiguchi, H. Okushi and K. Kajimura, J. Appl. Phys., **81**, 744 (1996)

[Hen77] C. H. Henry and D. V. Lang, Phys. Rev. B **15**, 989 (1977)

[Her90] C. P. Herrero, M. Stutzmann, A. Breitschwerdt and P. V. Santos, Phys. Rev. B, **41**, 1054 (1990)

[Hil76] R. M. Hill, phys. stat. sol. (a) **34**, 601 (1976)

[Hir97] M. T. Hirsch, J. A. Wolk, W. Walukiewicz and E. E. Haller, Appl. Phys. Lett. **71**, 1098 (1997).

[Ink81] J. C. Inkson, J. Phys. C: Solid State Phys. **14**, 1093 (1981)

[Ist97] A. A. Istratov, J. Appl. Phys. **82**, 2965 (1997)

[Jac83] J. D. Jackson, *Klassische Elektrodynamik*, 2. Auflage, Walter de Gruyter, New York 1983

[Jar77] M. Jaros, Phys. Rev. B, **16**, 3694 (1977)

[Job96] R. Job, M. Werner, A. Denisko, A. Zaitsev and W. R. Fahrner, Diamond Rel. Mat.**5**, 757 (1996)

[Joh65] E. O. Johnson, RCA Rev. **26**, 163 (1965)

[Joh85] N. M. Johnson, Appl. Phys. Lett. **47**, 874 (1985)

[Kaj91] S. A. Kajihara, A. Antonelli, J. Bernholc and R. Car, Phys. Rev. Lett. **66** 2010 (1991)

[Kal97] R. Kalish, C. Uzan-Saguy, B. Philosoph, V. Richter and S. Prawer, Appl. Phys. Lett. **70**, 999 (1997)

[Kal99] R. Kalish, A. Reznik, C. Uzan-Saguy and C. Cytermann, Appl. Phys. Lett. **76**, 757 (2000)

[Kam83] M. Kamo, Y. Sato, S. Matsumoto and N. Setaka, J. Crst. Growth **62**, 642 (1983)

[Kei65] T. H. Keil, Phys. Rev., **140**, A601 (1965)

[Kif94] I. Kiflawi, A. E. Mayer, P. M. Spear, J. A. van Wyk and G. S. Woods, Phil. Mag. **69**, 1141 (1994)

[Kim97] H. Kim, R. Vogelgesang, A. K. Ramdas, S. Rodrigues, M. Grimsditch and T. R. Anthony, Phys. Rev. Lett. **79**, 1706 (1997)

[Kir88] J. R. Kirtley, T. N. Theis, P. M. Mooney and S. L. Wright, J. Appl. Phys. **63**, 1541 (1988)

[Kit93] Ch. Kittel, *Einführung in die Festkörperphysik*, Oldenburg Verlag, München 1993

[Kli95] C. F. Klingshirn, *Semiconductor optics*, Springer, Berlin 1995

[Kna97] W. Knap et al., Appl. Phys. Lett. **70**, 2123 (1997).

[Kog77] S. M. Kogan and T. M. Lifshits, phys. stat. sol. (a) **39**, 11 (1977)

[Koi97] S. Koizumi, M. Kamo, Y. Sato, H. Ozaki and T. Inuzuka, Appl. Phys. Lett. **71**, 1065 (1997)

[Koi00] S. Koizumi, T. Teraji and H. Kanda, Diamond Rel. Materials **9**, 935 (2000)

[Kon93] J. Kono, S. Takeyama, T. Takamasu, N. Miura, N. Fujimori, Y. Nishibayashi, T. Nakajima and K. Tsuji, Phys. Rev. B **48**, 10917 (1993)

[Kur00] C. Kurtsiefer, S. Mayer, P. Zarda and H. Weinfurter, Phys. Rev. Lett. **85**, 290 (2000)

[Lag74] O. Lagerstedt and B. Monemar, J. Appl. Phys. **45**, 2266 (1974)

[Lan74] D. V. Lang, J. Appl. Phys. **45**, 3023 (1974)

[Lan75] D. V. Lang and R. A. Logan, J. Electr. Materials **4**, 1053 (1975)

[Lan77] D.V. Lang and R. A. Logan, Phys. Rev. Lett. **39**, 635 (1977).

[Lan82] Landolt-Börnstein: New Series III/17a: Semiconductors: *Pysics of Group IV Elements and II-V Compounds*, Ed.: O. Madelung, Springer, Berlin 1982

[Lan92] D.V. Lang in *Deep Centers in Semiconductors*, ed. S.T. Pantelides, Gordon and Breach Science Publishers, 2nd edition, Yverdon 1992.

[Law92] S. Lawson, G. Davies, A. T. Collins and A. Mainwood, J. Phys.: Condens. Matter **4**, L125 (1992)

[Lax53] M. Lax, J. Chem. Phys., **91**, 265 (1953)

[Li97] J. Z. Li, J. Y. Lin, H. X. Jiang, M. Asif Khan and Q. Chen, J. Appl. Phys. **82**, 1227 (1997)

[Loo97] D. C. Look, D. C. Reynolds, J. W. Hemsky, J. R. Sizelove, R. L. Jones and R. J. Molnar, Phys. Rev. Lett. **79**, 2273 (1997)

[Luc65] G. Lucovsky, Sol. St. Comm., **3**, 299 (1965)

[Mac54] S. Machlup, J. Appl. Phys. **25**, 341 (1954)

[Mai97] A. Mainwood and A. M. Stoneham, J. Phys. C : Condens. Matter **9**, 2453 (1997)

[Maj97] J. A. Majewski, M. Städele, and P. Vogl, MRS Symp. Proceed. **449**, 887 (1997).

[Mal93] D. M. Malta, J. A. van Windheim and B. A. Fox, Appl. Phys Lett. **62**, 2926 (1993)

[Mar77] G. M. Martin, A. Motinneau and A. Mircea, Electronics Letters **13**, 191 (1977)

[Mas76] B. Massarani and J. C. Bourgaoin, Phys. Rev. B **14**, 3682 (1976)

[Mea76] C. A. Mead and T. C. McGill, Physics Lett. **58A**, 249 (1976)

[Meh94] S.P. Mehandru and A.B. Anderson, J. Mater. Res., **9**, 383 (1994)

[Mei00] D. Meister, M. Böhm, M. Topf, W. Kriegseis, W. Burkhardt, I. Dirnstorfer, S. Rösel, B. Farangis, B. K. Meyer, A. Hoffmann, H. Siegele, C. Thomsen, J. Christen and F. Bertram, J. Appl. Phys. **88**, 1811 (2000)

[Mil75] G. L. Miller, J. V. Ramirez and D. A. H. Robinson, J. Appl. Phys. **46**, 2638 (1975)

[Mit63] E. W. J. Mitchell *Proc. 1st Congr. Diamond in Industry*, Paris 1962, pp 241

[Moe94] W. Mönch, Europhys. Lett., **27**, 479 (1994)

[Moo92] P. M. Mooney and T. N. Theis, Comments Cond. Mat. Phys. **16**, 167 (1992)

[Mot82] N. F. Mott, Proc. R. Soc. London A **382**, 1 (1982)

[Mot87] N. F. Mott, *Conduction in non-crystalline solids*, Oxford university press, Oxford (1987)

[Nak92] S. Nakamura, N. Iwasa, M. Senoh, and T. Mukai, Jpn. J. Appl. Phys. **31**, 1258 (1992)

[Nel77] R. J. Nelson, Appl. Phys. Lett. **31**, 351 (1977)

[Nes96] M. Nesládek, M. Vaněček, L. M. Stals, phys. stat. sol. (a) **154**, 283 (1996)

[Nij97] J. te Nijenhuis, G. Z. Cao, P. C. H. J. Smits, W. J. P. van Enckevort, L. J. Giling, P. F. A. Alkemade, M. Nesládek, Z. Remeš, Diamond Rel. Mater. **6** 1726 (1997)

[Nip98] J. C. Nipko and C.-K. Loong, Phys. Rev. B **57**, 10550 (1998)

[Pan75] J. I. Pankove, S. Bloom and G. Harbeke, RCA Rev. **36**, 163 (1975)

[Par97] C. H. Park and D. J. Chadi, Phys. Rev. B **55**, 12995 (1997).

[Pea49] G. L. Pearson and J. Bardeen, Phys. Rev. **75**, 865 (1949)

[Pea92] S. J. Pearton, J. W. Corbett and M. Stavola, *Hydrogen in crystalline semiconductors*, Springer, 1992

[Pra93] S. Prawer, C. Uzan-Saguy, G. Braunstein and R. Kalish, Appl. Phys. Lett. **63**, 2502 (1993)

[Pri89] J. F. Prins, Phys. Rev. B **39**, 3764 (1989)

[Pro64] V. Prosser, Czech. J. Phys. **B15**, 128 (1964)

[Ris00] J. Ristein, presented at *Vth Workshop on defects in CVD diamond*, Hasselt 2000, Belgium

[Ris97] J. Ristein, W. Stein, L. Ley, Phys. Rev. Lett., **78**, 1803 (1997)

[Rob34] R. Robertson, J. J. Fox and A. E. Martin, Phil. Trans Roy. Soc London **A232**, 463 (1934)

[Rob86] J. Robertson, Advances in Physics, **35**, 317 (1986)

[Roh98] E. Rohrer, *Photoleitungsspektroskopie von Diamant*, in *Selected Topics of Semiconductor Physics and Technology* edited by G. Abstreiter, M.-C. Amann, M. Stutzmann and P. Vogl, (Walter Schottky Institut, TU München, Germany 1998) Vol. 10

[Roh98] E. Rohrer, C. E. Nebel, M. Stutzmann, A. Flöter, R. Zachai, X. Jiang and C.-P. Klages, Diamond Rel. Mat. **7**, 879 (1998)

[Saa00] D. Saada, J. Adler and R. Kalish, Appl. Phys. Lett. **77**, 878 (2000)

[Sac99] J.-U. Sachse, J. Weber, H. Lemke, Phys. Rev. B **61**, 1924 (2000)

[Sak99] I. Sakaguchi, M. N.-Gamo, Y. Kikuchi, E. Yasu, H. Haneda, T. Suzuki and T. Ando Phys. Rev. B **60**, R2139 (1999)

[Sch92] F. Schwabl, *Quantenmechanik*, 4. Auflage, Springer, Berlin 1993

[Sch99] M. Schreck, H. Roll, B. Stritzker, Appl. Phys. Lett. **74**, 650 (1999)

[See85] K.-H. Seeger, *Semiconductor physics*, Springer, Berlin 1985

[Sho52] W. Shockley and W. T. Read, Jr., Phys. Rev. B. **87**, 62 (1952)

[Ski99] C. Skierbiszewski, T. Suski, M. Leszczynski, M. Shin, M. Skowronski, M. D. Bremser and R. F. Davis, Appl. Phys. Lett. **74**, 3833 (1999).

[Ste00a] H. Sternschulte M. Schreck, B. Stritzker, A. Bergmaier and G. Dollinger, accepted for publication in Diamond Rel. Mat.

[Ste00b] J. W. Steeds, S. J. Charles, J. Davies and I. Griffin, Diamond Rel. Materials **9**, 397 (2000)

[Sta80] D. L. Staebler and J. I. Pankove, Appl. Phys. Lett. **37**, 609 (1980)

[Ste99] H. Sternschulte M. Schreck, B. Stritzker, A. Bergmaier and G. Dollinger, Phys. Stat. Sol. A. **174**, 65 (1999)

[Sze85] S. M. Sze, *Semiconductor Devices*, Wiley, New York 1985

[Tac92] T. Tachibana, B. E. Williams and J. T. Glass, Phys. Rev. B **45**, 11975 (1992)

[Tac00] T. Tachibana, Y. Yokoya, K. Hayashi, K. Miyata and K. Kobashi, Y. Shintani, Diamond Rel. Mat. **9**, 251 (2000)

[Tav85] A.J. Tavendale, D. Alexiev, A.A. Williams, Appl. Phys. Lett., **47**, 316 (1985)

[Ued99] A Uedono, S. Fujii, N. Morishita, H. Itoh, S. Tanigawa and S. Shikata, J. Phys.: Condensed Matter **11**, 4109 (1999)

[Ver81] L. A. Vermeulen and A. Halperin, J. Phys. Chem. Solids **42**, 115 (1981)

[Vis92] E. P. Visser, G. J. Bauhuis, G. Janssen, W. Vollenberg, W. J. P van Enckevort and L. J. Giling, J. Phys.: Condens. Matter **4**, 7365 (1992)

[Vli65] K. M. van Vliet and J. R. Fassett in *Fluctuation Phenomena in Solids*, edited by R. Burgers, Academic Press, New York, 1965

[Wal98] C. G. van de Walle, Phys. Rev. B **57**, R2033 (1998).

[Wei88] M. B. Weissman, Rev. Mod. Phys. **60**, 537 (1988)

[Wet97] C. Wetzel, T. Suski. J. W. Ager III, E. R. Weber, E. E. Haller, S. Fischer, B. K. Meyer, R. J. Molnar and P. Perlin, Phys. Rev. Lett. **78**, 3923 (1997).

[Woo86] G. S. Woods, Proc. Roy. Soc. London A **407**, 219 (1986)

[Wyn94] H. A. Wynands, D. M. Malta, B. A. Fox, J. A. van Windheim, J. P. Fleurial D. Irvine and J. Vandersande, Phys. Rev. B **49**, 5745 (1994)

[Yam00] S. Yamanaka, D. Takeuchi, H. Watanabe, H. Okushi, K. Kajimura, Diamond Rel. Materials **9**, 956 (2000)

[Yi96] G.-C. Yi and B. W. Wessels, Appl. Phys. Lett. **68**, 3769 (1996)

[Yu96] P. Y. Yu, M. Cardona, *Fundamentals of Semiconductors*, Springer, Berlin 1996

[Zei98] R. Zeisel, C.E. Nebel and M. Stutzmann, J. Appl. Phys., **84**, 6105 (1998)

[Zho96] X. Zhou, G. D. Watkins, K. M. McNamara Rutledge, R. P. Messmer and Sanjay Chawla, Phys. Rev. B **54**, 7881 (1996)

[Zie85] J. F. Ziegler, J. P. Biersack and U. Littmark, *The Stopping and Range of Ions in Solids* (Pergamon, New York, 1985)

[Zie86] A. van der Ziel, *Noise in solid state devices and circuits*, Wiley, New York, 1986

[Zun89] T. Zundel and J. Weber, Phys. Rev. B, **39**, 13549 (1989)

Acknowledgements

At this point I want to express my thanks to all the people who helped me to make my way during the time of my Ph.D. studentship. These are in particular

Prof. Dr. Martin Stutzmann, who gave me the opportunity to study in his group. With his feeling for "hot topics" in semiconductor physics and his physical intuition and knowledge he always gave me inspiring ideas how to go on and what to do.

Dr. habil. Christoph E. Nebel, who always had "open house" for every kind of discussions and gave me enough freedom to perform my own ideas. The equipment of the "Transport-labor" enabled me to quickly built up the required experiments. The financial support from his projects gave me the opportunity to present my results on international conferences.

Dr. habil. Martin S. Brandt, who provides a good source for all kinds of information from physics to policy. Especially I want to thank him for his personal engagement in the last months of my thesis.

All my **fellow Ph.D. students**, but especially **Sebastian Gönnenwein, Günther 'Zwida' Vogg, Christopher Eisele** and **Dr. Martin Bayerl**. It was a great pleasure to have such nice colleagues. We had a lot of fun that helped us to survive all professional ups and downs.

The people who helped and supplied me with measurements:

- The noise measurements were done by **Sebastian Gönnenwein** and **Silvia Baldovino**.
- **Dr. Martin Bayerl, Sebastian Gönnenwein** and **Tobias Graf** reigned over the EPR spectrometers.

The people who supplied me with samples:

- **Dr. Roman Dimitrov** and **Uwe Karrer** under the supervision of **Dr. habil. Oliver Ambacher**. Their feeling for the MBE machine ensured that the AlGaN layers did what I want them to do.
- **Dr. Hadwig Sternschulte** from the University of Augsburg. She provided me with

the Li and S doped CVD layers. She also did the carbon ion implantation in the IIb samples.

- **Dr. Etienne Gheerheart**, who deposited the boron doped CVD sample
- **Dr. Peter Gluche** and **Oliver Kohn** from the University of Ulm, who deposited boron doped CVD layers.

The secretaries **Veronika Enter** and **Karin Rottler**, who always guided me through the jungle of bureaucracy.

The technicians **Michael Fischer, Wolfgang Bendak, Ralph Wasserrab** and **Bernhard Kratzer**, for their ”mechanical”solutions of problems in the lab.

My parents, who supported and encouraged me to follow my heart.

My wife **Irene** and my sons **Lukas** and **Jakob**. They form all that belongs to a good family where I could get all the recreation and support I needed.

Roland Zeisel, December 2000